

Cavity ringdown spectroscopy of atmospherically important radicals

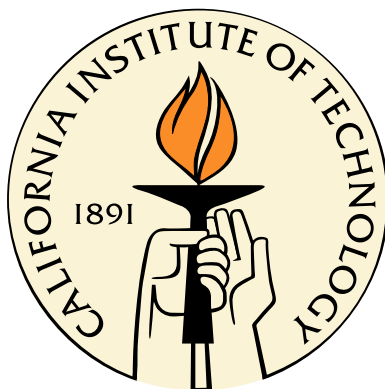
Thesis by

Andrei Deev

In Partial Fulfillment of the Requirements

for the Degree of

Doctor of Philosophy



California Institute of Technology

Pasadena, California

2005

(Defended December 14, 2004)

© 2005

Andrei Deev

All Rights Reserved

Abstract

Many radicals, due to their electronic structure, have low-lying electronic states transitions to which lie in the near-IR. They often carry more information about the molecules than the transitions in the UV. However, these transitions even in the most important atmospheric radicals have not been thoroughly investigated due to their weakness and low attainable concentrations of radicals. This thesis describes the application of cavity ringdown spectroscopy to detection of near-IR states of some atmospherically important radicals.

The near-IR cavity ringdown spectrometer constructed for these experiments is described in detail and characterized. The pulsed near-IR laser radiation was generated by sequential Raman shifting of the output of a tunable dye laser in hydrogen. The constructed multi-pass Raman cell extended the tunable range of the available dye laser continuously from the visible to 6000 cm^{-1} with 0.15 cm^{-1} resolution. The sensitivity of the instrument is $\approx 0.5\%$ of the mirror loss.

The near-IR $\tilde{A} \leftarrow \tilde{X}$ transition in peroxy radicals offers detection specificity for at least small radicals. The sensitivity of this transition to hydrogen atom substitution has been explored. The spectra of chloro-ethyl, -propyl, -butyl and -butenyl peroxy radicals in the $7000\text{-}8600\text{ cm}^{-1}$ region are reported. The origin bands of the electronic

transition were found to be shifted by 200 cm^{-1} to the red. The spectra have more complex structure than those of unsubstituted homologues. DFT calculations predicted multiple conformers for $\text{C}_2\text{H}_4\text{ClO}_2$ and $\text{C}_3\text{H}_6\text{ClO}_2$ with the energies within 2 kcal/mol. Tentative assignment of the $\text{C}_2\text{H}_4\text{ClO}_2$ spectrum is presented. The integrated cross-section for the transition in chloro-ethyl peroxy radical is estimated from the known rate of self-reaction.

The first full absorption spectrum of the "dark" $\tilde{\text{A}}\ ^2E'' \leftarrow \tilde{\text{X}}\ ^2A'_2$ transition of the nitrate radical NO_3 in the $6000\text{-}10700\text{ cm}^{-1}$ region is reported. ν_2 , ν_3 , and ν_4 progressions and several combination bands are assigned. A more accurate estimate for the position of the "dark" origin is given. Analysis of the partially resolved rotational contours suggests that NO_3 undergoes static Jahn-Teller distortion in some of the vibronic states.

Acknowledgements

I would like to acknowledge my collaborators and thank all of the people who helped me during these six years I spent at Caltech.

I am infinitely grateful to my advisor, Mitchio Okumura, for his support and guidance, for the possibility to argue with him, for the freedom he gave me, and for helping me to become an independent researcher.

I acquired most of my experimental skills from Alex Wong and Julio Lobo. They taught me molecular beam, laser and machining techniques, and many other things. I benefited from the expertise of Brian Bean and Andrew Mollner while I was constructing my cavity ringdown apparatus. David Powers assisted me in my work on peroxy radicals. The spectroscopic study of nitrate radical was carried out largely in collaboration with Jonas Sommar. He synthesized ClONO_2 and N_2O_5 , performed kinetics modeling and assisted with data acquisition. Kana Takematsu also helped with acquisition of the NO_3 spectra. Brian Drouin helped me model NO_3 spectra using SPCAT. John Stanton helped us with analysis of NO_3 data.

My experimental work would have been impossible without the help of Mike, Ray and Guy from the chemistry machine shop, and Rick from the glassware shop.

I thank Eva Garland, Lance Christensen, David Robichaud, Julie Fry, Sergey

Nizkorodov, Claire Morell, Aaron Noel, Lin Feng, Stan Sander for helpful discussions.

I thank members of the Blake and Wennberg groups for letting me borrow their tools and equipment.

I thank Mitchio and the last two generations of the Okumura group for the cordial atmosphere I enjoyed all these years.

I thank my parents, Victor and Irina Deev, for always encouraging me to learn and try new things.

Contents

Abstract	iii
Acknowledgements	v
Introduction	1
References	6
1 Near-infrared cavity ringdown spectrometer	7
1.1 Principles of cavity ringdown spectroscopy	7
1.2 Experimental apparatus	13
1.2.1 Near-infrared laser source	13
1.2.2 Flow reactor	20
1.2.3 Instrument control and data acquisition	23
1.3 Instrument characteristics	28
1.4 Summary	30
References	31
2 Near infrared spectroscopy of chloro-peroxy radicals	53

2.1	Introduction	53
2.2	Background	56
2.3	Experiment	58
2.4	Results and Discussion	60
2.5	Conclusion	68
	References	70
3	Cavity Ringdown Spectroscopy of the $\widetilde{A} \ ^2E'' \leftarrow \widetilde{X} \ ^2A'_2$ electronic transition of NO_3	97
3.1	Introduction	97
3.2	Experiment	101
3.3	Results and Discussion	103
3.3.1	Experimental Results	103
3.3.2	Assignment	105
3.3.3	Theoretical framework	109
3.3.4	Rotational contour analysis	113
3.4	Summary	117
	References	120

List of Figures

1.1	The principle of pulsed cavity ringdown spectroscopy. The pulse (its coherence length) is shorter than the cavity.	33
1.2	Optical layout of NIR-CRDS apparatus in photolysis experiments. . . .	34
1.3	Optical layout of NIR-CRDS apparatus with a long-path cell. A diode laser is used to measure the absolute concentration of NO ₃ through direct absorption at 661.5 nm.	35
1.4	Schematic diagram of components of Cavity ringdown spectrometer. . .	36
1.5	Typical ringdown trace, average of 20 shots.	37
1.6	Drawing of the Raman cell - side view.	38
1.7	Drawing of the Raman cell mirrors. All dimensions are in inches. . . .	39
1.8	Optical path of laser beam in a Herriott cell.	40
1.9	Drawing of the pick-off mirror mount - front view, 17-pass configuration. All dimensions are in inches.	41
1.10	Drawing of the back Raman cell mirror mount - interior view of the 6" ASA flange. All dimensions are in inches.	42
1.11	Assembly drawing of the flow reactor with the photolysis cell.	43

1.12	Drawings of the cells used in experiments described in chapters 2 and 3. All dimensions are in inches.	44
1.13	Assembly drawing of the cavity mirror mount.	45
1.14	Drawing of the back flange of the cavity mirror mount - exterior view.	46
1.15	Drawing of the back flange of the cavity mirror mount - cross-sectional view A-A.	47
1.16	Drawing of the back flange of the cavity mirror mount - interior view. .	48
1.17	Drawing of the front flange of the cavity mirror mount - interior view.	49
1.18	Drawing of the front flange of the cavity mirror mount - cross-sectional view B-B.	50
1.19	(a) Cavity ringdown spectrum of CO ₂ at 10 Torr. (*) denotes water lines. (b) Simulated spectrum of CO ₂ at 0.15 cm ⁻¹ resolution. Data taken from HITRAN database.	51
1.20	(a) Cavity ringdown spectrum of air at atmospheric pressure and hu- midity. (b) Simulated spectrum of 20 Torr of H ₂ O in 1 atm of air at 0.15 cm ⁻¹ resolution. Data taken from HITRAN database.	52
2.1	Cavity ringdown spectrum of C ₂ H ₅ O ₂	73
2.2	Cavity ringdown and simulated stick spectra of C ₂ H ₄ ClO ₂ . The geome- tries of the \tilde{X} and \tilde{A} states were optimized at the B3LYP/6-311++(2df,2p) level. The Franck-Condon were computed with FCFGAUS program. . .	74
2.3	Cavity ringdown spectrum of C ₃ H ₆ ClO ₂	75
2.4	Cavity ringdown spectrum of C ₄ H ₈ ClO ₂	76

2.5	Cavity ringdown spectrum of $C_4H_6ClO_2$	77
2.6	Geometries of the gauche conformers of $C_2H_4ClO_2$ optimized at the B3LYP/6-311++(2df,2p) level.	78
2.7	Geometries of the trans-trans and trans-gauche conformers of $C_2H_4ClO_2$ optimized at the B3LYP/6-311++(2df,2p) level.	79
2.8	Geometries of the transition states between the trans and the gauche conformers of $C_2H_4ClO_2$ optimized at the B3LYP/6-311++(2df,2p) level.	80
2.9	Geometries of $C_3H_6ClO_2$ optimized at the B3LYP/6-311++(2df,2p) level, Ia and Ib conformers.	81
2.10	Geometries of $C_3H_6ClO_2$ optimized at the B3LYP/6-311++(2df,2p) level, IIa, IIb and IIc conformers.	82
2.11	Geometries of $C_3H_6ClO_2$ optimized at the B3LYP/6-311++(2df,2p) level, IIIa, IIIb and IIIc conformers.	83
2.12	Kinetics of $C_2H_4ClO_2$ self-reaction.	96
3.1	Potential energy surface of a doubly-degenerate electronic state along a Jahn-Teller active doubly-degenerate mode: (a) zero Jahn-Teller and zero spin-orbit coupling; (b) linear only Jahn-Teller coupling; (c) linear and quadratic Jahn-Teller coupling; (d) linear Jahn-Teller and spin-orbit coupling.	124
3.2	Normal modes of NO_3	125
3.3	Cavity ringdown spectrum of the $\tilde{A} \leftarrow \tilde{X}$ transition of NO_3 in the 7050-7280 cm^{-1} region.	126

3.4	Cavity ringdown spectrum of the $\tilde{A} \leftarrow \tilde{X}$ transition of NO_3 in the 7500-7850 cm^{-1} region.	127
3.5	Cavity ringdown spectrum of the $\tilde{A} \leftarrow \tilde{X}$ transition of NO_3 in the 7850-8150 cm^{-1} region.	128
3.6	Cavity ringdown spectrum of the $\tilde{A} \leftarrow \tilde{X}$ transition of NO_3 in the 8100-8350 cm^{-1} region.	129
3.7	Cavity ringdown spectrum of the $\tilde{A} \leftarrow \tilde{X}$ transition of NO_3 in the 8300-8700 cm^{-1} region.	130
3.8	Cavity ringdown spectrum of the $\tilde{A} \leftarrow \tilde{X}$ transition of NO_3 in the 8600-8950 cm^{-1} region.	131
3.9	Cavity ringdown spectrum of the $\tilde{A} \leftarrow \tilde{X}$ transition of NO_3 in the 8900-9230 cm^{-1} region.	132
3.10	Cavity ringdown spectrum of the $\tilde{A} \leftarrow \tilde{X}$ transition of NO_3 in the 9210-9550 cm^{-1} region.	133
3.11	Cavity ringdown spectrum of the $\tilde{A} \leftarrow \tilde{X}$ transition of NO_3 in the 9550-9800 cm^{-1} region.	134
3.12	Cavity ringdown spectrum of the $\tilde{A} \leftarrow \tilde{X}$ transition of NO_3 in the 9720-9920 cm^{-1} region.	135
3.13	Cavity ringdown spectrum of the $\tilde{A} \leftarrow \tilde{X}$ transition of NO_3 in the 9870-10300 cm^{-1} region.	136
3.14	Cavity ringdown spectrum of the $\tilde{A} \leftarrow \tilde{X}$ transition of NO_3 in the 10300-10700 cm^{-1} region.	137

3.15	Simulation of rotational contours of a parallel and perpendicular $\tilde{A} \leftarrow \tilde{X}$ vibronic bands of NO_3	138
3.16	Simulation of rotational contours of the ν_4 and $2\nu_4$ bands.	139
3.17	Simulation of rotational contour of the $-\nu_4$ band.	140
3.18	Simulation of rotational contour of the ν_2 bands. The arrow points at the feature that can only be reproduced by the asymmetric top Hamiltonian.	141
3.19	Simulation of rotational contour of the 8290 cm^{-1} band.	142

List of Tables

2.1	Relative energies of chloro-ethyl peroxy radical conformers and transition states between them calculated with 6-311++G(2df,2p) basis set. Zero point energies were calculated at B3LYP level.	84
2.2	Frequencies of the gauche conformers of $C_2H_4ClO_2$ at the B3LYP/6-311++G(2df,2p) level.	85
2.3	Frequencies of the trans- conformers of $C_2H_4ClO_2$ in the \tilde{X} and \tilde{A} states at the B3LYP/6-311++G(2df,2p) level	87
2.4	Relative energies of chloro-propyl peroxy radical conformers at the B3LYP level with cc-pvtz and 6-311++G(2df,2p) basis sets with and without zero-point energy (ZPE) corrections.	89
2.5	Frequencies of Ia and Ib conformers of $C_3H_6ClO_2$ at the B3LYP/6-311++(2df,2p) level.	90
2.6	Frequencies of IIa, IIb and IIc conformers of $C_3H_6ClO_2$ at the B3LYP/6-311++(2df,2p) level.	92
2.7	Frequencies of IIIa, IIIb and IIIc conformers of $C_3H_6ClO_2$ at the B3LYP/6-311++(2df,2p) level.	94
3.1	Band positions and intensities of the $\tilde{A} \leftarrow \tilde{X}$ transition of NO_3	119

Introduction

Chemical and physical processes in the atmosphere include hundreds of reactions, many of which involve trace gases or radicals [1]. Nitrogen oxides (NO_x) and volatile organic compounds lead to the formation of photochemical smog in the troposphere. Oxidation of sulfur (SO_2) and nitrogen (NO_2) dioxides yields acids and causes acid rain and fog. Chlorofluorocarbons (CFCs) deliver chlorine atoms to the stratosphere where they catalyze the destruction of ozone. Carbon dioxide CO_2 , methane CH_4 , and nitrous oxide N_2O cause the greenhouse effect, and the increase of their concentrations affects the global climate. Chlorine atoms, hydroxyl OH and nitrate NO_3 radicals although present in very low concentrations are the main initiators of hydrocarbon oxidation. Many atmospheric reactions proceed through the formation of intermediate radicals (e.g. peroxy radicals), the reactivity of which determines the pathways of chemical processes.

For almost a century, optical spectroscopy has been a major tool for monitoring concentrations of trace gases both in laboratory studies and in the field. Although less sensitive than mass-spectroscopy methods, optical detection is non-intrusive and easy to implement and calibrate. In addition, optical spectroscopy is often capable

of distinguishing different structural conformers of molecules. In laboratory studies, its lower sensitivity can be compensated by higher than atmospheric concentrations of studied species.

Atmospheric radicals can also be produced at concentrations much higher than the ones present in the atmosphere; however, the attainable concentrations are limited by the radicals' reaction rates with themselves and their precursors. Therefore, studies of radicals even under laboratory conditions require very sensitive spectroscopic techniques. Laser-induced fluorescence (LIF) and resonance-enhanced multiphoton ionization (REMPI) are often the methods of choice in studies of electronic states radicals and photodissociation spectroscopy, followed by detection of products in studies of vibrational states. These methods offer high sensitivity; however, these techniques can be applied only to a limited number of small molecules. Photodissociation spectroscopy is limited to molecules yielding detectable products. LIF and REMPI fail for large molecules due to internal conversion or dissociation. Direct absorption spectroscopy is a universal approach applicable to both electronic and vibrational transitions that avoid the aforementioned limitations. In a classic direct absorption experiment, a change in the intensity of radiation is measured after it passes through the sample. The minimum detectable fractional absorption in such an experiment is limited by fluctuation of the light intensity and typically lies in the $10^{-4} - 10^{-5}$ range. However, such sensitivities are sufficient only for studies of extremely strong transitions in radicals.

Several experimental techniques have been developed in the past couple of decades

that allowed one to avoid the source noise. Frequency-modulation diode laser spectroscopy, developed in the early 1980's, achieves it by shifting detection to high frequencies and can theoretically increase the sensitivity to the shot noise limit [2]. The method became widely adopted by spectroscopists and atmospheric chemists for studies of transient species. Diode lasers are convenient sources of radiation in the near-infrared and in the visible part of the spectrum because they are relatively inexpensive and have narrow linewidth. However, limited tunability of diode lasers (10 cm^{-1} for distributed feedback lasers and 100 cm^{-1} for external cavity lasers) limits their application to spectroscopy of already known transitions.

Cavity ringdown spectroscopy (CRDS) is another direct absorption spectroscopy method introduced in the late 1980's [3] that can be used with both pulsed and continuous wave (CW) laser sources [4]. The method is based on measuring the life time of radiation trapped in a high-finesse optical cavity. Since the decay time does not depend on the power of the radiation of the cavity, the intensity fluctuations of the laser source noise does not affect the measured absorption. Typically, cavity ringdown spectroscopy can detect fractional absorption on the order of $10^{-6} - 10^{-8}$ per pass. This thesis will describe a flow cell near-infrared cavity ringdown spectrometer, constructed in the course of thesis work and the results of our spectroscopic studies of low-lying electronic states of several atmospherically important radicals.

The near-infrared part of the spectrum is a convenient region for detection of many atmospheric species in direct absorption. Although the near-IR transitions have smaller cross-sections than the transitions in the visible or mid-IR, detection in

the near-IR offers some advantages over other spectral regions. Detection of specific molecules via strong electronic transitions in the UV, although possible under laboratory conditions, is difficult because many species have broad absorption bands in this region. The fundamental bands of molecular vibrations in the mid-infrared also have larger cross-sections than their overtones. However, the higher power of available laser sources in the near-IR and the higher sensitivity of detectors can partially compensate for lower absorption. The low cost of near-IR diode lasers and photodetectors and the fact that they do not require cooling also facilitate the development of instruments for this region.

The development of high-sensitivity instruments in the near-infrared also made possible the spectroscopy of low-lying electronic states of radicals. The typically small cross-section of near-IR electronic transitions, together with low attainable concentrations of radicals, makes these transitions accessible only by high-sensitivity spectroscopic methods. For this reason, until now, the near-infrared electronic states of some very common radicals had not been explored. Although the low-frequency transitions have lower oscillator strength, they often are narrower and more structured than the transitions in the UV and can reveal more about the geometrical and electronic structure of the radical, as well as offer detection specificity.

The main goal of this work was to build a widely tunable near-infrared cavity ringdown spectrometer and use it to identify and study low-lying electronic states of atmospheric radicals. Chapter 1 of this thesis describes the design of the instrument. It contains technical characteristics of the multi-pass Raman cell used as an near-IR

source and the ringdown flow cell constructed for these experiments, as well as a description of the experimental procedures.

Chapter 2 presents results of our experimental and theoretical study of peroxy radicals formed in Cl atom-initiated oxidation of several simple alkenes and dienes. It reports the first spectra of the electronic $\tilde{A} \leftarrow \tilde{X}$ transitions in the radicals. *Ab initio* calculations were also performed in order to determine the structure of the smallest radicals and assign the vibronic bands.

Chapter 3 is dedicated to another important atmospheric species: nitrate radical NO_3 . In spite of the fact that nitrate radical has been studied for almost a century, it appears that little is known about its lowest electronic state. Because the $\tilde{A} \leftarrow \tilde{X}$ transition is electronically forbidden, its detection requires high-sensitivity spectroscopic techniques. Prior to this work, spectrum of only one vibronic band of the \tilde{A} state had been reported [5]. This thesis will present the first full spectrum of the $\tilde{A} \leftarrow \tilde{X}$ electronic transition in the 6000-10700 cm^{-1} region containing more than 30 new bands, as well as analysis of their rotational structure and vibronic progressions. The manifestation of Jahn-Teller effect in the spectrum and its influence on the molecular structure will be discussed.

References

- [1] J. H. Seinfeld and S. N. Pandis. *Atmospheric chemistry and physics: From air pollution to climate change*. John Wiley and Sons, Inc., 1998.
- [2] G. E. Hall and S. W. North. *Annual Review of Physical Chemistry*, 51:243–274, 2000.
- [3] A. O’Keefe and D. A. G. Deacon. *Review of Scientific Instruments*, 59(12):2544–2551, 1988.
- [4] J. J. Scherer, J. B. Paul, A. Okeefe, and R. J. Saykally. *Chemical Reviews*, 97(1):25–51, 1997.
- [5] E. Hirota, T. Ishiwata, K. Kawaguchi, M. Fujitake, N. Ohashi, and I. Tanaka. *Journal of Chemical Physics*, 107(8):2829–2838, 1997.

Chapter 1

Near-infrared cavity ringdown spectrometer

1.1 Principles of cavity ringdown spectroscopy

Cavity ringdown spectroscopy (CRDS) is a relatively new, very sensitive, direct absorption spectroscopy technique introduced by O’Keefe and Deacon in 1988 [1]. It is based on measurement of the decay rate of the energy of radiation trapped inside a high-finesse optical cavity and can be used with both pulsed and continuous laser sources. The main advantages of this method are its immunity to power fluctuations of the light source and long effective pathlength. The reported implementations of the method detect fractional absorption on the order of 10^{-6} - 10^{-8} . Cavity ringdown spectroscopy has found numerous application in various areas of physical chemistry. It has been used in spectroscopic studies of metal [2] and water [3] clusters, and carbon chains [4] in molecular jets. The technique has been also applied for detection of trace gasses in the atmosphere [5] and radicals in flames [6], and characterization of molecules adsorbed on surfaces [7]. More than ten years ago, cavity ringdown spectroscopy was first employed for kinetics studies of radicals [8] and since then, this

application of the technique has been becoming increasingly popular.

The basic principle of cavity ringdown spectroscopy can best be explained by the case of a pulsed source of radiation. A laser pulse is injected into a cavity formed by a pair of highly reflective mirrors. The light that passes the front mirror becomes trapped in the cavity, moving back and forth between the mirrors. After each reflection, a small portion of the light $(1 - R)I$ leaks out of the cavity. The energy of the radiation in the cavity will decay with time, and so will the intensity of the exiting light. The solution of the simple differential equation describing the intensity of the trapped light $dI/dt = -(1 - R)Ic/L$ is the exponential decay function:

$$I(t) = I_0 e^{-t/\tau_0} \quad (1.1)$$

where τ_0 is the so-called "ringdown time" of the cavity, the time after which the intensity drops by a factor of e . The ringdown time is determined by the mirror reflectivity, R , and the distance between the mirrors, L

$$\tau_0 = \frac{L}{c} \left(\frac{1}{1 - R} \right) \quad (1.2)$$

When absorbing species are present in the cavity, the additional loss of αL_s per pass will lead to a faster decay of the signal, and therefore, a shorter ringdown time. In the case when the absorption features are much broader than the laser linewidth Γ_{laser} , the absorption, $\alpha(\lambda)$, does not change over the laser line contour and the signal decay will also be exponential with the ringdown time

$$\tau = \frac{L}{c} \left(\frac{1}{(1-R) + \alpha L_s} \right) \quad (1.3)$$

where L_s is the length of the part of the cavity containing the sample. The absorption of the sample at a given wavelength, λ , then, can be extracted from the experimentally measured τ and τ_0 via formula

$$\alpha(\lambda) = \frac{L}{cL_s} \left(\frac{1}{\tau(\lambda)} - \frac{1}{\tau_0(\lambda)} \right) \quad (1.4)$$

The distance the laser pulse travels by the time its intensity drops by a factor of e can be considered as the effective pathlength of this method. For example, in a cavity comprised of mirrors of reflectivity $R = 99.99\%$ placed 0.5 m apart, the effective pathlength is 5 km.

Since the decay rate is independent of the pulse energy, the method is insensitive to laser power fluctuations. The sensitivity of the method is determined by the accuracy of measuring the ringdown time and the baseline loss. This can be better seen if we rewrite equation (1.4), in the case of weak absorption as

$$\delta\alpha_{min} = \frac{L}{cL_s} \frac{\Delta\tau}{\tau_0^2} \quad (1.5)$$

The relative accuracy of measuring the decay time $\Delta\tau/\tau$ is usually constant over a large range of decay times. This means that the lowest measurable $\delta\alpha$ is proportional to the baseline loss $\sim 1/\tau_0$, due to the absorption of the sample or the transmittance of the mirrors. Thus, the sensitivity decreases as the absorption strength increases. For

example, the presence of a strong background absorption will decrease the detection sensitivity of a trace absorber. The bandwidth of the detector and the sampling rate of the data acquisition system limit the shortest measurable ringdown time. Therefore, cavity ringdown spectroscopy has a limited dynamic range and it is not suitable for measurement of strong absorptions.

The fundamental sensitivity limit of cavity ringdown is determined by the shot noise. A 0.5 mJ laser pulse at 1.5 μm consists of 4×10^{15} photons. If the cavity is comprised of 99.99% reflective mirrors, 4×10^7 photons will reach the detector after the first pass resulting in $1/\sqrt{N} = 2 \times 10^{-4}$ statistical noise. However, in practice, there are other factors limiting the sensitivity. One of them is the precision of the A/D conversion of the ringdown signal. For example, if a 8-bit oscilloscope is used for data acquisition, it will digitize the signal with a precision of $1/256=4 \times 10^{-3}$.

Another limitation on applicability of the method is put by the laser linewidth. To obtain the time dependence of the ringdown signal, we have to integrate equation (1.1) over the laser line contour. The described above procedure of measuring absorption can be used only if the decay of the ringdown signal is exponential. If the absorption features are broader than the laser linewidth, we can replace $\alpha(\lambda)$ with its average value. In this case, we will obtain an exponential time dependence, and therefore, the method can be used to measure absorption of any reasonable magnitude. When the widths of the absorption features are comparable or narrower than the laser linewidth, the signal decay is no longer single-exponential. If a single sharp absorption line is present within the laser line contour, the light resonant with the absorber will decay

faster. This leads to a bi-exponential decay of the ringdown signal. The absorbance of the sample, in this particular case, can be measured by fitting the earliest part of the signal. However, this procedure is not practical because it will lead to larger fitting errors in the regions of weak absorption. If several absorption lines are present within the band of laser frequencies, the signal decay will be multi-exponential. As Zalicki and Zare [9] showed, the cavity ringdown technique can still be used, provided the absorption loss in the cavity is much weaker than the mirror loss

$$\alpha L \ll (1 - R) \tag{1.6}$$

If this condition is met, fitting the signal could still be approximately described by a single-exponential function. This puts a very strong limitation on the dynamic range of the method. For example, for mirrors with reflectivity of $R = 99.99\%$, the measured absorption should satisfy the condition, $\alpha L \ll 10^{-4}$. Since, in typical pulsed experiments, the ringdown time is measured with a 0.5-2% error which corresponds to a minimal detected absorbance of 10^{-6} , the method will have the dynamic range of only one order of magnitude $10^{-6} < \alpha L < 10^{-5}$.

We considered above the simplest case of a short laser pulse. If the pulse is longer than the length of the cavity, it overlaps with itself and it is necessary to consider the interference effects. The spectral intensity of the radiation in the cavity depends on many parameters of experiments: the length, width and spectral bandwidth of the laser pulse and its coherence length; the length of the cavity; the radius of curvature, diameter and reflectivity of the mirrors. The general treatment of propagation of a

laser pulse in the cavity is rather complicated. Here, I will qualitatively discuss only some of the effects of this phenomenon.

When the laser pulse is longer than the round-trip length in the cavity, the pulse will start to interfere with itself, leading to the formation of transmission "fringes". The width of the fringes $\Delta\nu$ is inversely proportional to the number of round trips the pulse makes in the cavity $\Delta\nu = \nu_0/N$, where $\nu_0 = c/2L$ is the free spectral range of the cavity [2]. The fringes sharpen as the pulse length increases, and in the limit of infinite pulse, converge to the fringes (modes) of a Fabry-Perot interferometer. Therefore, the method will be measuring the averaged absorption of the sample at the frequencies of the modes of the cavity within the laser linewidth. Furthermore, excitation of multiple modes will result in mode beating in the ringdown signal. This problem can be circumvented through intentional excitation of the transverse modes of cavity. The transverse modes are shifted in frequency from the TEM₀₀ mode, as can be seen from the formula

$$\nu_{qmn} = \nu_{q00} \left[q + (1 + m + n) \frac{2}{\pi} \arctan \left(\frac{d}{[L(2r - L)]^{1/2}} \right) \right] \quad (1.7)$$

where q is the longitudinal mode index, m and n are the transverse mode indexes, and r is the mirror radius of curvature. For a non-confocal cavity, the spacing between the longitudinal and transverse modes is different, and therefore, there is a continuum of transverse modes between every two longitudinal modes. To achieve contribution of the transverse modes to the ringdown signal, it is necessary to minimize diffraction losses at least for several lowest transverse modes which means the diameter of the

mirrors should be much larger than the diameter of the laser beam, and no mode matching optics should be used. This approach has been shown to reduce significantly beating between the longitudinal modes.

However, the arguments presented above are only valid if the pulse is coherent with itself (transform limited). The mode structure is an interference effect and it will only appear when the overlapping parts of the pulse are coherent. For lasers with broad bandwidth, the coherence length will be shorter than any reasonable cavity length and the mode structure will not appear. For example, the dye laser used in our studies generate 5-6 ns pulses with a linewidth of $\Gamma_{laser}=0.15 \text{ cm}^{-1}$. Although the laser pulses are almost 2 m long and slightly longer than the cavity length in our experiments, the coherence length of the pulse is only $\tau_c = 1/(2\pi\Gamma_{laser})=1 \text{ cm}$.

1.2 Experimental apparatus

1.2.1 Near-infrared laser source

The development of dye lasers in the late 1960's provided spectroscopists with a tunable source of laser radiation in the visible and greatly stimulated spectroscopic studies in that spectral region. The development of tunable laser sources in the infrared advanced much slower. In the early days of laser technology, two techniques of generation of the IR light were being developed: downconversion in a non-linear medium and stimulated Raman scattering (SRS). Both methods had their advantages and drawbacks. Optical parametric oscillators and amplifiers required synthesis of

efficient non-linear crystals, as well as development of optical schemes for optimal conversion. At that time, Raman shifters pumped by dye lasers were a cheap and simple alternative to OPOs.

Raman shifting of visible light into the near- and mid-IR is very easy to implement. Relatively high conversion efficiencies (20%) can be achieved for the first Stokes component even in a single-pass cell. However, the tunable range of such a source will be limited by the tunable range of the pump source, and in the case of a dye laser pumped cell it will be only 400-800 cm^{-1} . Although various gases can be used as a Raman medium, molecular hydrogen is usually the medium of choice. The H_2 molecule has the largest vibrational frequency ($\omega_e = 4401 \text{ cm}^{-1}$) and gives the largest Raman shift. Therefore, conversion of visible light into the infrared requires sequential Raman shifting to the second or the third Stokes component. The conversion efficiency of shifting to the higher Stokes components in a single pass is much lower (<3%). Sequential shifting in multi-pass cells requires metal coated mirrors because the mirrors have to be reflective in three or four broad spectral regions. The low damage threshold of the metal coated mirrors as well as gas breakdown at the focus of the beam limit the pump, and therefore, the output energies.

Although work on development of OPOs still continues today, the technology has already matured. Commercially available systems can now provide millijoules of tunable radiation from the UV to the mid-IR with transform limited linewidth, and they have almost replaced dye lasers. Raman shifters are still being used mostly in the far-UV and far-IR regions in which parametric generation of light is not efficient (or

cost-efficient). Since the operating medium (non-linear optical crystals) of OPOs is expensive and requires a high quality pump laser beam, the price of OPO systems and the cost of their maintenance is still significantly higher than the cost of a comparable dye laser system. Stimulated Raman scattering still remains a convenient option of extending the range of a dye laser system into the infrared. For our experiments, we designed and built a multi-pass Raman cell that allowed us to generate tunable laser radiation between 550 nm and 1.7 μm using the available dye laser system. This cell was used as source of near-IR radiation in all cavity ringdown experiments described in chapters 2 and 3.

Stimulated Raman scattering is a non-resonant process of coherent amplification of radiation. If we neglect pump depletion and generation of the higher Stokes components, the power of the first Stokes component will increase exponentially as the beam propagates in the medium

$$P_s(L) = P_s(0)\exp(g_s L), \quad (1.8)$$

where P_s is the power of the first Stokes component and g_s is the Raman gain. The Raman gain coefficient depends on the properties of the medium as well as the intensity and the geometry of the pump beam. The gain is inversely proportional to the beam diameter. Therefore, the conversion efficiency can be increased by focusing the laser beam in the medium [10]. In that case, g_s in equation (1.8) will denote the cumulative focused gain per pass. It has been shown that the Raman gain does not depend on the focal length of the lens. Moreover, for a focused pump beam, the gain

coefficient depends on the pump power, but not intensity

$$g \propto \frac{P_p}{(\lambda_s + \lambda_p)\lambda_s} \arctan\left(\frac{L}{b}\right) \quad (1.9)$$

where P_p is the pump power, λ_p and λ_s are the wavelenghtes of the pump and the first Stokes component, respectively, and b is the confocal parameter.

In practice, Raman shifters are operated in the regime when saturation is reached and the power of the desired Stokes component plateaus as a function of $g_s L$. Small changes of $g_s L$ will only change the distribution of laser power between the pump and the higher Stokes components. However, when saturation is not achieved, the exponential dependence of the Stokes component power on the pump power, gas pressure and the number of passes exhibit a threshold-like effect. The initial power of the Stokes components is zero, and the power build-up starts with a single spontaneously emitted photon (if we disregard four-wave mixing). To reach the power level of a few millijoules, the gain needs to be on the order of 10^{15} - 10^{16} . A multiple-pass arrangement of a Raman cell increases the pass length of the radiation. An n -pass cell will have the exponential Raman gain larger by a factor of

$$\frac{1 - R^n}{1 - R} \quad (1.10)$$

where R is the reflectivity of the mirrors. Silver coated mirrors have reflectivity better than 96% for wavelenghtes above 500 nm. For example, in 3-pass and 17-pass cells, the exponential gains will increase by factors of 2.88 and 12.5, and the total

Raman gain by factors 17.8 and 2.6×10^5 , respectively. Thus, switching from a single-pass to a multi-pass configuration will reduce the pump power threshold by several orders of magnitude.

The task of designing a multi-pass Raman cell was to create a simple and easy-to-align optical system that would periodically refocus the pump and Raman scattered radiation. A simple solution to this problem involved using a pair of metal coated concave mirrors in a Herriott resonator configuration and was first reported by Rabinowitz *et al.* [11]. In this optical configuration first described by Herriott *et al.* [12], the beam injected into the resonator off-axis will, at a certain angle, stay inside the cavity on a path lying on a rotational hyperboloid. The beam spots on the mirrors will form a circle. The angular rotation of the impact point of the beam can be calculated from

$$\theta = \arccos(1 - (d/\rho)), \quad (1.11)$$

where d is the distance between the mirrors and ρ is the mirror radius of curvature.

If there are integer numbers s and m for which

$$2s\theta = 2\pi m, \quad (1.12)$$

then after $2s$ passes, the beam returns to the entrance point and follows the same path again. In this case, the number of beam spots on the mirrors is finite. When the number of passes is small, the beam spots on the mirrors do not overlap and

it is possible to intercept the beam and direct it out of the cell. If we choose θ to satisfy equation (1.12) with $m = s - 1$, then the distance between the mirrors d will need to be very close to 2ρ . Since the focal length of a concave mirror is a half of its radius $f = -\rho/2$, the mirrors will be placed at a distance of $2f$ from the center of the cell. Thus, the injected laser beam initially focused in the middle of the cell will be refocused there after each reflection.

Our Raman cell design is similar to the one introduced by Rabinowitz *et al.* [13]. A 2.2 m long cell contains two 3" diameter 1 m radius-of-curvature (ROC) concave spherical mirrors placed approximately 2 m apart. The mirrors are coated with protected silver coating (SPRAW Industries). Both mirrors have 1" round holes in the middle. The front mirror also has a 0.375" slit (see Fig. 1.7). The cell consists of a 74" long, 3.8" internal diameter tube with 6", 9" ASA flanges (ASA-6 and ASA-9) on the ends, and a 9" ASA nipple (see Fig. 1.6). The back mirror is attached to a 2" optical mount (Newport UltimaTM series) mounted to the 6" flange (see Fig. 1.10). The standard optical screws of the mount are replaced with a longer, 2.5" long 1/4-80 screws, 1.6" long rear parts of which were machined down to 1/8" diameter. The 1/8" diameter parts of the screws are fed through three 1/8" Ultra-torr fittings mounted on the exterior side of the flange. This design allows us to align the back mirror from the outside of the cell. The front mirror is attached to a 1" optical mount (Newport UltimaTM series) suspended on four 1/4-20 threaded rods screwed into the 9" flange. A small 0.5" diameter 1m ROC silver mirror attached to a small mirror mount (9873-K Newfocus) is placed in front of the front 3" Raman mirror. This "pick-off" mirror

intercepts the laser beam after it makes the desired number of passes and directs it out of the cell through the 1" hole in the back mirror. It was necessary to minimize the size of the pick-off mirror and the mirror mount to avoid blocking the laser beam at the adjacent spots. The position of the pick-off mirror is determined by the number of passes before closure and the desired number of passes in the cell. Fig. 1.9 shows the position of the pick-off mirror mount in a 17-pass configuration. Both Raman mirrors and the pick-off mirror are aligned when the cell is open. The 9" nipple is then attached to the cell. The alignment of the mirrors slightly changes when the cell is filled with hydrogen at high pressure. This effect is compensated by adjusting the direction of the entering beam and the tilt of the back mirror. The pump laser beam enters the cell through a 1.5" diameter window on the 9" nipple flange at the distance of 1" from the center of the flange.

The Raman gain coefficient is proportional to the number density of the medium. For a given pathlength of the beam in the cell, the higher the pressure of gas, the lower the pump power threshold for Raman generation. However, in a tight focusing geometry, the Stokes and anti-Stokes components are also generated by four-wave mixing in processes such as $2\omega_p = \omega_s + \omega_{as1}$, $2\omega_{s1} = \omega_{s2} + \omega_p$, *etc.* The generated radiation of the Stokes components can then seed stimulated Raman scattering. The four-wave processes need to satisfy the phase matching conditions which leads to higher divergence of the generated components at higher pressures of hydrogen. Above a certain pressure, the cross-section of the generated beam at a given frequency will no longer be a circle, but a ring. In all of our experiments, the hydrogen pressure in

the cell was maintained between 6 and 9 atm.

A Continuum TDL51 dye laser system pumped by a Continuum NY60 Nd:YAG was used for near-IR generation. The dye laser pulse energy varied from 10 to 40 mJ/pulse, depending on the position relative to the maximum of the dye tuning curve. The linewidth of the dye laser was approximately 0.15 cm^{-1} . Metal mirror coatings are known to have low damage thresholds. In order to avoid damaging the Raman cell mirrors, we propagated the pump beam 10 meters to ensure good beam quality, then expanded with a telescope and focused inside the Raman cell. The pump energy entering the Raman cell was in the 5-20 mJ/pulse range. It was found that at these pump pulse energies, the power of the 2nd Stokes component already reached a plateau after three passes. Therefore, in all of our experiments, we used the cell in the 3-pass configuration.

1.2.2 Flow reactor

The experimental conditions required for generation of radical species vary widely. The commonly used methods include microwave discharge, photolysis, chemical reactions, *etc.* The designed apparatus needed to be able to adapt to various experimental conditions. For that reason, the constructed flow reactor has a modular structure. It consists of cavity mirror mount assemblies, glass adaptors and a flow cell. These elements are connected to each other via Ultra-Torr fittings (Swagelok) so the cell can be easily changed or replaced.

We were not satisfied with the cavity mirror mounts that were commercially avail-

able at the time and we therefore decided to develop our own design. The assembly had to incorporate a standard commercial mirror mount for fine control and stability. Since we had several ongoing cavity ringdown experiments in the group, we intended the design to be easily replicable. For that reason, we preferred to use standard, commercial, off-the-shelf components. A schematic drawing of our mirror mount assembly is shown in Fig. 1.13. The assembly consists of two modified ASA-5 flanges, a cylindrical spacer and a standard commercial kinematic mirror mount (Newport 1" Ultima). The cell is connected to the mirror mount assemblies via 3/4" Ultra-Torr fittings welded on the outer side of the front flanges. The front flanges are bolted to home-made aluminum stands approximately 8.5" above the laser table. The assembly is held together by four 1/4-20 bolts that are screwed into the front flange from the back, passing through 1/4" holes in the back flange. The aluminum spacer is a piece of a standard off-the-shelf aluminum tube (2.75" inside diameter, 3.5" outside diameter) with a 1/4" NPT tapped hole on the side to allow a flow of inert gas to purge the mirrors. Both flanges have a 0.1" high 2.75" diameter steps on the inner sides and a 9/32" o-ring groove. The inside diameter of the spacer is adjusted to fit tightly to the steps on the flanges. This insures stability of the position of the back flange. The kinematic mirror mount is bolted to the back flange by two screws. Since the sensitivity of cavity ringdown spectroscopy depends on the reflectivity of the cavity mirrors it is necessary periodically to clean the cavity mirrors. The mirror mount units can be easily disassembled to access the mirrors and reassembled without losing the alignment of the cavity. The cleaning procedure including reassembling the

mounts usually takes only ten minutes.

The cavity mirrors are aligned in the same manner as the back mirror of the Raman cell. The standard optical screws in the mirror mount were replaced with 2.7" long 1/4-80 screws(Newfocus), the rear parts of which were machined down to 1/8" diameter and fed through 1/8" Ultra-Torr fitting mounted on the outer side of the back flange. The near-IR radiation enters and exits the cell through 1" diameter windows mounted on the exterior side of the back flange and sealed with o-rings.

Different cells can be used in our apparatus, depending on the requirement of the experiment. A cell can be connected directly to the mirror mount assemblies if it has 3/4" tube ports. Otherwise, it is necessary to use adaptors. Both cells used in the experiments described in chapters 2 and 3 had 1/2" ports and were connected to the mirror mounts via simple pyrex adaptors with 1/2" Ultra-Torr unions (see Fig. 1.11).

In our studies of photolytically-produced radicals, a 17.5 cm long quartz cell was used. The cell consisted of a 1/2" diameter round quartz tube with a 4.5 cm long 1 × 1 cm square piece fused in the middle (see Fig. 1.12). The reactants were photolyzed in the square part of the cell. The gas inlet and pump port were 7 cm apart. The reactants were photolyzed by the UV radiation of an excimer laser (Lambda-Physik EMG-103) that entered the cell perpendicularly. The UV radiation was focused by a cylindrical lens into a 0.5 × 4 cm rectangle in the cell. The chosen setup although the least efficient in terms of the number density of generated radicals was the simplest to implement. To maximize the number density of radicals in the cavity, it is necessary to maximize the overlap between the excimer and the near-IR laser beams. Most of

the cavity mirrors used in our experiments had a radius of curvature 1 m. This limited the size of the cavity to 1 m and the reagent part of the cell to about 50 cm. Thus, collinear geometry could give us in principle an order of magnitude increase in the signal. However, to achieve such a long overlap, the beams would need to intersect at an angle smaller than 5° , which requires a more complicated mirror mount design. Since we had a sufficient signal-to-noise ratio in our experiments on peroxy radicals, we chose to perform measurements using this simple setup. The distance between the cavity mirrors in this geometry was 54 cm.

We built several long cells for measuring absorption of relatively stable species. A schematic drawing of the cell used in the NO_3 experiments is shown in Fig. 1.12. The cell consists of a 50 cm long $1/2''$ diameter pyrex tube with a $1/2''$ gas inlet and a $1/2''$ pump port placed 40 cm apart. When the cell was used, the distance between the cavity mirrors (which included the purge volumes) was 78 cm. The pressure in both cells was measured by a capacitance manometer (MKS BaratronTM, 1000 Torr) through a $1/4''$ port located by the pump port.

1.2.3 Instrument control and data acquisition

The radiation exiting the cavity was focused onto the photodetector with a 5 cm focal-length lens. Several 1 mm diameter photodiodes were used as photodetectors including an unamplified extended InGaAs photodiode (Hamamatsu), and InGaAs and Si photodiodes with built-in transimpedance amplifiers (Thorlabs PDA400 and PDA155). The signal from the photodetector was amplified by a home-built amplifier

(CLC401 OpAmp) with a gain of 50 and recorded by a digital oscilloscope (Tektronix 320) or a transient digitizer computer board (Gage Compuscope 1012).

Only about 0.01% of the laser power at the frequency of interest enters the cavity. Furthermore, the power of a 5-6 ns laser pulse trapped inside leaks out of the cavity over $\approx 10 \mu\text{s}$ time period leading to another three order of magnitude decrease of the peak intensity of the signal. Thus, it is necessary to suppress the power of the pump and other Stokes components by at least seven orders of magnitude. When the sufficient suppression was not achieved, we observed a very strong signal at time zero. In that case, the early part of the ringdown signal usually 0.5-1 μs was discarded.

Instrument control and data acquisition were performed by a personal computer (PC, Intel Pentium II 400 MHz) equipped with several expansion boards. They included a GPIB interface board (National Instruments), digital input/output (I/O) board (Measurement Computing PCI-DIO24H, 24-Bit, 64 mA), analog I/O board (Measurement Computing PCI-DAS6034, 16 analog channels at 200 kS/s, 8 digital I/O channels, and 2 counter/timers) and transient digitizer (Gage Compuscope 1012, 2 channels, 20MS/s combined). The lasers and data acquisition were synchronized by two digital delay generators (Stanford Research Systems DG535). A schematic diagram of electronic communication between different parts of the instrument is shown in Fig. 1.4. A Visual Basic computer program was written to control the dye laser and the delay between the YAG and the excimer lasers, and to collect ringdown waveforms and fit them to an exponential decay.

To insure the power stability of a pulsed YAG laser, it is necessary to operate

its flashlamp at a constant rate. The average temperature of the YAG rods, the temperature gradient, and the pulse energy depend on the repetition rate of the flashlamp. The thermal gradient in the rod gives rise to a refractive index gradient the so called "thermal lensing" and can cause focusing of the laser beam. In the NY-60 model, this effect was compensated by a slightly concave back mirror of the oscillator cavity. The radius of curvature of the mirror is a function of the repetition rate. The laser used in our experiments had been optimized to run at 20 Hz, which determined the repetition rate of our experiment. We chose to run the experiment at 19 Hz to avoid always being in phase with the 60 Hz noise introduced by the power lines.

One of the digital delay generators was triggered internally at 19 Hz and provided the clock for the experiment. This delay generator triggering the flashlamp discharge and the Q-switch of the YAG laser was constantly operating. The second delay generator triggered the excimer laser, the oscilloscope and the A/D boards in the computer. The settings of this generator were controlled by the data acquisition computer via a GPIB bus.

In initial experiments, waveforms were recorded with a digital oscilloscope (Tektronix 320) which had a bandwidth of 100 MHz, 8-bit A/D resolution and a digital record length of 1000 points. Since the energy of the laser pulses fluctuated from shot to shot, the oscilloscope gain was chosen to keep the average amplitude of the signal by at least a factor of two smaller than the digitizing range. This effectively limited our A/D resolution to 1/128. The waveforms were averaged by the oscilloscope with

16-bit precision, and then the 1000-point 16-bit integer buffer was read into the PC RAM via a GPIB bus. The total number of waveforms was limited to 256; however, only 20 waveforms were normally averaged. Later, the computer was upgraded with a Compuscope 1012 board that had a 12-bit A/D resolution and 20 MHz bandwidth (single channel mode). The bandwidth of the board, however, was sufficient for our experiments. The ringdown time, τ_0 in our experiments stayed in the 7-25 μs range. Typically, the ringdown signal was recorded in the interval from $t = 0$ to $t = (5-6)\tau_0$, resulting in 1500-2500 data points per waveform. Unfortunately, the DC offset on the board could not be changed. Thus, the effective A/D resolution was only 1/1024. This gave us a factor of eight improvement in digitizing noise. A 4096 point block of on-board memory was read into PC RAM after each shot. Then, the desired number of waveforms were averaged in a buffer of single precision floating point variables. Although the board was connected via a now obsolete ISA bus, the data transfer rate was sufficiently fast to acquire data at 19 Hz. All spectra shown in chapters 2 and 3 were obtained with the Compuscope 1012 board.

Both the oscilloscope and the Compuscope board were triggered approximately 20 μs before the YAG laser fired. The first 10-15 μs of the waveform were used to calculate the DC offset of the signal. The offset was then subtracted from the waveform before fitting it in order to lower the number of parameters of the fit. The part of waveform starting at time $t=0-1 \mu s$ was fit to a single-exponential decay with two adjustable parameters

$$y = ae^{bt} \tag{1.13}$$

using NL2SOL algorithm [14]. This was implemented by calling a dynamic link library (dll) compiled using the original FORTRAN code of J. E. Dennis *et al.*

Originally, the dye laser was controlled by an XT computer supplied by the manufacturer. To simplify instrument control and increase the data collection rate, the data acquisition computer was set up to control the dye laser directly by sending 5 V pulses directly to the laser's stepping motor controller. The PCI-DIO24H board with external pull-up resistors provided the pulses with required current (30 mA). The data acquisition program scanned the wavelength of the dye laser, collected and fitted the ringdown waveforms, and saved $1/\tau$ in a file as a function of the laser wavelength. Since $1/\tau_0$ changes as a function of wavelength, it is necessary to perform a background scan in order to take this change into account. If the species of interest are generated by photolysis, both scans can be performed simultaneously. The delay generator that triggers the excimer laser and the A/D board (or oscilloscope) is controlled by the data acquisition computer through a GPIB bus. Thus, at each wavelength during the scan, background absorption can be measured by turning off the excimer laser. This procedure excludes the long-term changes of the reflectivity of the cavity mirrors and the pressure of the precursor gases.

In photolysis experiments, it is also possible to measure the decay rate of produced radicals by monitoring absorption at a given wavelength as a function of time. In this case, the program changes the timing between the trigger pulses of the YAG and excimer lasers, and records $1/\tau$ as a function of the UV-NIR delay.

The 6000-8000 cm^{-1} region contains relatively strong overtones of the C-H and

O-H stretching vibrations of many molecules which can be used for calibration of the laser. These transition are strong enough to be detected by photoacoustic spectroscopy at concentrations of several Torr. A home-built photoacoustic cell was set up to verify the calibration of the laser during cavity ringdown scans. The cell consisted of a 10 cm long 1" diameter aluminum tube with glass windows and a small electret microphone (Knowles Acoustics EK-3132) mounted inside. When the cell is used for calibration, about ten percent of the near-IR radiation output of the Raman cell is split and directed into it. The signal from the microphone was amplified by a factor of 100 and then digitized by the PCI-DAS6034 board. The first period of the acoustic wave is integrated and recorded as a function of wavelength.

1.3 Instrument characteristics

To assess the performance and sensitivity of our instrument, we performed several scans of stable species spectra of which are well-known and catalogued. Fig. 1.19 and 1.20 show spectra of CO₂ (7580-7610 cm⁻¹) and air (9200-9400 cm⁻¹) recorded with our instrument in the long-path cell and simulated spectra of CO₂ and H₂O with 0.15 cm⁻¹ resolution based on the data from HITRAN database [15]. Newport 1 m ROC mirrors (different sets) were used in both scans. The cavity length in these scans was $L = 78$ cm. Twenty waveforms were averaged at each wavelength. The CO₂ spectrum was recorded at the pressure of 10 Torr. The spectrum of air that contained mostly water lines was measured at atmospheric pressure and humidity. We routinely use H₂O absorption features to calibrate our laser. This was one of the

scans taken for that purpose.

From equation (1.4), we can see that the minimal detectable fractional absorption is proportional to the error in determination of $1/\tau$

$$\left(\frac{\Delta I}{I}\right)_{min} = \frac{L}{c} \delta\left(\frac{1}{\tau}\right)_{min} \quad (1.14)$$

The noise level in the CO₂ spectrum equals $\delta\left(\frac{1}{\tau}\right) \approx 340 \text{ s}^{-1}$ which yields the sensitivity limit of $(\Delta I/I)_{min} = 9 \times 10^{-7}$ for our instrument. This number can easily be improved by a factor of 2-3 by using mirrors with higher reflectivity that are currently commercially available.

I would also like to point out the presence of the "saturation" effect in the CO₂ spectrum. The relative intensities of the weak 7590.5, 7592.1, 7594.5, 7696 and 7597.5 cm⁻¹ bands in the cavity ringdown spectrum and the spectrum generated from HITRAN database are similar. The intensities of the stronger bands in both P and R branches plateau at the level of the 7597.5 cm⁻¹ band. This is a clear manifestation of the laser bandwidth effect mentioned above. The Doppler linewidth (FWHM) of CO₂ transitions at room temperature is $\approx 0.013 \text{ cm}^{-1}$. The pressure broadening coefficient for the lines in this region is $\approx 0.01 \text{ cm}^{-1}/\text{atm}$, which at 10 Torr gives a negligible contribution to the total linewidth. Therefore, the width of the absorption features of CO₂ is a factor of 10 narrower than the laser bandwidth. As discussed above, in the case when the absorption features are narrower than the laser bandwidth, the ringdown decay is no longer single-exponential and cavity ringdown spectroscopy can be used only if the absorption is weak (equation (1.6)). Therefore, we can use our

instrument for CO₂ spectroscopy only when $1/\tau < 1.1/\tau_0$, i.e., when the total absorption is less than 10% of the mirror loss. This observation is in agreement with equation (1.6).

The spectrum of air demonstrates that when the width of the absorption features becomes comparable with the laser linewidth, this limitation is lifted. The pressure broadening effect increases the widths of the water lines to $\approx 0.1 \text{ cm}^{-1}$ at 1 atm. The relative intensities of the observed H₂O lines are in good agreement with the intensities recorded in HITRAN database. The upper bound of the dynamic range of the instrument in this case is larger than 400% of the mirror loss.

1.4 Summary

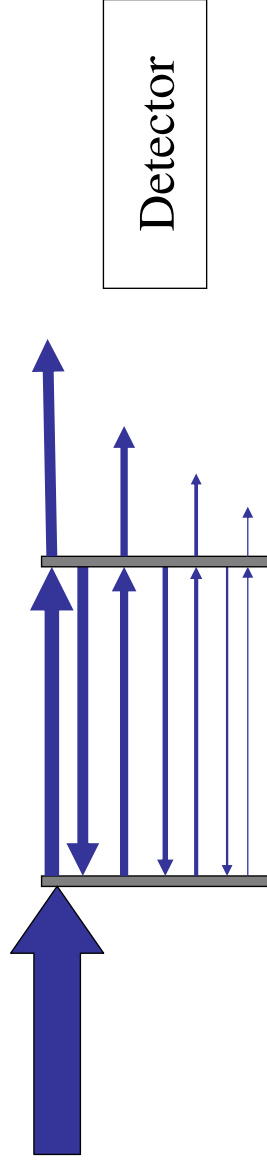
We constructed a flow cell near-IR cavity ringdown spectrometer that employs a multi-pass Raman shifter as a source laser radiation. The maximum pathlength is approximately 50 cm. The instrument has been operated in the 5900-10700 cm^{-1} region, although the tunable range can easily be extended to 5000 cm^{-1} . With currently available cavity mirrors (100 ppm transmission), the sensitivity of the instrument is $(\Delta I/I)_{min} = 9 \times 10^{-7}$ per pass at 20 Hz. Due to a limitation of the method, the dynamic range of the instrument is only one order of magnitude for systems with absorption features narrower than the laser bandwidth. For systems with broad absorption features, the dynamic range is at least 600.

References

- [1] A. O’Keefe and D. A. G. Deacon. *Review of Scientific Instruments*, 59(12):2544–2551, 1988.
- [2] J. J. Scherer, J. B. Paul, A. Okeefe, and R. J. Saykally. *Chemical Reviews*, 97(1):25–51, 1997.
- [3] J. B. Paul, C. P. Collier, R. J. Saykally, J. J. Scherer, and A. Okeefe. *Journal of Physical Chemistry A*, 101(29):5211–5214, 1997.
- [4] J. P. Maier. *Journal of Physical Chemistry A*, 102(20):3462–3469, 1998.
- [5] R. T. Jongma, M. G. H. Boogaarts, I. Holleman, and G. Meijer. *Review of Scientific Instruments*, 66(4):2821–2828, 1995.
- [6] J. J. Scherer, D. Voelkel, and D. J. Rakestraw. *Applied Physics B-Lasers and Optics*, 64(6):699–705, 1997.
- [7] A. C. R. Pipino, J. W. Hudgens, and R. E. Huie. *Chemical Physics Letters*, 280(1-2):104–112, 1997.
- [8] T. Yu and M. C. Lin. *Journal of the American Chemical Society*, 115(10):4371–4372, 1993.

- [9] P. Zalicki and R. N. Zare. *Journal of Chemical Physics*, 102(7):2708–2717, 1995.
- [10] A. De Martino, R. Frey, and F. Pradere. *IEEE Journal of Quantum Electronics*, 16(11):1184–1191, 1980.
- [11] P. Rabinowitz, A. Stein, R. Brickman, and A. Kaldor. *Applied Physics Letters*, 35(10):739–741, 1979.
- [12] D. Herriott, R. Kompfner, and H. Kogelnik. *Applied Optics*, 3(4):523–526, 1964.
- [13] P. Rabinowitz, B. N. Perry, and N. Levinos. *IEEE Journal of Quantum Electronics*, 22(6):797–802, 1986.
- [14] J. E. Dennis, D. M. Gay, and R. E. Welsch. *ACM Transactions on Mathematical Software*, 7(3):369–383, 1981.
- [15] L. S. Rothman, A. Barbe, D. C. Benner, L. R. Brown, C. Camy-Peyret, M. R. Carleer, K. Chance, C. Clerbaux, V. Dana, V. M. Devi, A. Fayt, J. M. Flaud, R. R. Gamache, A. Goldman, D. Jacquemart, K. W. Jucks, W. J. Lafferty, J. Y. Mandin, S. T. Massie, V. Nemtchinov, D. A. Newnham, A. Perrin, C. P. Rinsland, J. Schroeder, K. M. Smith, M. A. H. Smith, K. Tang, R. A. Toth, J. Vander Auwera, P. Varanasi, and K. Yoshino. *Journal of Quantitative Spectroscopy & Radiative Transfer*, 82(1-4):5–44, 2003.

Pulsed CRDS



$$I(t) = I_0 \exp\left[-\frac{t}{\tau_0}\right]$$

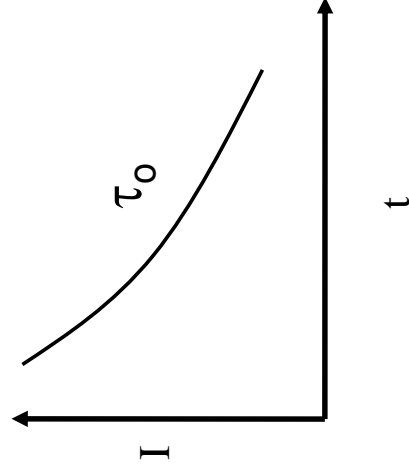


Figure 1.1: The principle of pulsed cavity ringdown spectroscopy. The pulse (its coherence length) is shorter than the cavity.

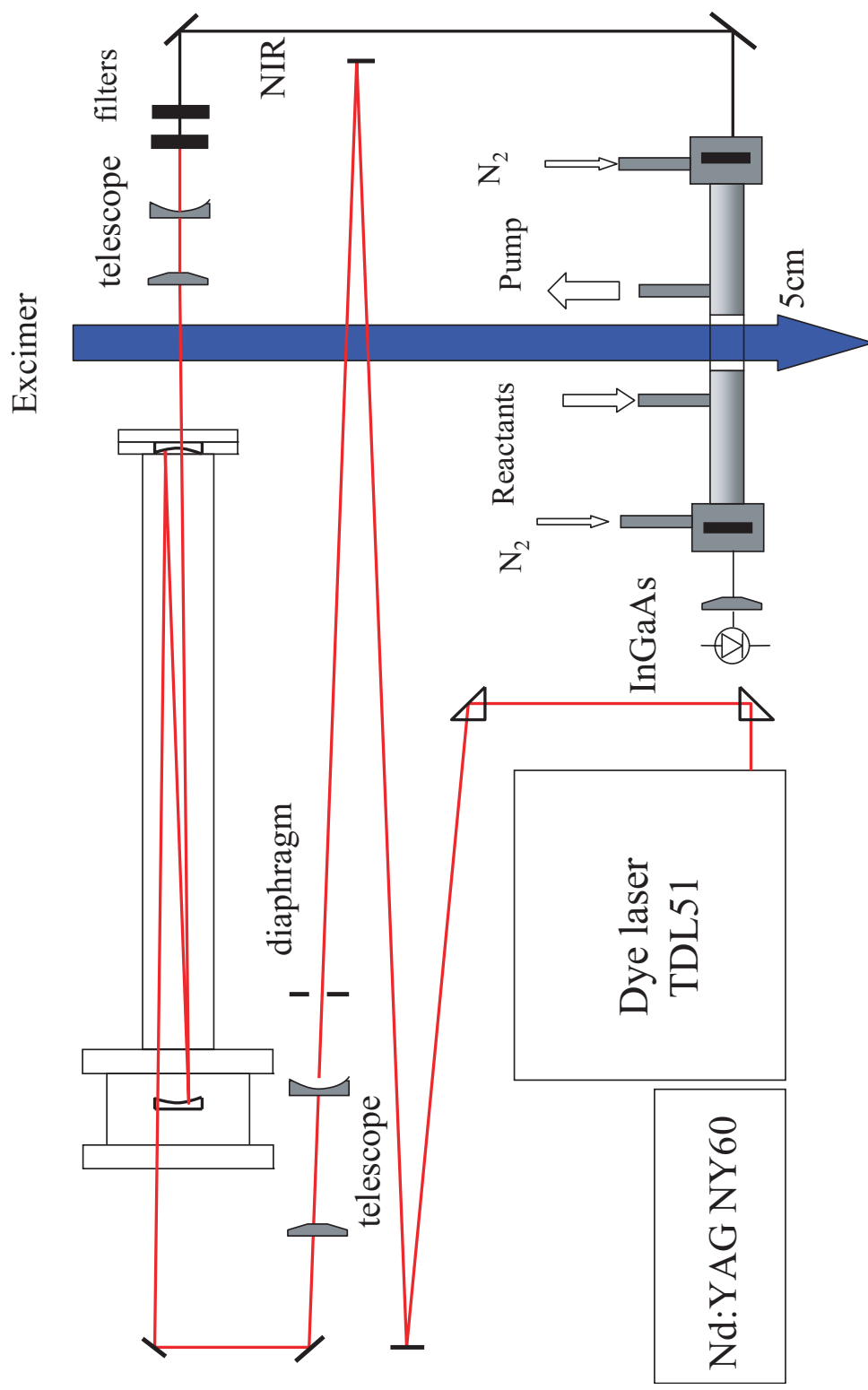


Figure 1.2: Optical layout of NIR-CRDS apparatus in photolysis experiments.

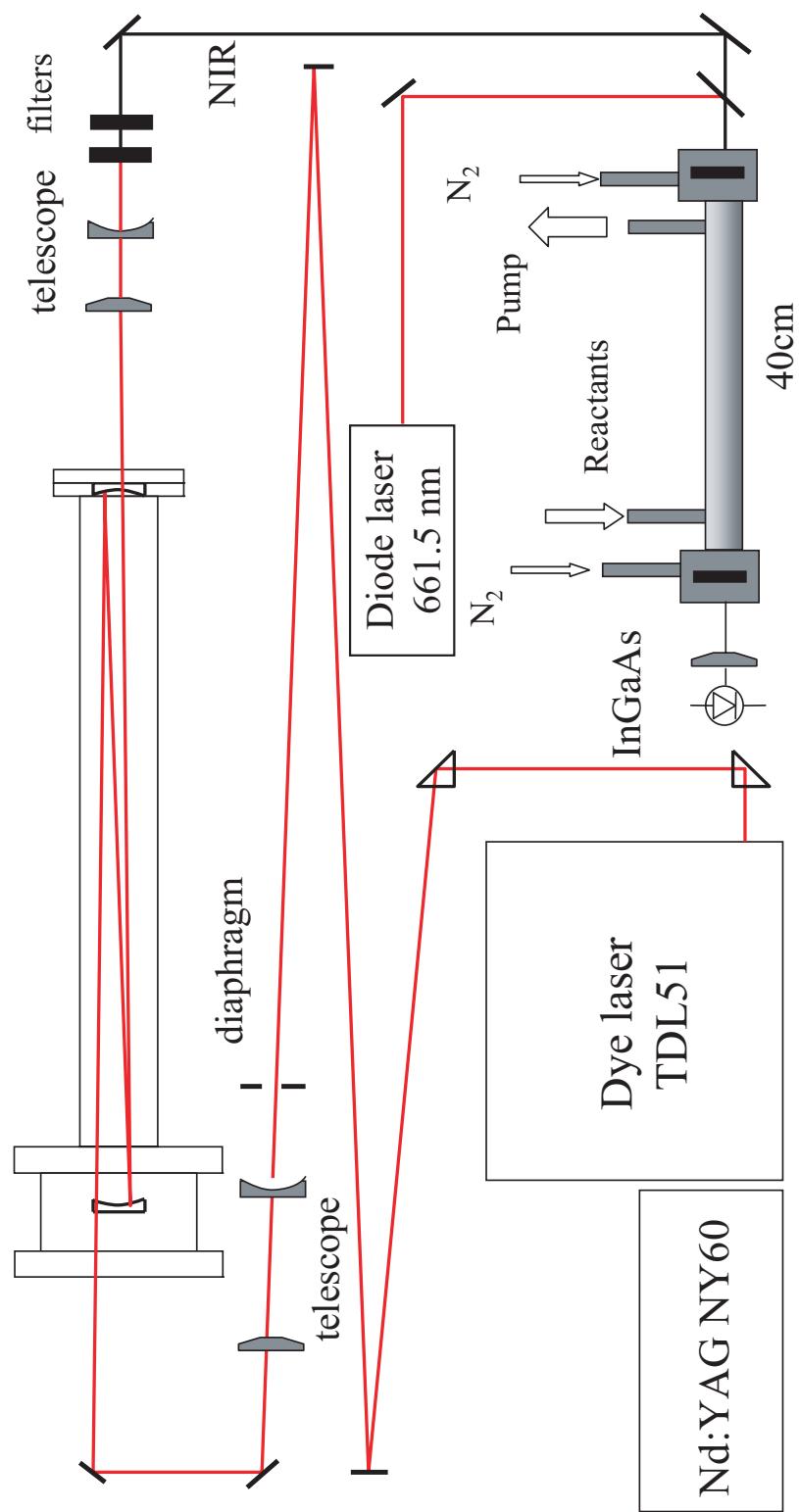


Figure 1.3: Optical layout of NIR-CRDS apparatus with a long-path cell. A diode laser is used to measure the absolute concentration of NO₃ through direct absorption at 661.5 nm.

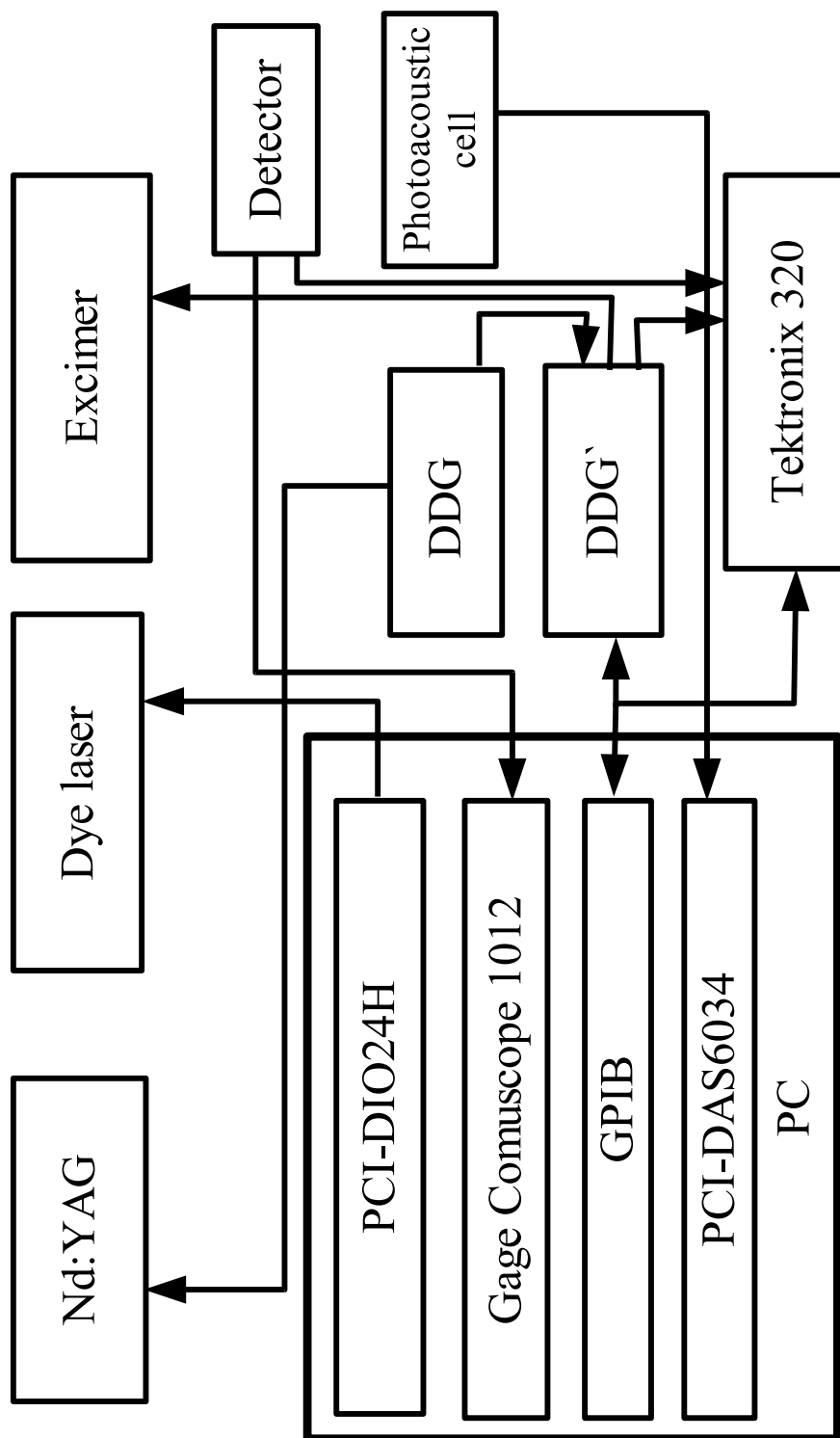


Figure 1.4: Schematic diagram of components of Cavity ringdown spectrometer.

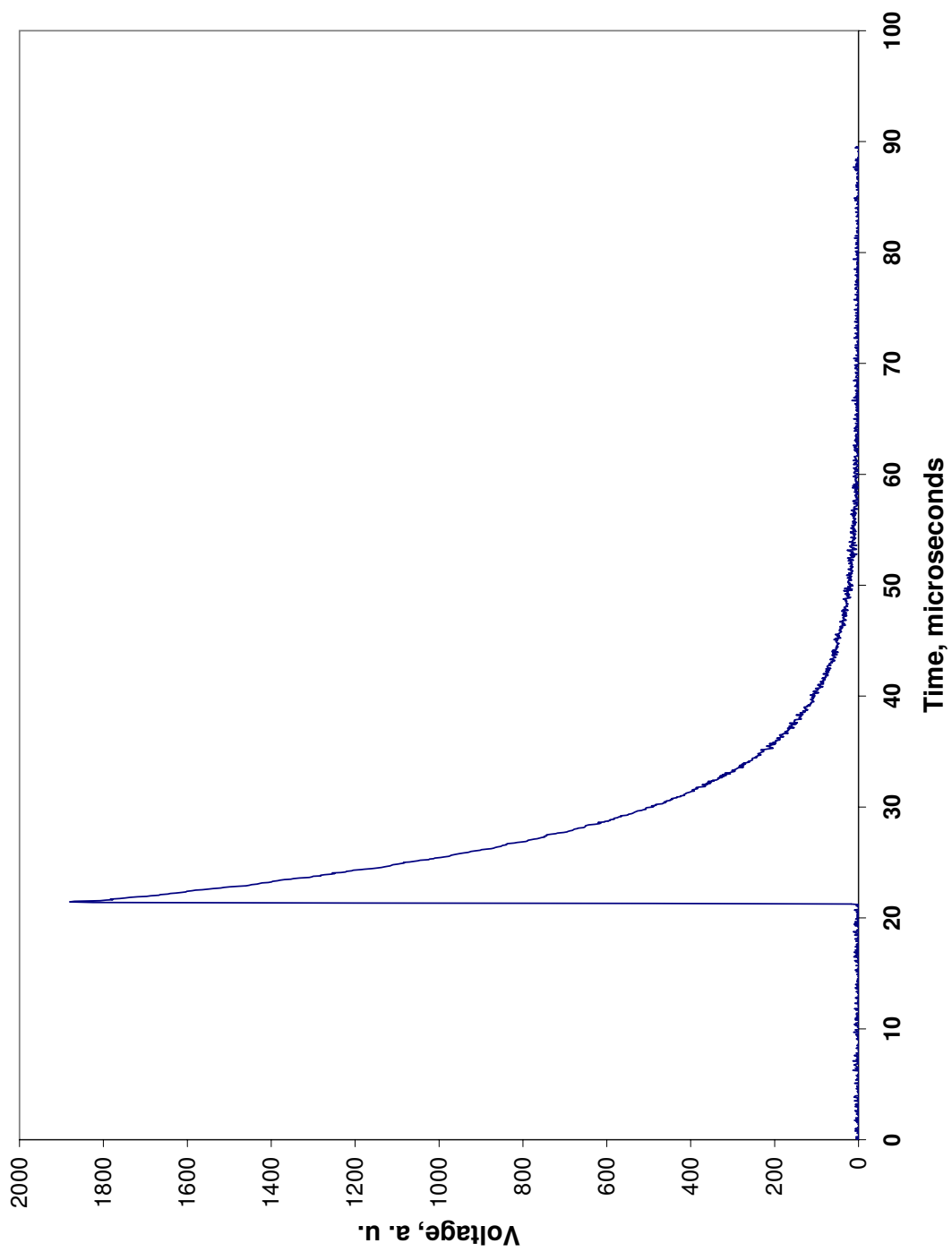


Figure 1.5: Typical ringdown trace, average of 20 shots.

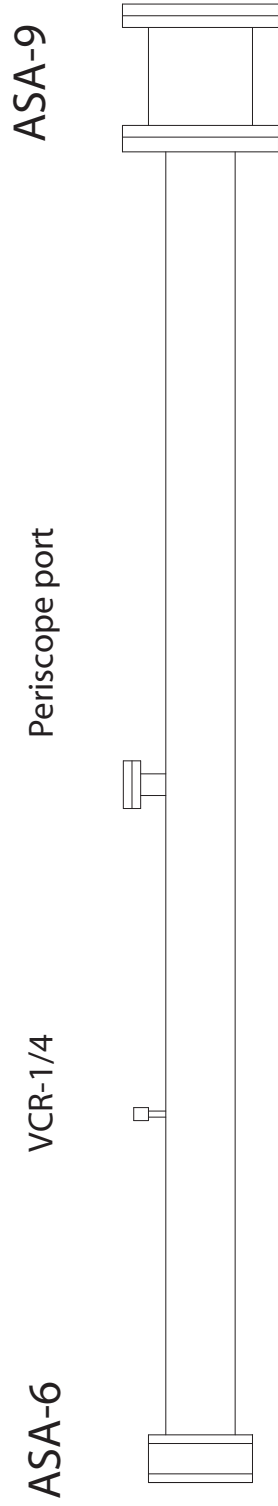


Figure 1.6: Drawing of the Raman cell - side view.

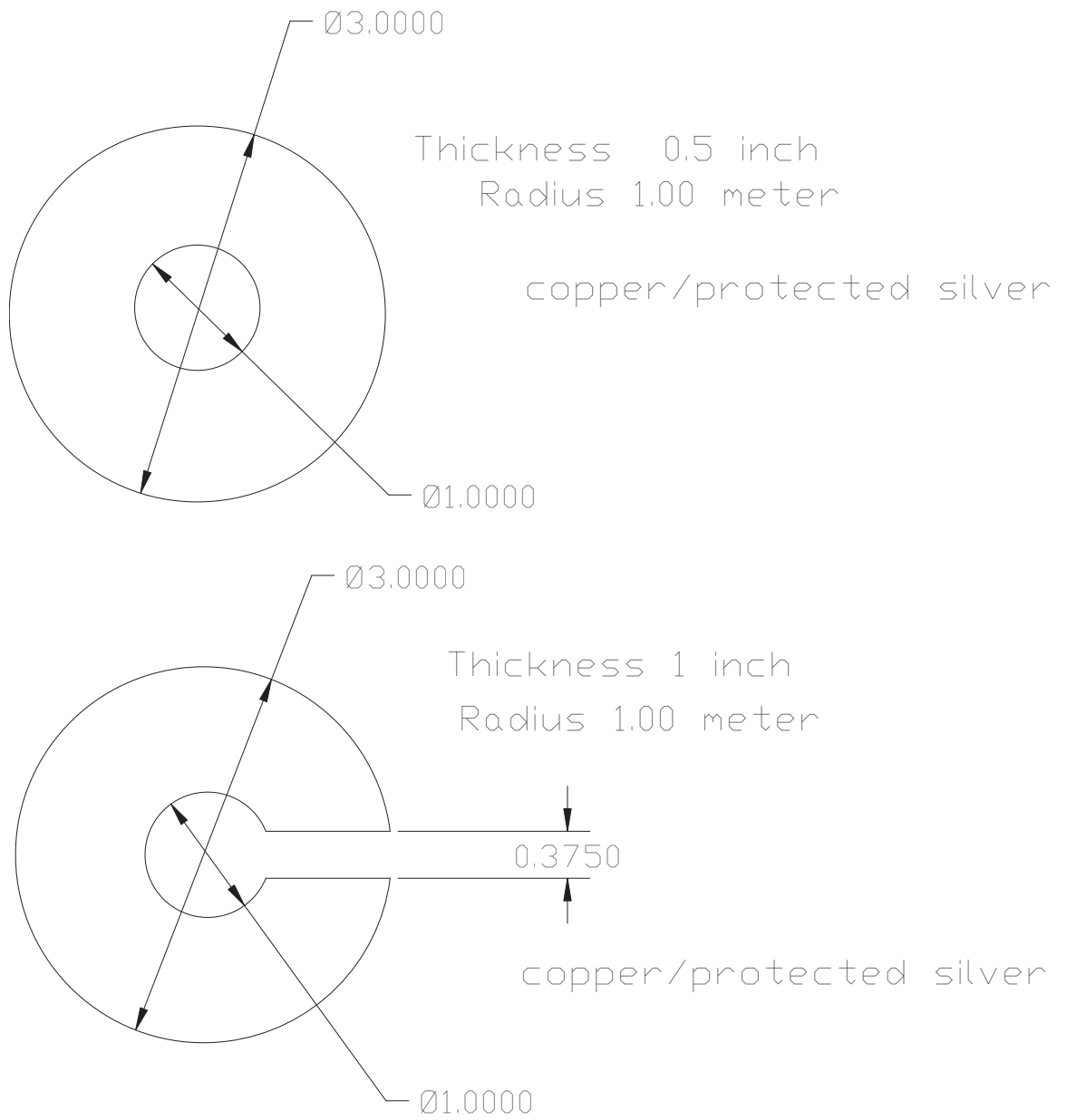


Figure 1.7: Drawing of the Raman cell mirrors. All dimensions are in inches.

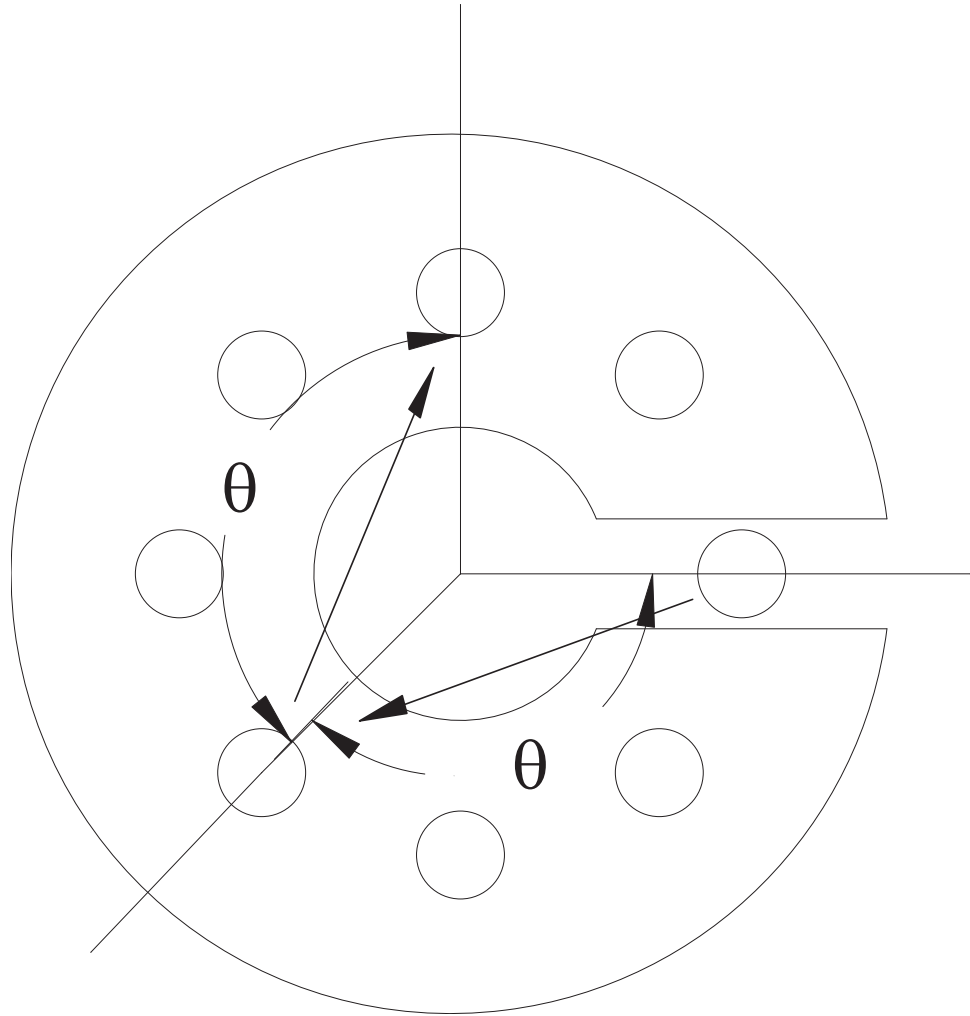


Figure 1.8: Optical path of laser beam in a Herriott cell.

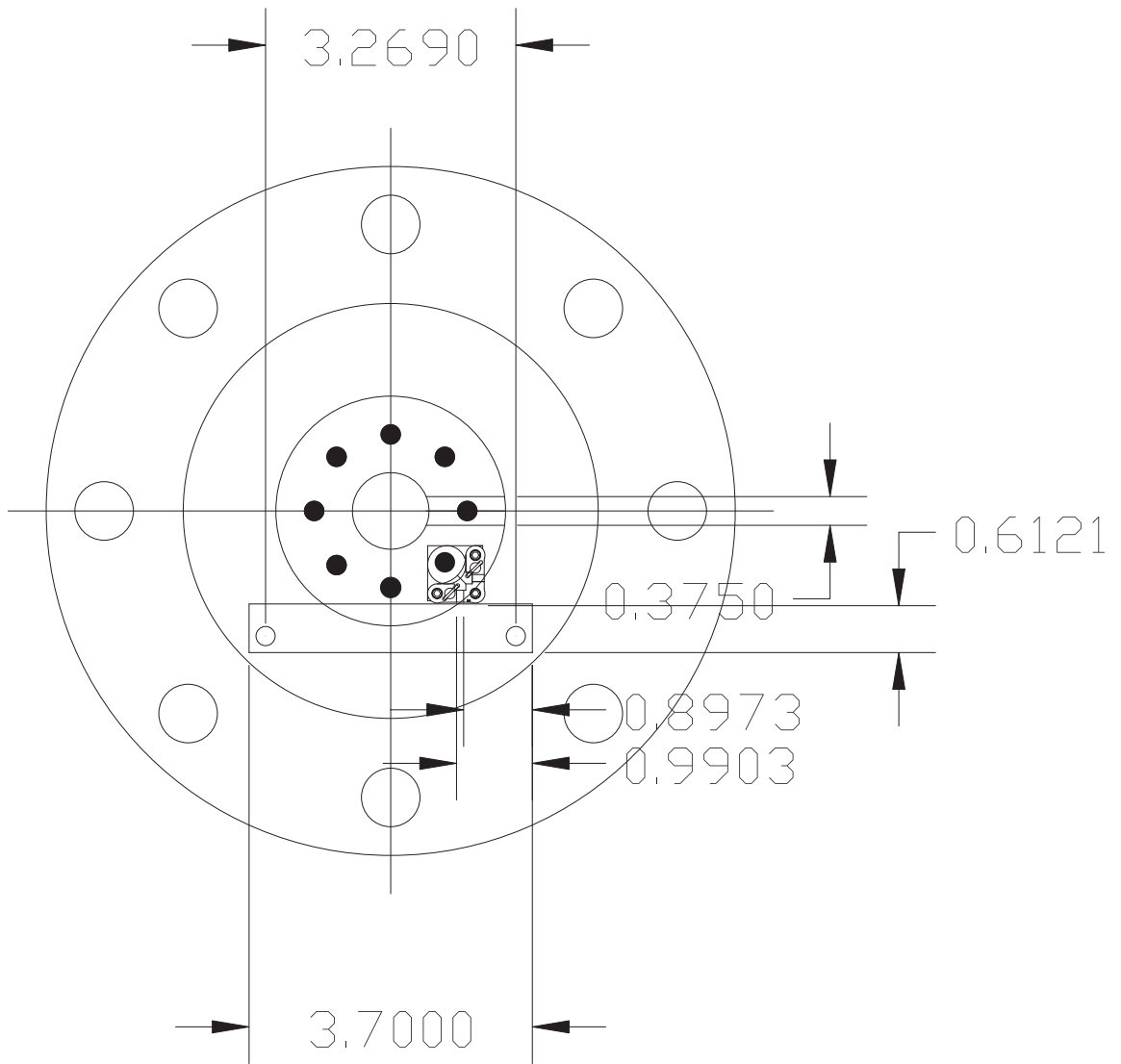


Figure 1.9: Drawing of the pick-off mirror mount - front view, 17-pass configuration. All dimensions are in inches.

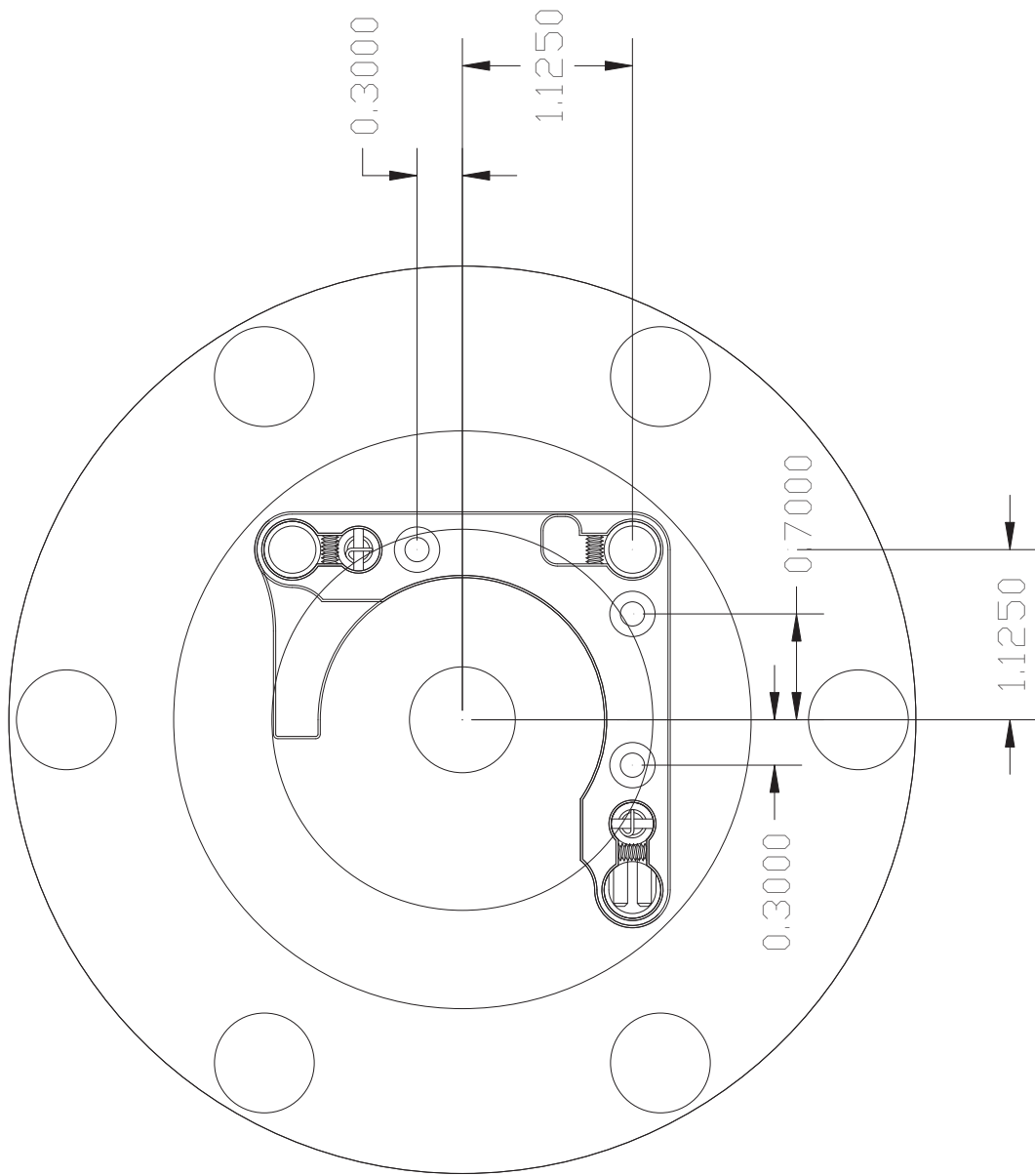


Figure 1.10: Drawing of the back Raman cell mirror mount - interior view of the 6" ASA flange. All dimensions are in inches.

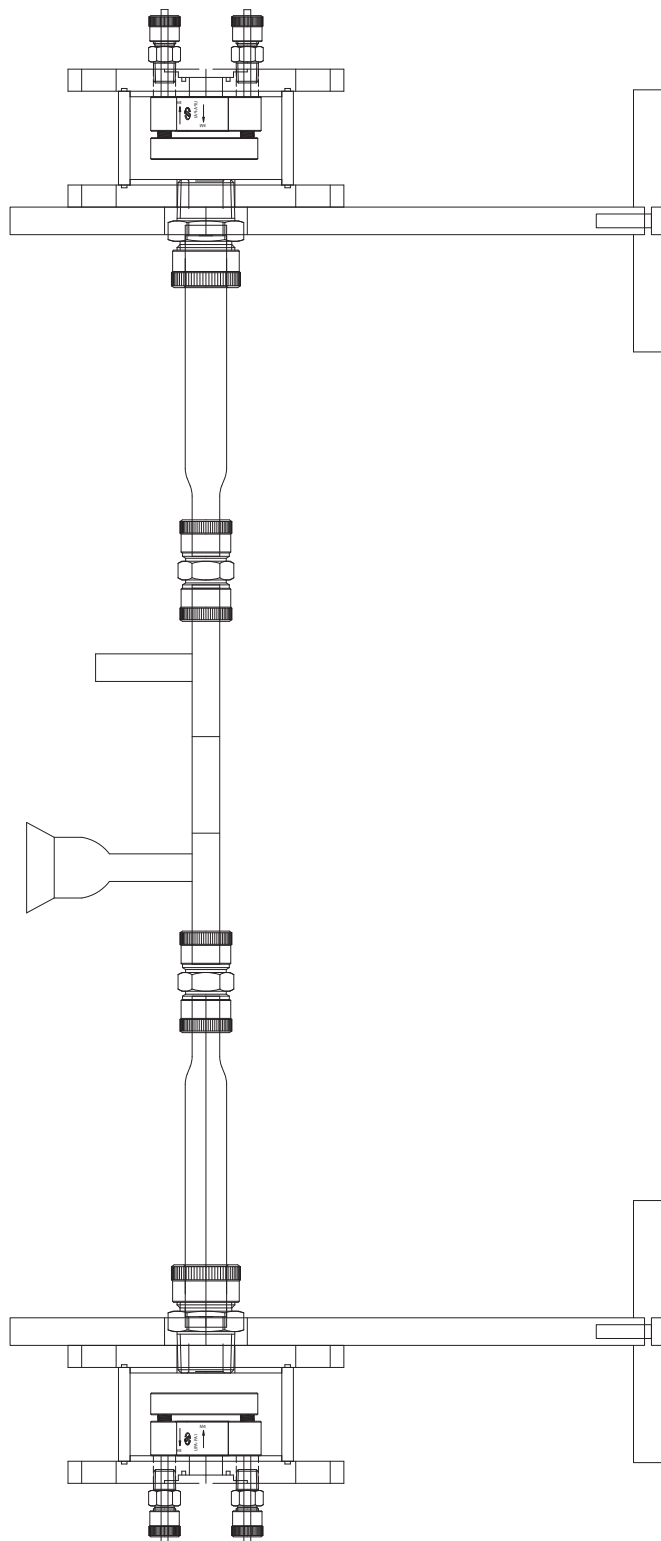


Figure 1.11: Assembly drawing of the flow reactor with the photolysis cell.

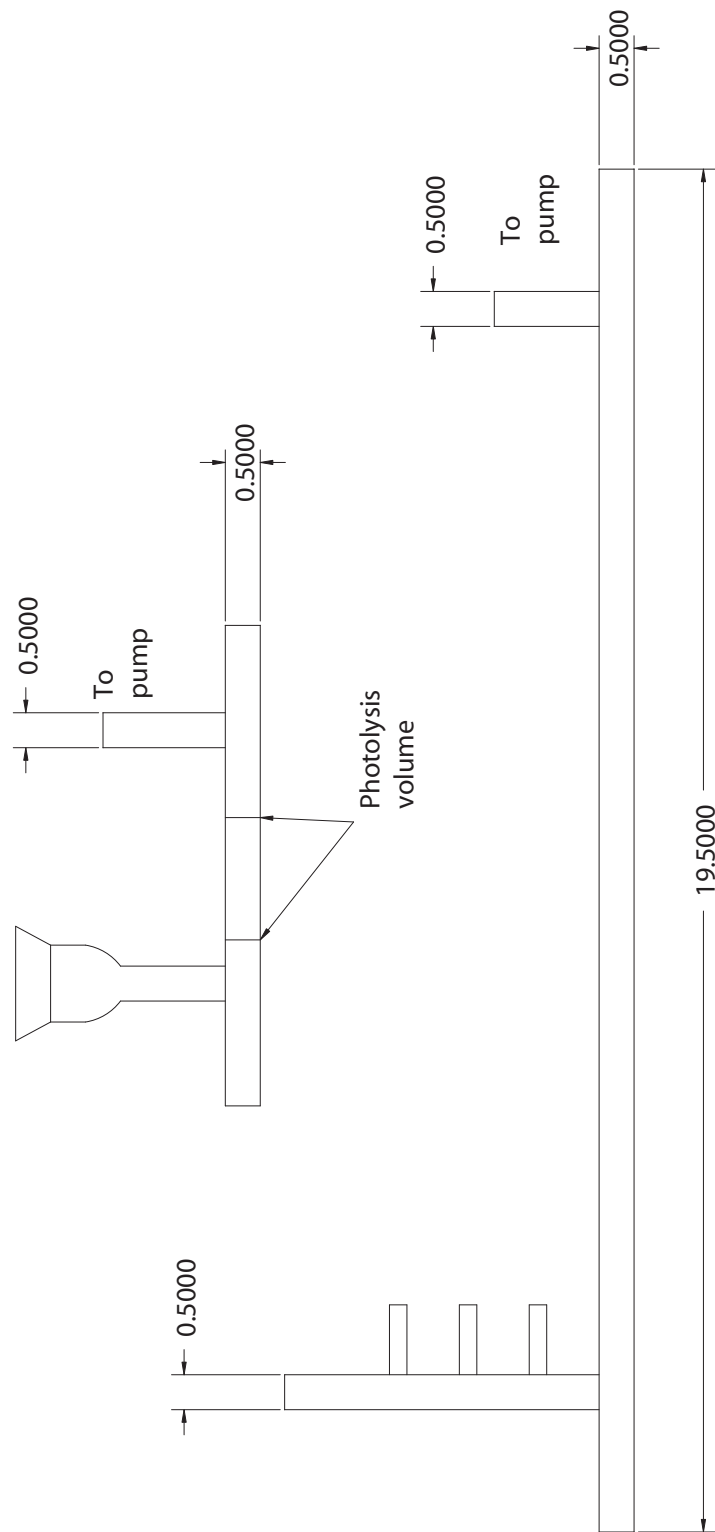


Figure 1.12: Drawings of the cells used in experiments described in chapters 2 and 3. All dimensions are in inches.

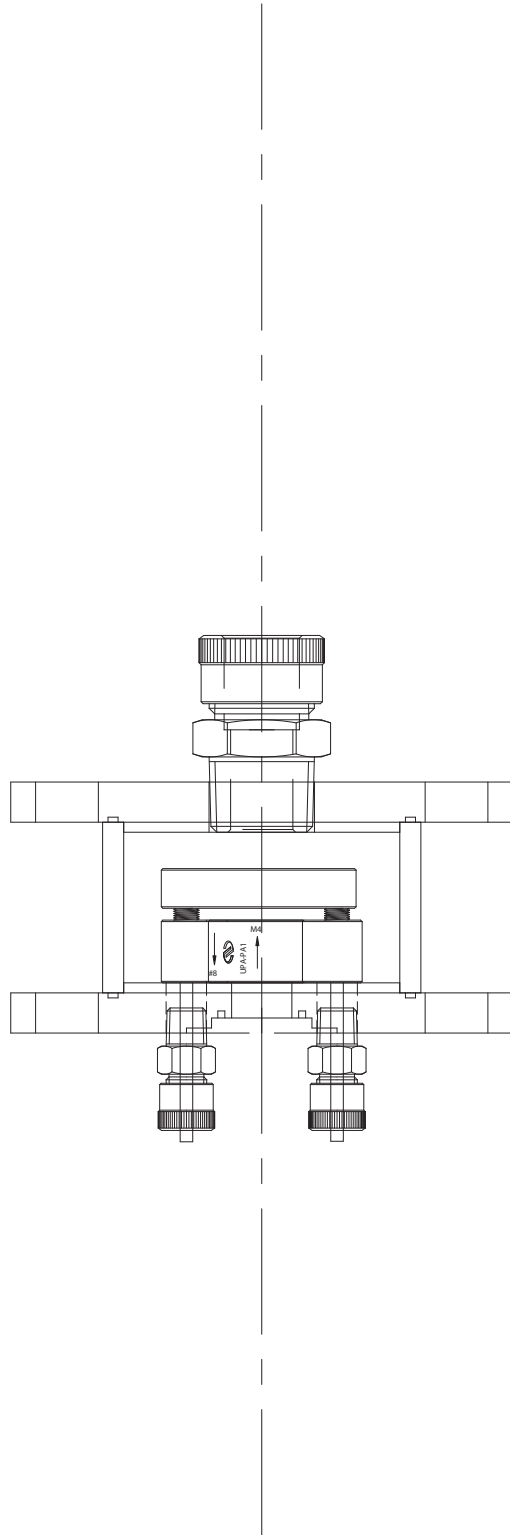


Figure 1.13: Assembly drawing of the cavity mirror mount.

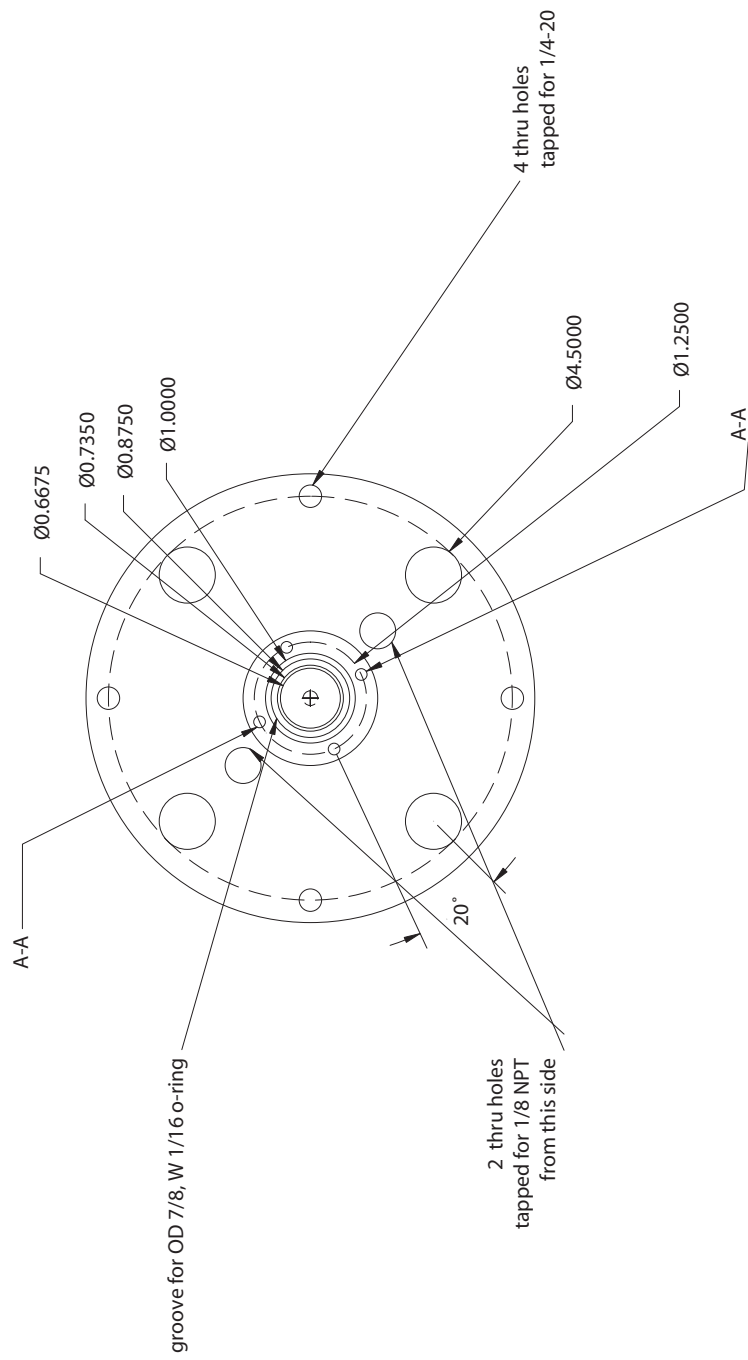


Figure 1.14: Drawing of the back flange of the cavity mirror mount - exterior view.

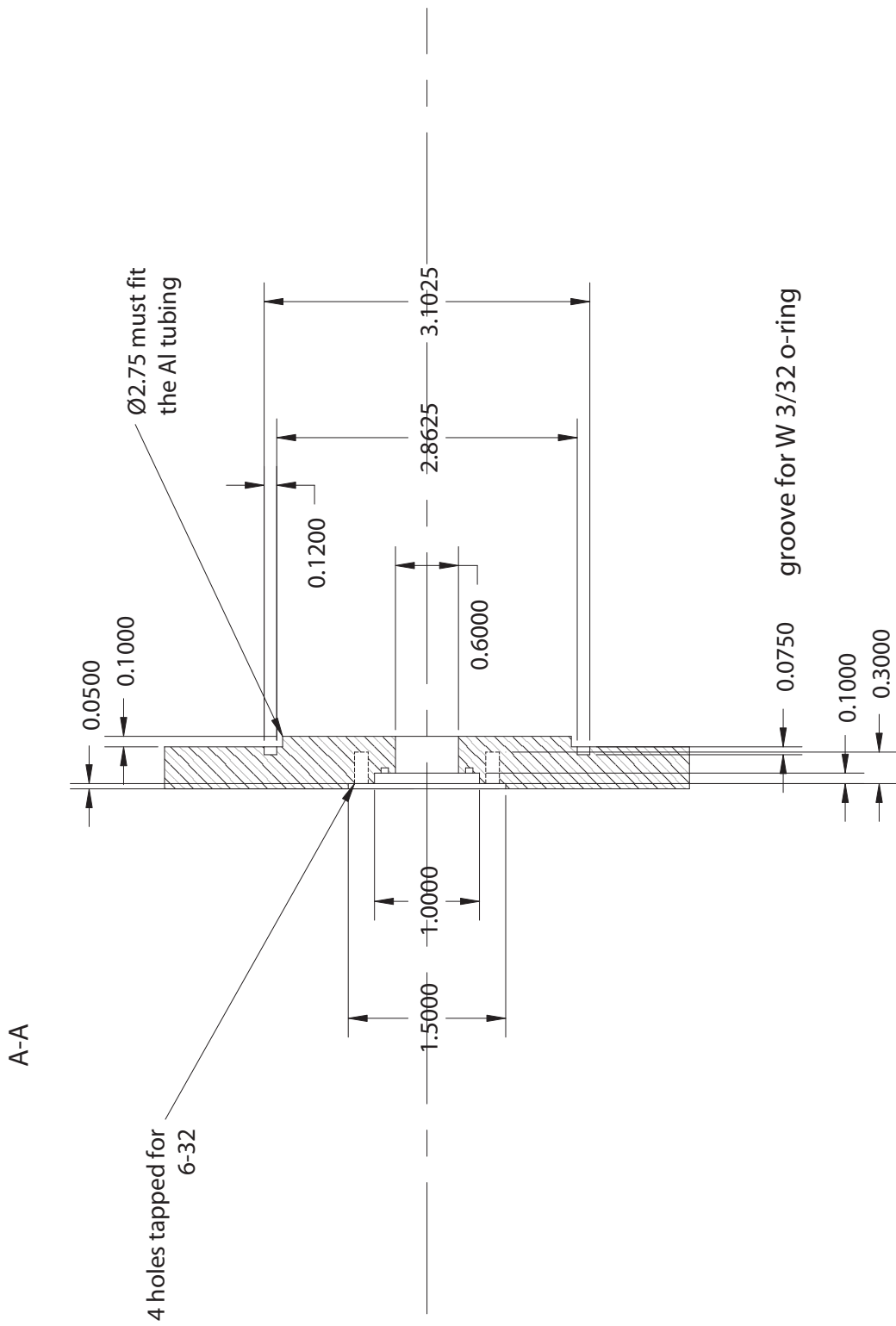


Figure 1.15: Drawing of the back flange of the cavity mirror mount - cross-sectional view A-A.

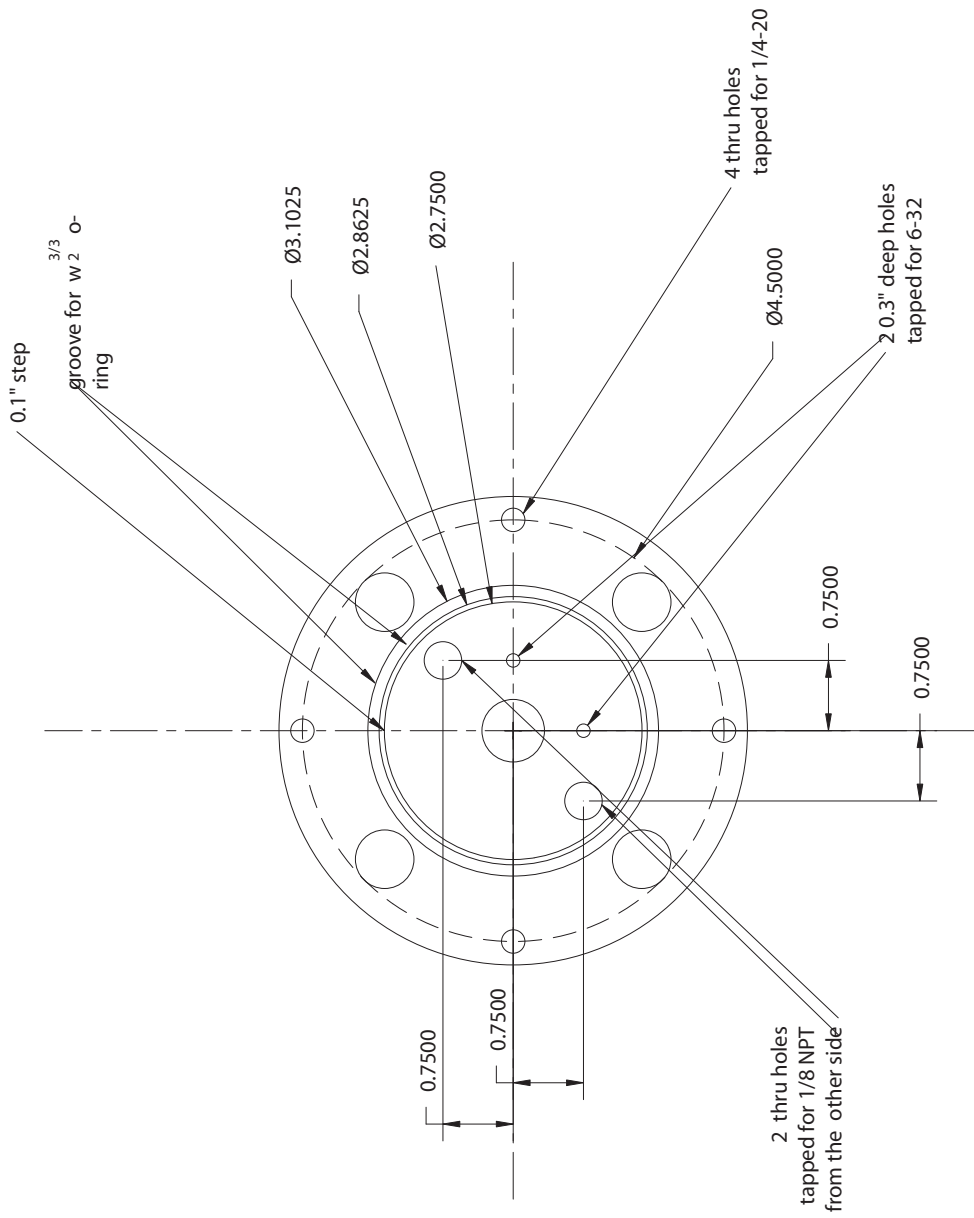


Figure 1.16: Drawing of the back flange of the cavity mirror mount - interior view.

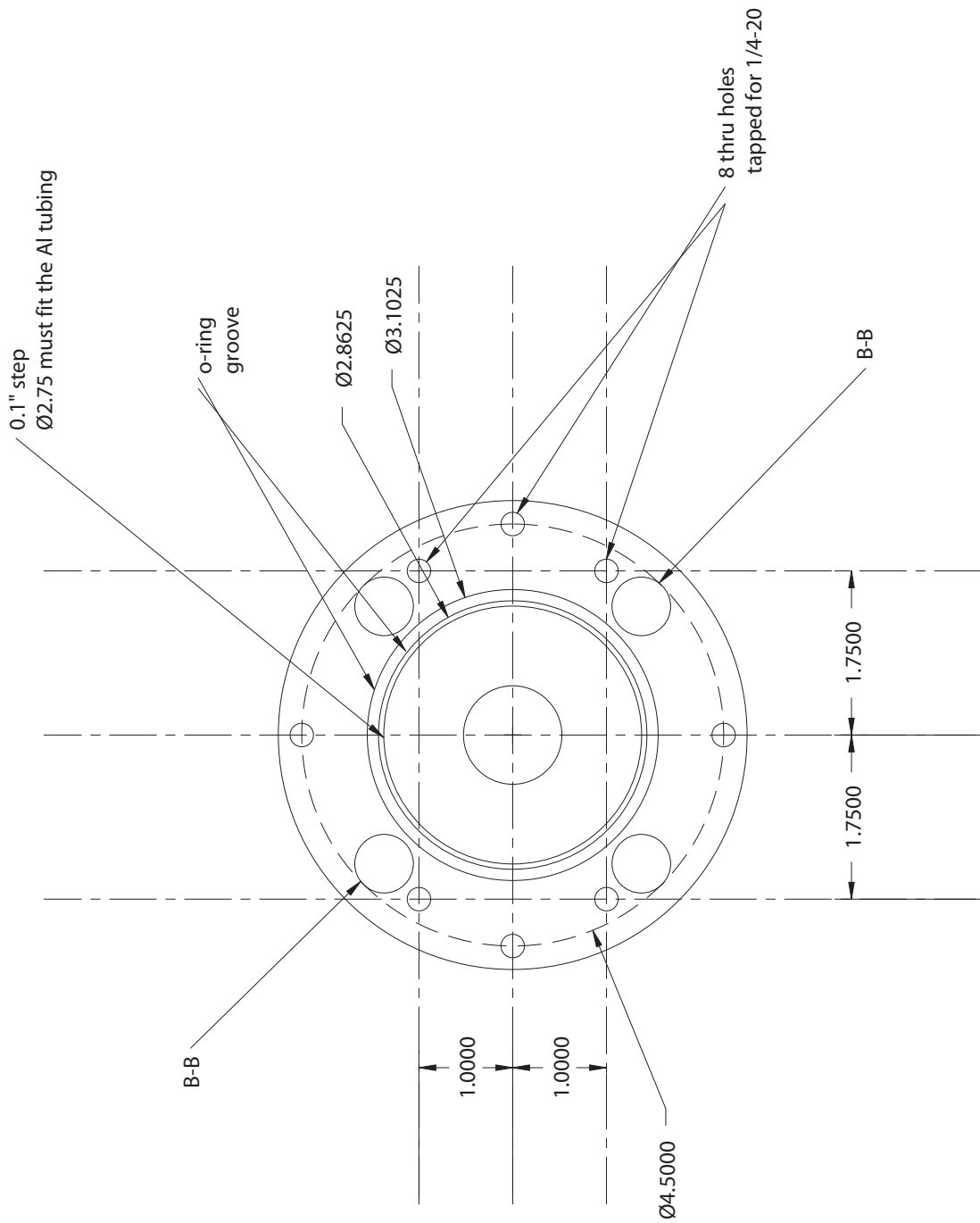


Figure 1.17: Drawing of the front flange of the cavity mirror mount - interior view.

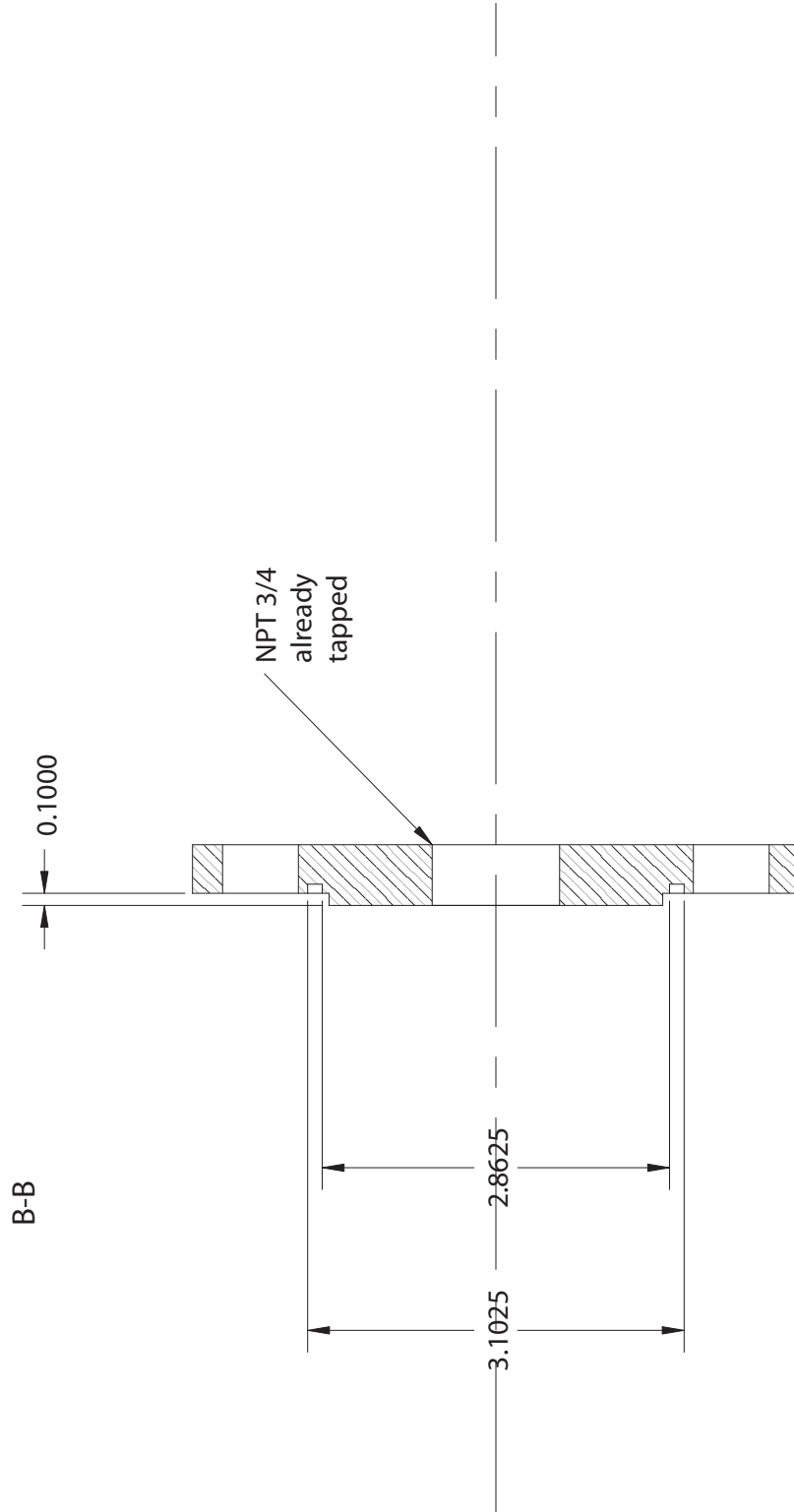


Figure 1.18: Drawing of the front flange of the cavity mirror mount - cross-sectional view B-B.

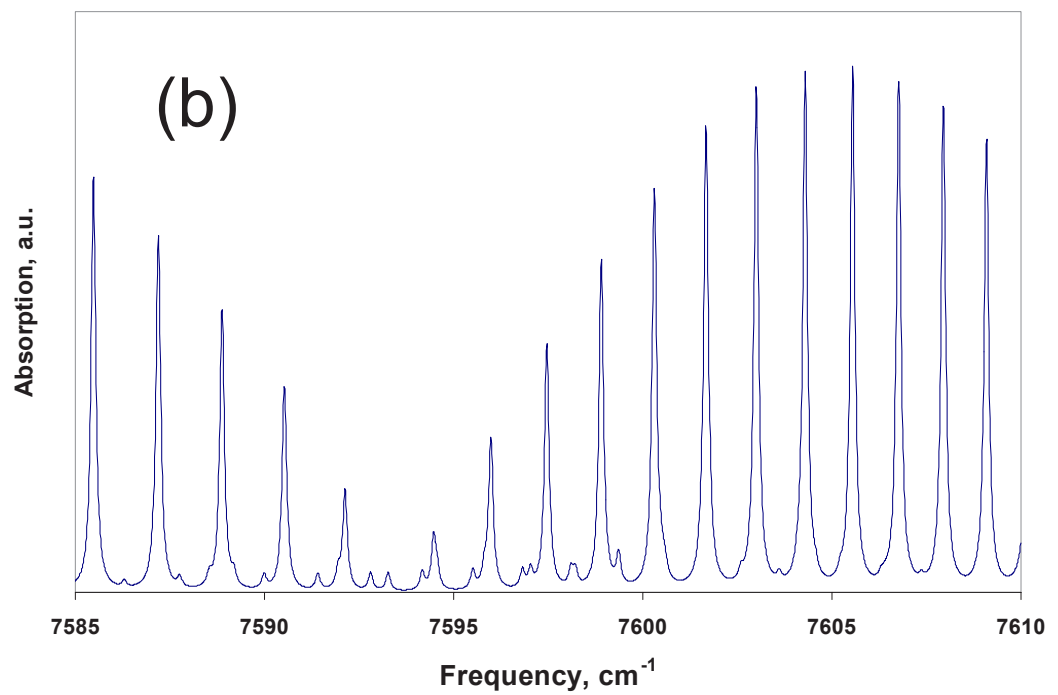
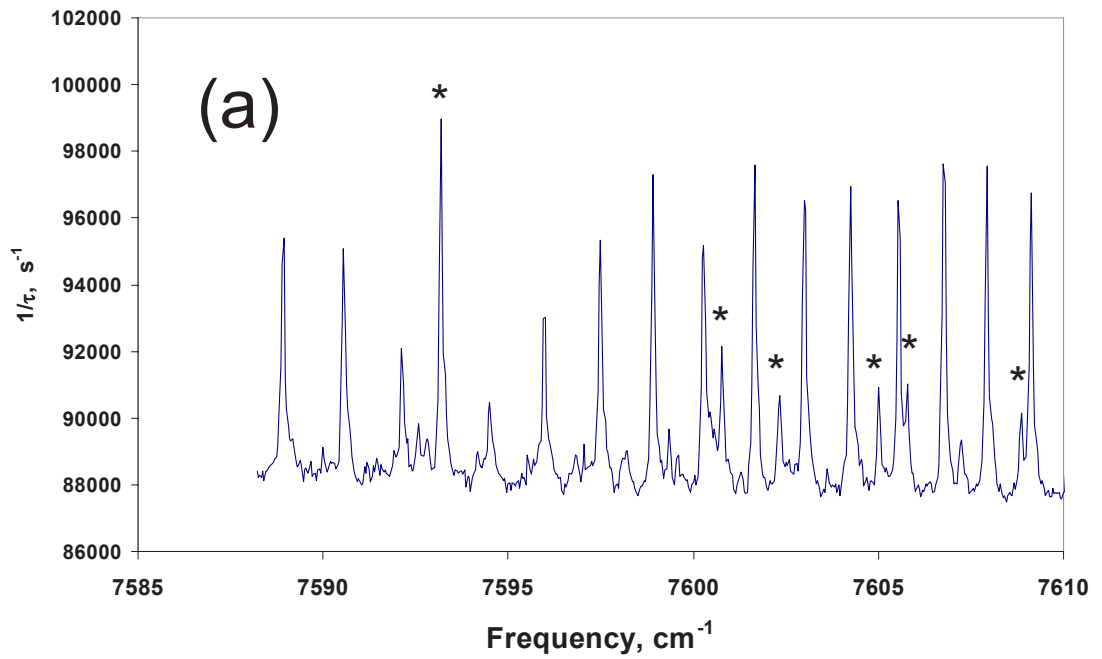


Figure 1.19: (a) Cavity ringdown spectrum of CO₂ at 10 Torr. (*) denotes water lines. (b) Simulated spectrum of CO₂ at 0.15 cm^{-1} resolution. Data taken from HITRAN database.

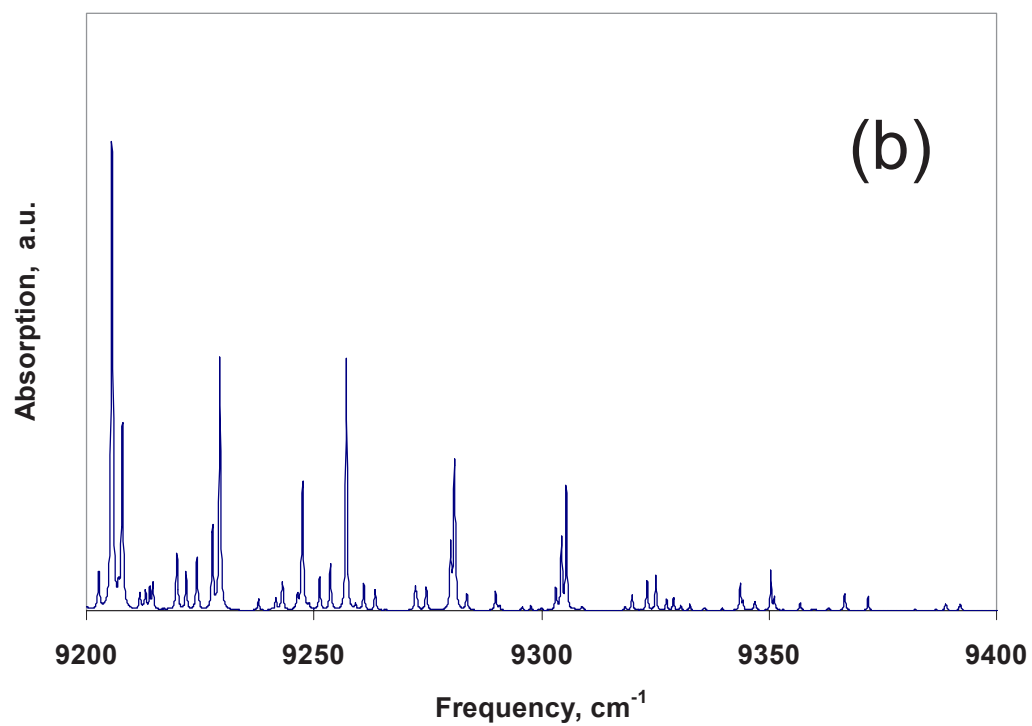
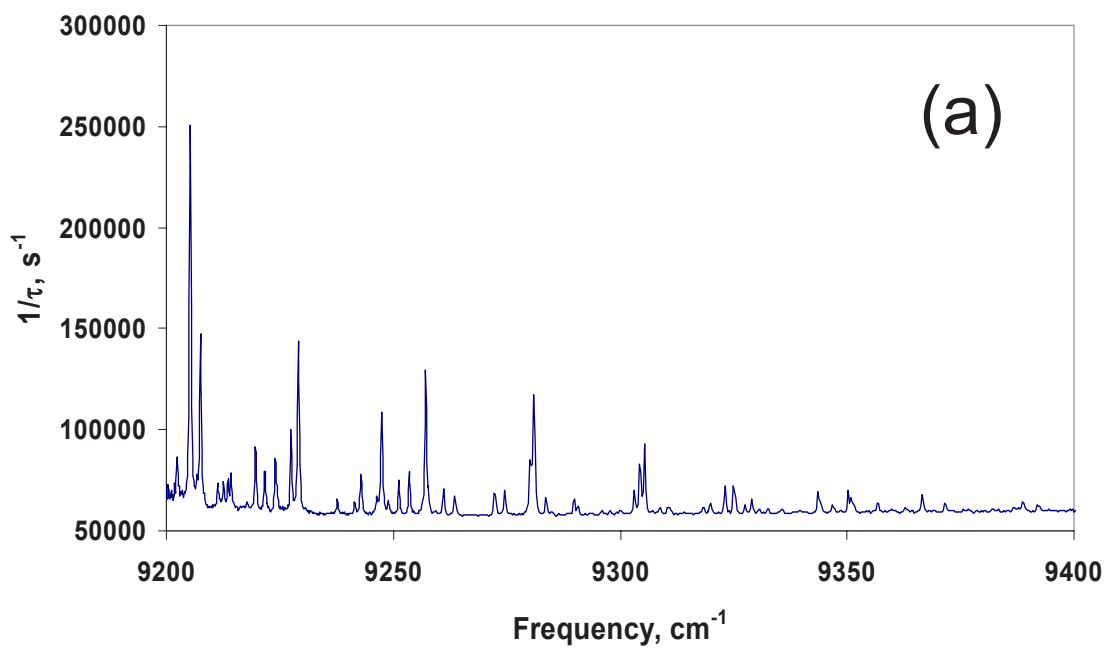


Figure 1.20: (a) Cavity ringdown spectrum of air at atmospheric pressure and humidity. (b) Simulated spectrum of 20 Torr of H_2O in 1 atm of air at 0.15 cm^{-1} resolution. Data taken from HITRAN database.

Chapter 2

Near infrared spectroscopy of chloro-peroxy radicals

2.1 Introduction

Peroxy radicals are important intermediates of oxidation of hydrocarbons in atmospheric chemistry and in combustion. They are formed by the addition of molecular oxygen to alkyl and alkenyl radicals, and subsequently react with NO, NO₂, HO₂ and themselves eventually form ozone a major source of smog in urban areas. Oxidation of alkanes through hydrogen abstraction produces the simplest organic peroxy radicals: CH₃O₂, C₂H₅O₂. Reactions of alkenes and dienes with Cl and OH radicals at atmospheric conditions occur through the addition of the radicals to the double bonds; resulting in the formation of chloro- and hydroxy-peroxy radicals. Since two thirds of hydrocarbons emitted into the atmosphere come from the biosphere in the form of unsaturated compounds such as isoprene, substituted peroxy radicals play a major role in hydrocarbon atmospheric chemistry.

This chapter presents results of the first spectroscopic study of the near-infrared $\tilde{A} \leftarrow \tilde{X}$ electronic transition in several peroxy radicals formed in Cl atom-initiated

oxidation of the simplest alkenes and dienes. Chlorine oxidation is not generally dominant in the lower troposphere because the average concentration of Cl atoms is three orders of magnitude lower than the concentration of OH radicals, which is one of the other major oxidants. However, it has been shown recently [1] that at dawn in the marine boundary layer (MBL), the concentration of chlorine atoms can reach 10^5 atoms/cm⁻¹. Since the reaction rate of chlorine atoms with alkenes is an order of magnitude higher, MBL chlorine atoms in the morning become a significant source of peroxy radicals. Chlorine chemistry also dictates the removal of hydrocarbons in the Arctic MBL during ozone depletion events (polar spring), the frequency of which appears to increase.

Until recently, spectroscopic detection of peroxy radicals in kinetics experiments was solely done in the UV by probing the strong $\tilde{B} \leftarrow \tilde{X}$ electronic transition. This transition gives rise to broad unstructured bands in the 200-260 nm region with a typical half-width of 40 nm. Although the positions of the UV bands slightly change as a function of radical size and composition, the $\tilde{B} \leftarrow \tilde{X}$ bands of different radicals largely overlap, making it difficult to use UV detection to study reactions when more than one peroxy radical is present. In contrast, the first electronic state of peroxy radicals has relatively narrow bands with resolved vibrational and in some cases, rotational structure [2, 3]. The $\tilde{A} \leftarrow \tilde{X}$ bands of the small, most important peroxy radicals do not overlap, making it possible to monitor different radicals independently. Since large dienes (e.g., isoprene) have four radical addition sites, their oxidation can proceed through eight different pathways, forming structurally different peroxy

radicals. Measuring the branching ratio isoprene oxidation still remains one of the major problems of atmospheric chemistry. There have been numerous experimental studies of isoprene oxidation. However, in none of them were the intermediates of the process detected. The $\tilde{A} \leftarrow \tilde{X}$ transition of the intermediate peroxy radicals can potentially be used to study kinetics and measure the branching ratio of isoprene oxidation.

Although the first spectra of the $\tilde{A} \leftarrow \tilde{X}$ transition in the simplest peroxy radicals were reported almost thirty years ago, this transition has not been used by the kineticists until recently because of its low oscillator strength. The advent of cavity ringdown spectroscopy technique has greatly improved the sensitivity of direct absorption spectroscopy. Miller group has shown recently that CRDS can be successfully employed for spectroscopic studies of this transition [2]. The goal of this work was to obtain the $\tilde{A} \leftarrow \tilde{X}$ spectra chloro-peroxy radicals formed in oxidation of a number of alkenes, and to determine whether this transition could be used for the detection of substituted peroxy radicals in laboratory studies and in the atmosphere.

The mechanism of the reaction of chlorine atoms with small alkenes and dienes has been studied under various temperature and pressure conditions by several groups [4]. In general, there are two possible reaction mechanisms: 1) Cl atom addition to a double bond; and 2) alkyl hydrogen atom abstraction. Cl addition with subsequent HCl elimination will give the same products as allyl hydrogen abstraction. At normal atmospheric conditions Cl atom addition is the dominant mechanism [4, 5]. In molecules with a small number of internal degrees of freedom, Cl atom addition to a

double bond is a reversible process, and a third body is required to carry away the excess energy and stabilize the radical. Thus, the addition reaction has a positive pressure dependence, and at low enough pressures, its rate becomes slower than the rate of hydrogen atom abstraction. In $\text{Cl} + \text{C}_3\text{H}_8$ reaction, it occurs at the pressure of about 10 Torr [5]. Since the goal of the present work was to study chloro-peroxy radicals, the experiments were performed at the pressures at which the addition was the dominant process and chloro-peroxy radicals were the dominant intermediates.

2.2 Background

The $\tilde{\text{A}} \leftarrow \tilde{\text{X}}$ transitions in peroxy radicals involve excitation of a p-electron from a non-bonding to a slightly anti-bonding p-orbital on the tail oxygen atom. Thus, the transition would be sensitive only to electron density changes in the vicinity of the peroxy group. In HO_2 , the transition origin is located at 7029 cm^{-1} . Its position shifts to the blue in methyl and ethyl peroxy radicals. However, starting with ethyl peroxy a further increase of the carbon chain length changes only the width of the band, but not its position. The frequency of the 0-0 bands of methyl, ethyl and propyl radical were reported to be at 7383 cm^{-1} , 7593 cm^{-1} and 7564 cm^{-1} , respectively [6, 2]. All spectra of the $\tilde{\text{A}} \leftarrow \tilde{\text{X}}$ transition of peroxy radicals reported so far exhibited O-O stretching progressions with frequencies between 870 cm^{-1} and 930 cm^{-1} [3, 7, 6]. There is very little experimental data available on the effects of different ligands on the $\tilde{\text{A}} \leftarrow \tilde{\text{X}}$ transition. Recent work by Zalyubovsky *et al.* [7] on spectroscopy of CF_3O_2 showed that fluorine ligands shifted the band by 1000 cm^{-1} to the red. We

expected that a single chlorine ligand would have a similar effect on the transition, but to a lesser extent.

$\text{C}_2\text{H}_5\text{O}_2$ is the largest alkyl-peroxy radical for which a near-IR spectrum has been reported; thus, it will serve as a reference system for the analysis of our data. However, there are still some unanswered questions about the structure of $\text{C}_2\text{H}_5\text{O}_2$ and the assignment of its spectrum. *Ab initio* calculations performed by the Schaefer group predicted two stable structures for the radical [8, 9]. One of them (trans) has the O-O group in the CCO plane (C_s symmetry), whereas the group is almost perpendicular to that plane in the other one (gauche). At the CCSD(T)/TZ2P level, the gauche conformer is lower in energy by only 0.2 kcal mol⁻¹. The energies of the transition states between the stable geometries are 1.2 kcal mol⁻¹, which means that conversion can easily occur at room temperature. In the first reported near-IR spectrum of $\text{C}_2\text{H}_5\text{O}_2$, five strong bands were observed between 7000 and 9000 cm⁻¹ [6]. Based on the results of ¹⁸O isotopic substitution of oxygen, Hunziker and Wendt assigned only two bands (7593 and 8511 cm⁻¹) to the $\tilde{A} \leftarrow \tilde{X}$ transition of ethyl peroxy radical, $v'_{\text{O-O}} = 0$ and 1. The other observed bands were not assigned. Zalyubovsky *et al.* [7] observed the 7350 and 7590 cm⁻¹ bands in the cavity ringdown spectrum and attributed the former band, in part, to methyl peroxy radical although they could not explain the origin of methyl peroxy radicals in their experiment. It remains unclear whether the observed spectral features belong to both conformers or to a single conformer, and to which one.

2.3 Experiment

The peroxy radicals were produced in the quartz flow cell described in the previous chapter by pulsed laser photolysis. A diagram of the apparatus is shown in Fig. 1.11. DCM, Rhodamine 640 and Rhodamine 610 laser dyes and their mixtures were used to cover the 590-660 nm region ($6950\text{-}8600\text{ cm}^{-1}$). Two sets of ringdown mirrors were used in this experiment: Newport 1 m-ROC 1" diameter Ultra-Low Loss SuperMirrorsTM ($7000\text{-}8000\text{ cm}^{-1}$) and 6 m-ROC 0.8" diameter Los Gatos Research mirrors ($8000\text{-}8600\text{ cm}^{-1}$). During the experiment, a constant flow of nitrogen protected the mirrors from the reagents. The radiation exiting the cavity was tightly focused onto a 1 mm diameter extended-InGaAs photodiode (Hamamatsu). The photodiode signal was amplified by a factor of 50 and then digitized by the Compuscope 1012 board. Typically, 20 ringdown traces were averaged before fitting the signal to a single-exponential decay function.

Reagents were mixed before entering the flow cell. Molecular chlorine was photolyzed in the cell by 308 nm UV radiation of a XeCl excimer laser (Lambda Physik EMG 103). UV radiation was sent through the photolysis region of the cell, perpendicular to the gas flow. The beam was focused behind the cell by a cylindrical lens and had a rectangular 0.5×4.5 cm cross-section in the middle of the cell. The UV pulse energy entering the cell was 35 mJ. Both the excimer and dye lasers were operated at 19 Hz. Background absorption was measured and subtracted from the acquired spectrum to remove the absorption features of the alkene precursors and residual water, which have strong overtone transitions in the $7000\text{-}8600\text{ cm}^{-1}$ region. Both spectra

were acquired simultaneously; this allowed us to take into account possible changes of reflectivity of the mirrors (due to contamination of the surface, for example). At each laser wavelength during the scan, 20 waveforms were acquired, each following a photolysis pulse. Then, the excimer laser was turned off and 20 more waveforms were collected. Since the repetition rate of the our experiment (19 Hz) was faster than the residence time of the gas in the cell, the products of the reactions initiated by photolysis of chlorine accumulated in the cell. However, it was possible to identify the absorption features of the products in the spectrum by their time dependence. The concentration of peroxy radicals decreases rapidly after the photolysis, whereas the concentration of the products stays the same, on average.

Chloro-alkyl and alkenyl peroxy radicals were produced in the flow cell after the photolysis pulse via the following mechanism



Ethylene, propene, 2-butene (mixture of cis- and trans-) and 1,3-butadiene were used as hydrocarbon precursors. The typical pressures of the reactants in our experiments were $[\text{Cl}_2]=2$, $[\text{Alkene}]=0.5-1$, $[\text{O}_2]=20$ and $[\text{N}_2]=15$ Torr. We estimate that approximately 0.4% of Cl_2 molecules were photolyzed by each UV pulse. Total flow rate through the cell was 40 sccm. Thus, the cell was flushed after every 6 pulses.

A spectrum of unsubstituted ethyl peroxy radicals in the 7000-8200 cm^{-1} region was measured to test our instrument and to aid in the assignment of spectra of substituted radicals. The radical was produced via $\text{Cl}_2/\text{C}_2\text{H}_6/\text{O}_2$ chemistry and its spectrum was acquired under the same conditions as the spectra of the chlorinated species.

Since the rate constants of the chemical reactions leading to formation and destruction of $\text{C}_2\text{H}_4\text{ClO}_2$ are known, we simulated the time dependence of its concentration under the conditions of our experiment. The concentration of the peroxy radical was predicted to reach a maximum 15 μs after the photolysis pulse. According to our simulations, its concentration would decrease by only 3% over the next 10 μs the typical ringdown time in our experiment. Thus, the ringdown signal should stay exponential with good accuracy. All ringdown spectra were acquired 15 μs after the photolysis pulse. Additional scans with 4 ms delay were also performed to identify spectral features that belonged to transient species.

2.4 Results and Discussion

We revisited the spectrum $\text{C}_2\text{H}_5\text{O}_2$ using an alternative method of generating radicals to those employed in previous studies. The spectrum in the 7200-8200 cm^{-1} region is shown in Fig. 2.1. In the 7300-7700 cm^{-1} region, our spectrum resembles the one reported by Zalyubovsky *et al.* [7], but in this case, the 7350 cm^{-1} band did not exhibit a sharp Q-branch characteristic to CH_3O_2 spectrum. A study of the dependence of the spectral features on the delay between the photolysis and the IR laser pulses showed that both bands decayed at the same rate (within the error of the

fit). However, because the rates of CH_3O_2 reactions with itself and with $\text{C}_2\text{H}_5\text{O}_2$ are the same, the presence of methyl peroxy radical would lead to equal disappearance rates of CH_3O_2 and $\text{C}_2\text{H}_5\text{O}_2$. Thus, we can neither rule out CH_3O_2 based on the kinetics data, nor explain its possible presence in our system. In addition, we observed two more bands at 8050 and 8510 cm^{-1} . Due to strong absorption of C_2H_6 precursor at 8500 cm^{-1} , we were not able to obtain a clean spectrum of the 8510 cm^{-1} band.

Because we expected the $\tilde{\text{A}} \leftarrow \tilde{\text{X}}$ transition of chloro-peroxy radicals to be shifted to the red from the origin of the $\text{C}_2\text{H}_5\text{O}_2$ band, we initially searched the 7000-7600 cm^{-1} region. For each radical, we observed a strong band between 7300 and 7400 cm^{-1} . Since all near-IR spectra of peroxy radicals exhibit O-O stretching bands, we extended the scans in the regions 900 cm^{-1} to the red and to the blue from the observed bands. No absorption was detected in the 6400-6700 cm^{-1} region, whereas in the 8100-8600 cm^{-1} , region we observed several bands for every radical we investigated. This indicates that the 7400 cm^{-1} bands were the origin bands of the $\tilde{\text{A}} \leftarrow \tilde{\text{X}}$ transition in the chloro-peroxy radicals. The obtained cavity ringdown spectra of chloro-ethyl, 2-chloro-propyl, 2-chloro-3-butyl and chloro-butenyl peroxy radicals are shown in Fig. 2.2-2.5. No absorption bands of the chloro-peroxy radicals were observed between 7900 and 8100 cm^{-1} and for this reason, the scans in that region are omitted. Strong absorption of 2-butene in the 8100-8600 cm^{-1} region did not allow us to acquire a clean spectrum of $\text{C}_4\text{H}_8\text{ClO}_2$.

The chloro-peroxy radicals studied in this work exhibited more complex spectra than CH_3O_2 and $\text{C}_2\text{H}_5\text{O}_2$. They do demonstrate features common to all peroxy

radicals: a strong origin band and the presence of the O-O stretch bands. However, all the chloro-peroxy species have several other bands between the 0-0 band and the O-O stretch, in addition to several new bands in the O-O stretch region. None of the bands in the spectra has a resolved rotational structure. The bands significantly broaden and their peak intensity decreases in the spectra of the larger radicals. Another common feature of all chloro-peroxy radicals is the presence of absorption bands at 7800 cm^{-1} , approximately 450 cm^{-1} to the blue from the origin bands. We should notice that the 8047 cm^{-1} band of ethyl peroxy has the same spacing from its origin.

In $\text{C}_2\text{H}_4\text{ClO}_2$, the origin band is centered at 7355 cm^{-1} and has distinct asymmetric shoulders about 65 cm^{-1} from the center, with the red one being more extended. Besides the origin band, six other bands are observed in the $7200\text{-}8600\text{ cm}^{-1}$ region: three of them within 500 cm^{-1} from the origin, and the other three in the region of the O-O stretch. All other bands are almost symmetric with the width of $40\text{-}45\text{ cm}^{-1}$ at half maximum. The origin is the strongest band in the spectrum its intensity at least twice as strong as the intensities of the other bands. The second strongest band is located at 8232 cm^{-1} , it being the first band in the O-O stretch region. There are no obvious similarities between the spectrum patterns in the $7300\text{-}7700$ and $8200\text{-}8600\text{ cm}^{-1}$ regions.

In the $\text{C}_3\text{H}_6\text{ClO}_2$ spectrum, most of the features have irregular shapes most likely resulting from the overlapping of several bands. The origin is located at 7390 cm^{-1} and has about the same width (40 cm^{-1}) as in $\text{C}_2\text{H}_4\text{ClO}_2$. The 0-0 band of chloropropyl peroxy radical also has two distinct shoulders at 7292 and 7364 cm^{-1} which

are spaced farther from the main band. The 7600 cm^{-1} satellite is a 80 cm^{-1} wide feature with three peaks, most likely comprised of several bands. The intensity of the 7800 cm^{-1} band in $\text{C}_3\text{H}_6\text{ClO}_2$ is much smaller than in $\text{C}_2\text{H}_4\text{ClO}_2$. This band was barely detectable in our experiment, so we could not resolve its structure. In the O-O stretch region, the $\text{C}_3\text{H}_6\text{ClO}_2$ and $\text{C}_2\text{H}_4\text{ClO}_2$ spectra are significantly different. In chloro-propyl peroxy, the strongest band is in the middle of the region and its shape resembles the shape of the origin. The $8200\text{-}8600\text{ cm}^{-1}$ region mirrors the origin of the transition, the only difference being the absence of any structure in the 8500 cm^{-1} band.

The $\text{C}_4\text{H}_8\text{ClO}_2$ and $\text{C}_4\text{H}_6\text{ClO}_2$ spectra (Fig. 2.4 and 2.5) have very broad ($100\text{-}150\text{ cm}^{-1}$) overlapping unstructured features. In the $7400\text{-}7600\text{ cm}^{-1}$ region, three $\text{C}_4\text{H}_8\text{ClO}_2$ and two $\text{C}_4\text{H}_6\text{ClO}_2$ bands are observed. The 7800 cm^{-1} feature also appears in the $\text{C}_4\text{H}_8\text{ClO}_2$ spectrum and is stronger than in $\text{C}_3\text{H}_6\text{ClO}_2$.

We performed several *ab initio* calculations using Gaussian 98 package [10] to aid in assigning the observed spectroscopic features. The geometries of the chloro-ethyl and chloro-propyl radicals were optimized and their vibrational frequencies were calculated using B3LYP/6-311++G(2df,2p) method. Single point energies of $\text{C}_2\text{H}_4\text{ClO}_2$ were then calculated at the CCSD/6-311++G(2df,2p) level of theory.

Four stable conformers of $\text{C}_2\text{H}_4\text{ClO}_2$ were found. We labeled them as trans-trans, trans-gauche, gauche (a), and gauche (b) (see Fig. 2.6 and 2.7). For the trans-trans conformer the only one that belongs to C_s symmetry group the energy and the frequencies of the first excited state were also calculated. The results are summarized

in Tables 2.1, 2.2 and 2.3. Franck-Condon factors for the $\tilde{A} \leftarrow \tilde{X}$ transition of the trans-trans conformer were computed using FCFGAUS program [11, 12]. The predicted stick spectrum for this conformer is shown in Fig. 2.2. The energies of all four conformers of $C_2H_4ClO_2$ fall within a 1 kcal mol^{-1} interval which is actually smaller than the error of the CCSD/6-311++G(2df,2p) method [13]. The energy differences between the gauche and trans conformers (0.4 and $0.8 \text{ kcal mol}^{-1}$, respectively) are larger than the corresponding difference for ethyl peroxy radicals. The barriers between the trans and gauche conformers are less than $1.6 \text{ kcal mol}^{-1}$. We also searched for stable geometries of $C_3H_6ClO_2$ at the B3LYP/6-311++G(2df,2p) level. There are nine possible structures of the chloro-peroxy radical formed in oxidation of propene. The Cl atom can substitute one of the three hydrogen atom in the methyl group and the O-O bond can have three stable positions between each pair of the three hydrogen atoms surrounding it. We labeled these structures Ia, Ib, Ic, IIa, IIb, IIc, IIIa, IIIb and IIIc (see Fig. 2.9, 2.9 and 2.9). Only Ic geometry was not stable, probably due to steric repulsion between the tail oxygen and the chlorine atom. Eight of these geometries were found to be stable, six of which had energies within 1 kcal mol^{-1} (see Table 2.5) and therefore might have been observed in our experiment. Since the number of possible conformers, as well as the number of basis functions needed to describe the system increases fast for the larger radicals, we did not perform calculation for $C_4H_8ClO_2$ and $C_4H_6ClO_2$.

The possible existence of multiple conformers of the peroxy radicals makes unambiguous assignment of their spectra difficult. Because we lack reliable theoretical

predictions for the energy of the \tilde{A} state for all conformers, we cannot completely rule out the possibility that the observed spectral features belong to different conformers of the radicals. In order to gain some insight about $C_2H_4ClO_2$, we revisited a simpler system: $C_2H_5O_2$. The authors of the two previous experimental reports on ethyl peroxy radicals [6, 2] only assigned the origin and the O-O stretching band, but did not address the issue of multiple conformers. If the theoretical prediction of Rienstra-Kiracofe *et al.* [9] is correct and both conformers of $C_2H_5O_2$ have almost the same energy, one should expect to see two progressions in the spectra. There are indeed three unassigned bands in the spectrum reported by Hunziker and Wendt. The 8050 cm^{-1} band is located 450 cm^{-1} to the blue from the origin, at the same interval as the 7800 cm^{-1} bands present in the spectra of $C_2H_4ClO_2$, $C_3H_6ClO_2$ and $C_4H_8ClO_2$. Therefore, these bands belong to the same mode pertinent to O_2 group. The closest mode predicted to be active in trans-trans $C_2H_5O_2$ and $C_2H_4ClO_2$ is the COO bending vibration. The origin of the other two unassigned bands in the ethyl peroxy spectrum remains unclear. However, none of them can be the 0-0 band of the other conformer, due to the absence of the second O-O and COO progressions in the spectrum. Since the difference in predicted vibrational frequencies for the O-O and COO vibrations of the conformers in the ground state is smaller than 20 cm^{-1} , it is also possible that the 0-0 transition and the vibronic bands of the conformers largely overlap. The same conclusion can be drawn from the $C_3H_6ClO_2$ spectrum. Although we did not measure the concentration of the peroxy radicals directly in our experiment, they should be approximately the same because they are proportional to

the initial concentration of chlorine atoms. As seen in Fig. 2.2, the origin bands of $C_2H_4ClO_2$ and $C_3H_6ClO_2$ have comparable width and intensity. This indicates that multiple conformers of $C_3H_6ClO_2$ contribute to the 0-0 band, and the energy of the transition is independent of the molecular geometry (within 40 cm^{-1}).

Making the same assumption, for $C_2H_4ClO_2$, we attempted to assign the additional features in the spectrum to vibronic bands. The simulated vibronic spectrum of the trans-trans conformer predicted the band pattern in the $7300\text{-}7800\text{ cm}^{-1}$ region reasonably well. Thus, the 7527 and 7602 cm^{-1} bands correspond to the backbone bend (ν_3) and the O-O wag ($2\nu_1$). The shoulders of the origin band probably belong to a low frequency vibration. Both the O-O wag and the CH_2Cl twist have the frequencies around 100 cm^{-1} . Because the $\tilde{A} \leftarrow \tilde{X}$ transition mostly affects the O-O group, only vibrations involving the oxygen atoms should have non-zero Franck-Condon factors and therefore, the CH_2Cl twist should not be active. Due to symmetry constraints, the fundamental ν_1 vibration does not appear in the simulated spectrum of the trans-trans conformer. However, it should be active in the other conformers. Thus, we can assign the origin shoulder bands to the fundamental and a hot band of the ν_1 vibration. In the $8200\text{-}8600\text{ cm}^{-1}$ region, the only qualitative discrepancies between the theory and the experiment is the presence of the CO vibration and the absence of $\nu_{12}+\nu_1$ mode (symmetry constraint). The strongest band in this region is obviously the O-O stretch ν_{12} ; the other three bands can be assigned to its combination modes: $\nu_{12}+\nu_1$, $\nu_{12}+2\nu_1$ (or $\nu_{12}+\nu_3$).

The same vibrations should be active in the spectra of the other chloro-peroxy

radicals. As seen from Tables 2.2, 2.3, 2.5 and 2.6, the vibrational frequencies of different conformers vary significantly. Thus, as the number of conformers increase, the vibronic bands in the spectra will broaden. The number of low-frequency backbone bending modes also increases in the larger radicals. Excitation of these modes analogous to $C_2H_4ClO_2$ probably gives rise to the broad bands in the $7600-7700\text{cm}^{-1}$ region in the spectrum of $C_4H_8ClO_2$. These considerations can explain the observed trends in the spectra of the peroxy radicals.

In the case of 1,3-butadiene, two structural isomers, 1-chloro 2-butenyl 4-peroxy and 1-chloro 3-butenyl 2-peroxy are produced in chlorine-initiated oxidation with the ratio of 55%/40% [14]. This fact most likely determines the structure of the spectrum. When the peroxy group is in 4 position, it does not interact with the chlorine ligand and the transition in that isomer remains unperturbed, producing the 7600 and 8500 cm^{-1} bands in the $C_3H_6ClO_2$ spectrum. When it is in 2 position, the interaction with the Cl ligand shifts the bands by 200 cm^{-1} to the red.

Cavity ringdown spectroscopy can also be employed for kinetics studies on the time scale longer than the ringdown time. The observed rate of absorption decay is dependent on both the reaction rate and the reagent concentrations. Assuming that the major mechanism of peroxy radical removal in our experiment is their self-reaction, $1/[RO_2]$ should have a linear dependence on time:

$$\frac{[RO_2]_0}{[RO_2]} = 1 + 2k[RO_2]_0t. \quad (2.4)$$

Fitting the experimental $1/[RO_2](t)$ to a linear function (Fig. 2.12) yields the

product $2k[\text{RO}_2]_0$. For $\text{C}_2\text{H}_4\text{ClO}_2$, the rate of self-reaction has been experimentally measured [15, 16]. Therefore, it is possible to obtain $[\text{RO}_2]_0$ and estimate the absorption cross-section for the transition. We measured the absorption of $\text{C}_2\text{H}_4\text{ClO}_2$ at 7353 cm^{-1} the peak of the 0-0 band as a function of delay between the photolysis and IR pulses in the $10\text{ }\mu\text{s}$ -4 ms interval. Using $k = 4.5 \times 10^{-12}\text{ cm}^3\text{s}^{-1}$ rate constant (Chakir *et al.*), we obtained the value of $S = \int_{7200}^{8600} \sigma(\nu)d\nu = 5.8 \times 10^{-18}\text{ cm}^{-1}/(\text{molecule}\cdot\text{cm}^{-2})$ for the integrated absorption cross-section of the transition. We observed weak constant "absorption" everywhere in the 7000 - 8600 cm^{-1} region, partially due to light scattering on the acoustic wave and aerosol particles formed in the cell after pulsed photolysis. We were not able to quantify these effects. Excluding the baseline from the integral would yield a smaller cross-section value $S = 2.8 \times 10^{-18}\text{ cm}^{-1}/(\text{molecule}\cdot\text{cm}^{-2})$.

2.5 Conclusion

In this chapter, the first spectra of the electronic $\tilde{\text{A}} \leftarrow \tilde{\text{X}}$ transition in $\text{C}_2\text{H}_4\text{ClO}_2$, $\text{C}_3\text{H}_6\text{ClO}_2$, $\text{C}_4\text{H}_8\text{ClO}_2$ and $\text{C}_4\text{H}_6\text{ClO}_2$ radicals were reported. The origin bands of the radicals were observed at around 7400 cm^{-1} , thus shifted by 200 cm^{-1} to the red from their position in unsubstituted homologues. The O-O stretching and the COO bending modes were active in all radicals. Several bands non-present in the spectra of unsubstituted radicals were observed around the 0-0 and the O-O stretch bands. *Ab initio* calculations predicted four and eight structural conformers of $\text{C}_2\text{H}_4\text{ClO}_2$ and $\text{C}_3\text{H}_6\text{ClO}_2$, respectively. Although we could not unambiguously assign all observed

spectral features, we demonstrated that they could correspond to vibronic transitions.

The energy of the $\tilde{A} \leftarrow \tilde{X}$ transition was found to be sensitive only to the immediate environment of the peroxy group, and not to the increase of the aliphatic chain further than two carbon atoms. In addition, the larger peroxy radicals demonstrated broad, unstructured, overlapping bands. Both observations lead us to the conclusion that the $\tilde{A} \leftarrow \tilde{X}$ transition will not provide significant information about the structures of the prevalent large peroxy radicals, e.g., as those formed in terpene oxidation. However, this transition could still be used for selective monitoring in kinetic studies.

References

- [1] C. W. Spicer, E. G. Chapman, B. J. Finlayson-Pitts, R. A. Plastridge, J. M. Hubbe, J. D. Fast, and C. M. Berkowitz. *Nature*, 394(6691):353–356, 1998.
- [2] M. B. Pushkarsky, S. J. Zalyubovsky, and T. A. Miller. *Journal of Chemical Physics*, 112(24):10695–10698, 2000.
- [3] S. J. Zalyubovsky, B. G. Glover, and T. A. Miller. *Journal of Physical Chemistry A*, 107(39):7704–7712, 2003.
- [4] M. J. Ezell, W. H. Wang, A. A. Ezell, G. Soskin, and B. J. Finlayson-Pitts. *Physical Chemistry Chemical Physics*, 4(23):5813–5820, 2002.
- [5] E. W. Kaiser and T. J. Wallington. *Journal of Physical Chemistry*, 100(48):18770–18774, 1996.
- [6] H. E. Hunziker and H. R. Wendt. *Journal of Chemical Physics*, 64(8):3488–90, 1976.
- [7] S. J. Zalyubovsky, D. B. Wang, and T. A. Miller. *Chemical Physics Letters*, 335(3-4):298–304, 2001.

- [8] Igor S. Ignatyev, Yaoming Xie, Wesley D. Allen, and III Schaefer, Henry F. *Journal of Chemical Physics*, 107(1):141–155, 1997.
- [9] Jonathan C. Rienstra-Kiracofe, Wesley D. Allen, and III Schaefer, Henry F. *Journal of Physical Chemistry A*, 104(44):9823–9840, 2000.
- [10] M. J. Frisch, G. W. Trucks, H. B. Schlegel, G. E. Scuseria, M. A. Robb, J. R. Cheeseman, V. G. Zakrzewski, J. A. Montgomery, Jr., R. E. Stratmann, J. C. Burant, S. Dapprich, J. M. Millam, A. D. Daniels, K. N. Kudin, M. C. Strain, O. Farkas, J. Tomasi, V. Barone, M. Cossi, R. Cammi, B. Mennucci, C. Pomelli, C. Adamo, S. Clifford, J. Ochterski, G. A. Petersson, P. Y. Ayala, Q. Cui, K. Morokuma, D. K. Malick, A. D. Rabuck, K. Raghavachari, J. B. Foresman, J. Cioslowski, J. V. Ortiz, A. G. Baboul, B. B. Stefanov, G. Liu, A. Liashenko, P. Piskorz, I. Komaromi, R. Gomperts, R. L. Martin, D. J. Fox, T. Keith, M. A. Al-Laham, C. Y. Peng, A. Nanayakkara, M. Challacombe, P. M. W. Gill, B. Johnson, W. Chen, M. W. Wong, J. L. Andres, C. Gonzalez, M. Head-Gordon, E. S. Replogle, and J. A. Pople. *Gaussian 98, Revision A.9*. Gaussian, Inc., Pittsburgh PA, 1998.
- [11] P. Chen. *In Unimolecular and Bimolecular Reactions Dynamics*. John Wiley & Sons, Chichester, 1994.
- [12] K. M. Ervin, T. M. Ramond, G. E. Davico, R. L. Schwartz, S. M. Casey, and W. C. Lineberger. *Journal of Physical Chemistry A*, 105(48):10822–10831, 2001.

- [13] W. Klopper, K. L. Bak, P. Jorgensen, J. Olsen, and T. Helgaker. *Journal of Physics B-Atomic Molecular and Optical Physics*, 32(13):R103–R130, 1999.
- [14] W. H. Wang and B. J. Finlayson-Pitts. *Journal of Geophysical Research-Atmospheres*, 106(D5):4939–4958, 2001.
- [15] T. J. Wallington, J. M. Andino, and S. M. Japar. *Chemical Physics Letters*, 165(2-3):189–194, 1990.
- [16] A. Chakir, J. Brion, J. P. Ganne, and D. Daumont. *Physical Chemistry Chemical Physics*, 5(12):2573–2580, 2003.

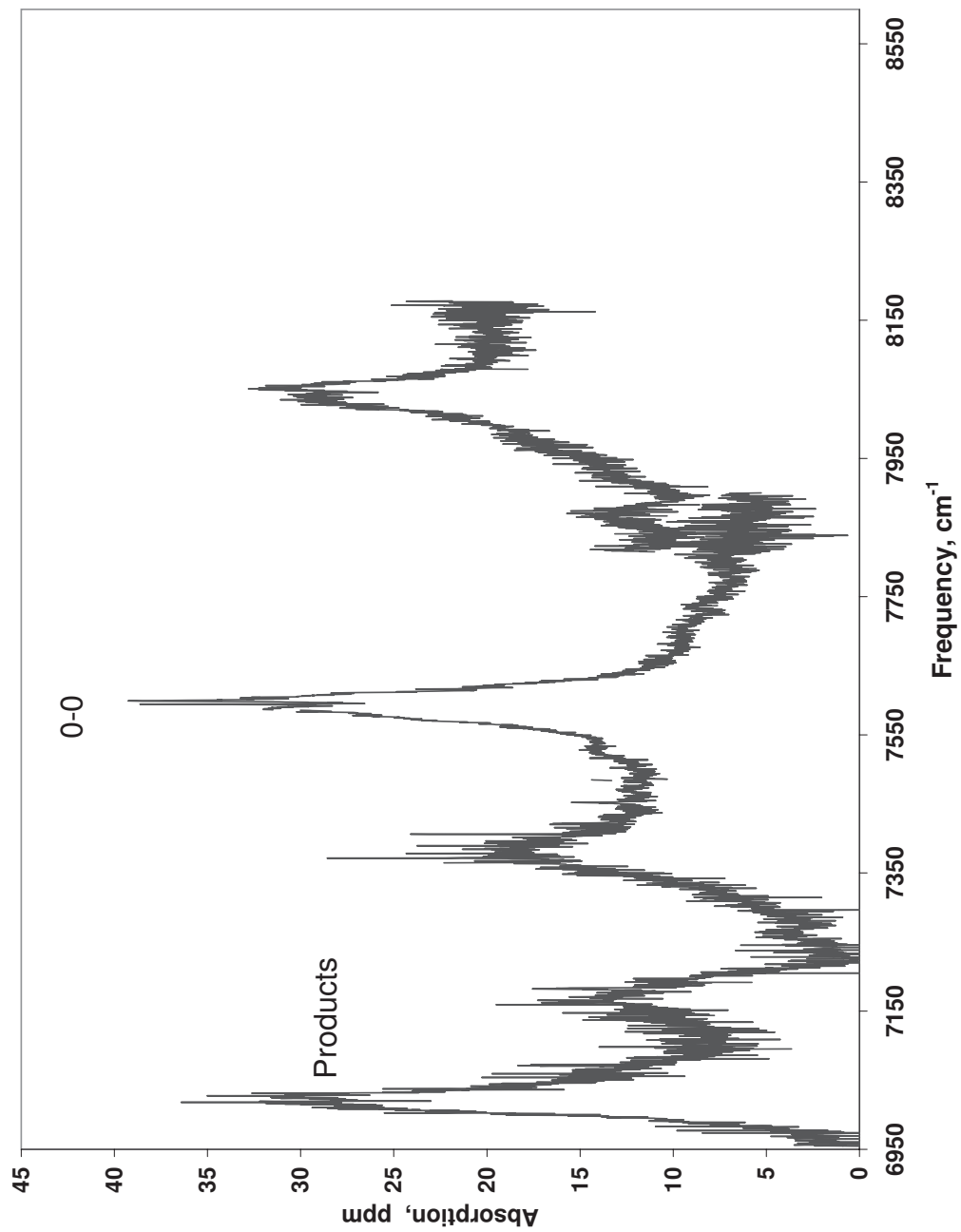


Figure 2.1: Cavity ringdown spectrum of $C_2H_5O_2$.

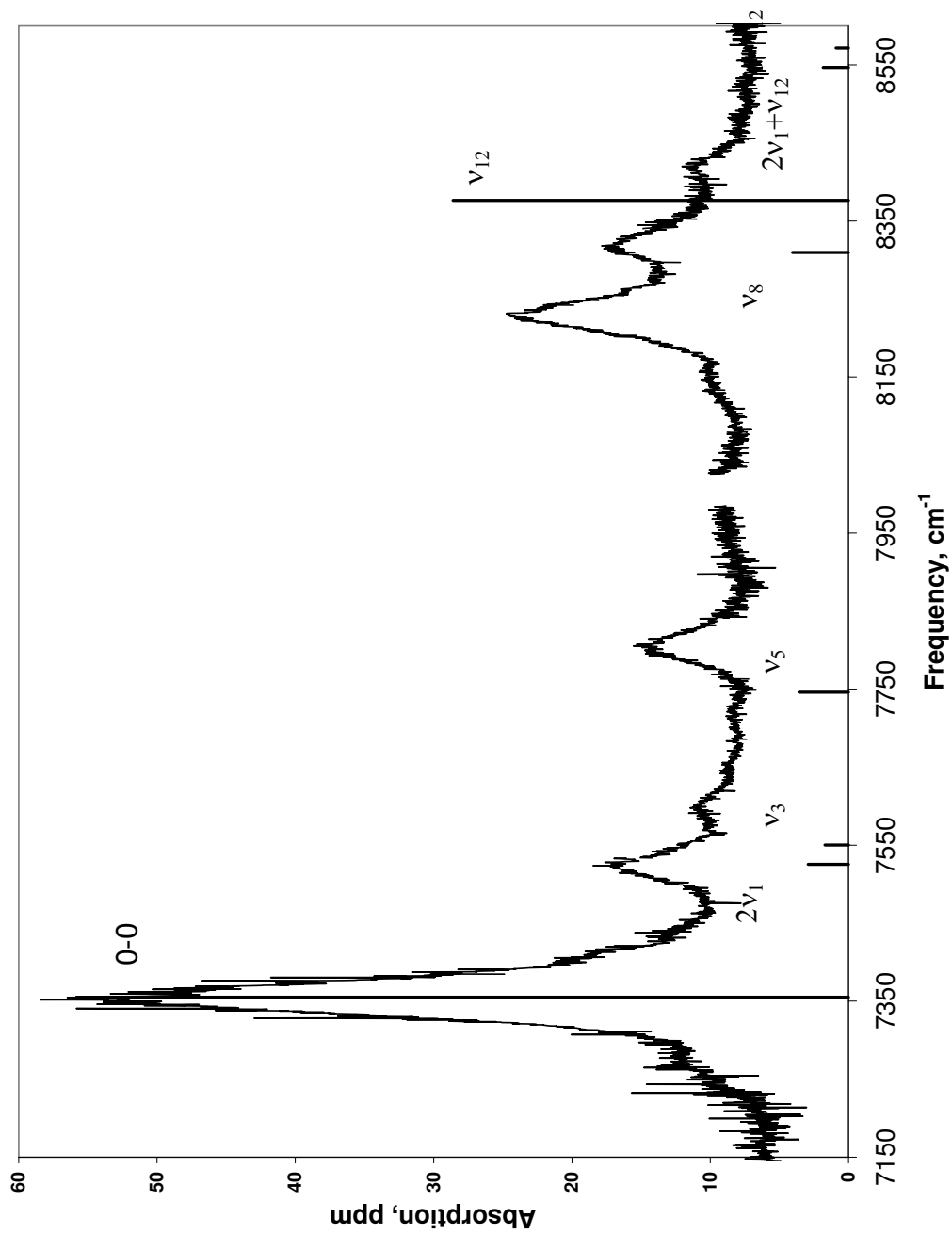


Figure 2.2: Cavity ringdown and simulated stick spectra of $C_2H_4ClO_2$. The geometries of the \tilde{X} and \tilde{A} states were optimized at the B3LYP/6-311++(2df,2p) level. The Franck-Condon were computed with FCFGAUS program.

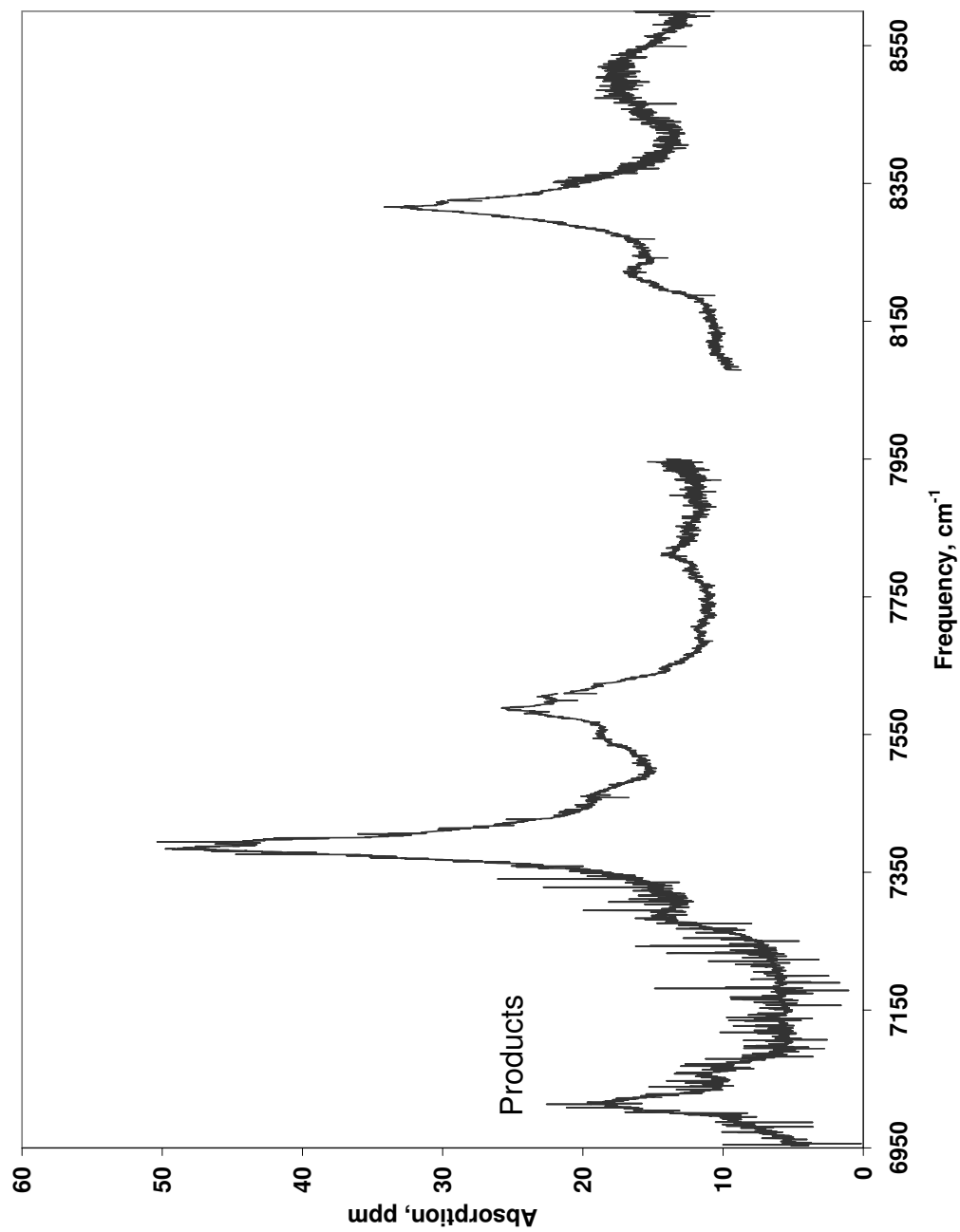


Figure 2.3: Cavity ringdown spectrum of $C_3H_6ClO_2$.

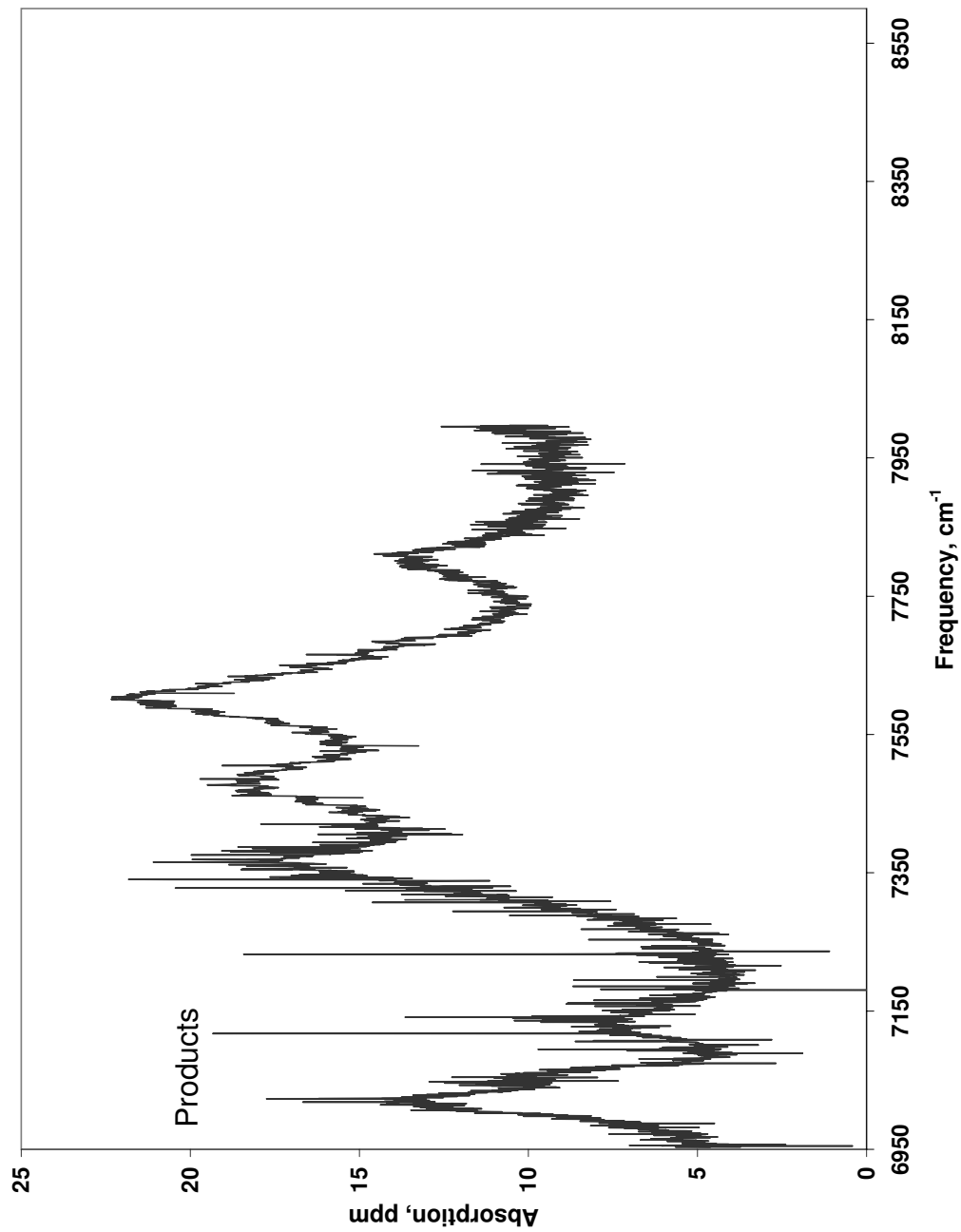


Figure 2.4: Cavity ringdown spectrum of $C_4H_8ClO_2$.

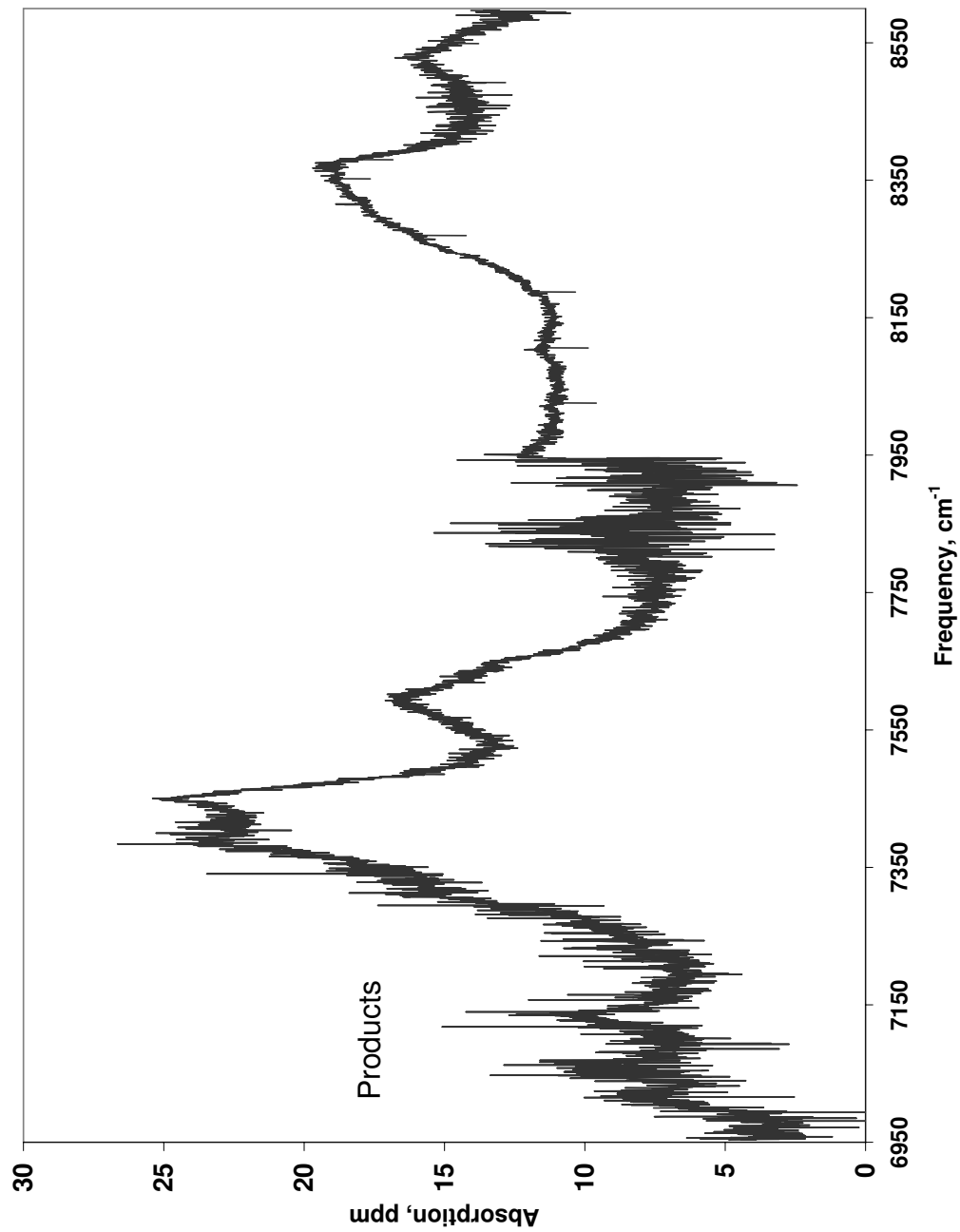


Figure 2.5: Cavity ringdown spectrum of $C_4H_6ClO_2$.

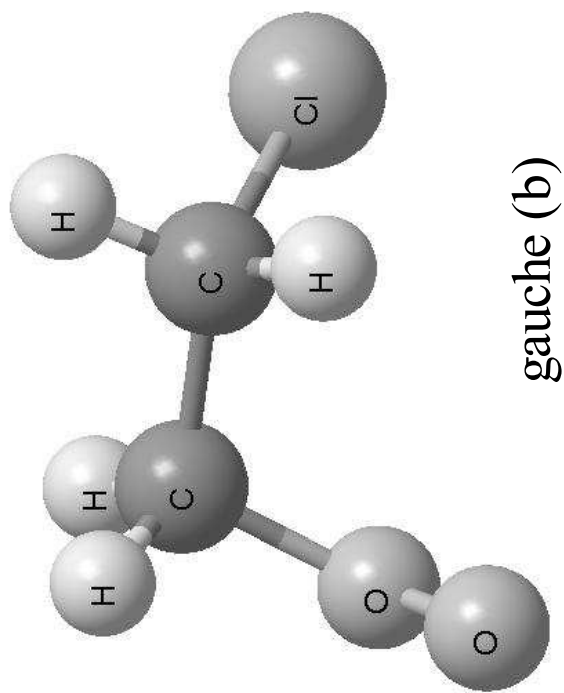
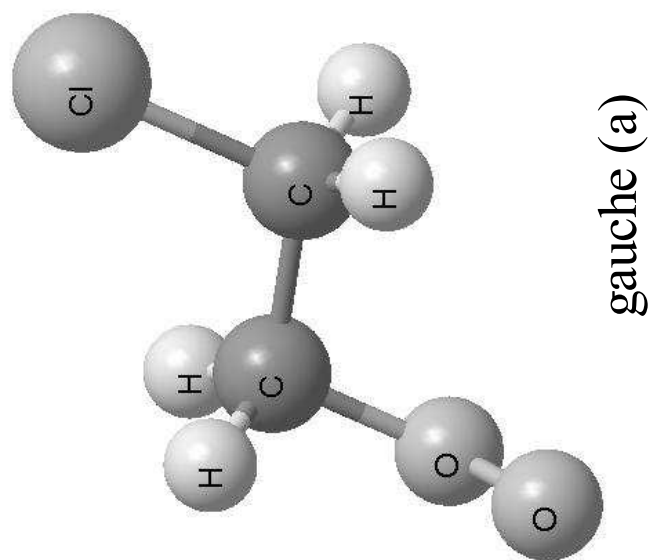
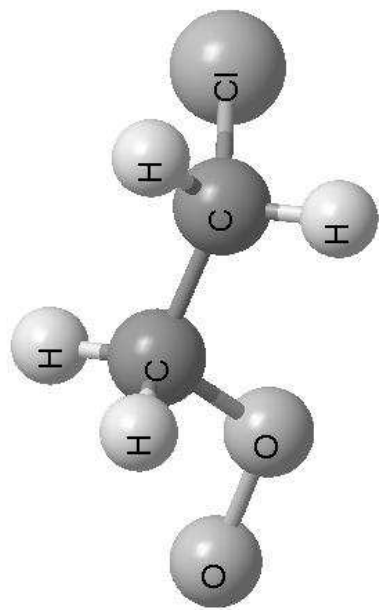
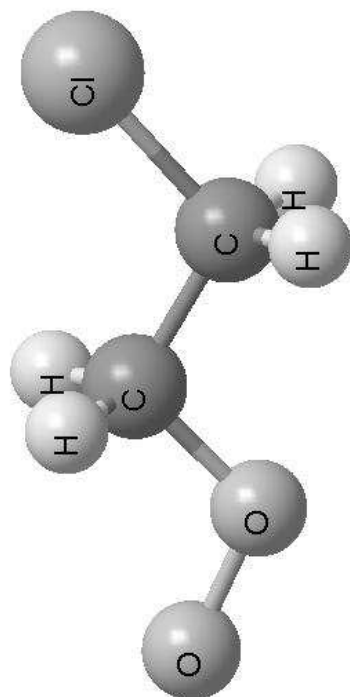


Figure 2.6: Geometries of the gauche conformers of $C_2H_4ClO_2$ optimized at the B3LYP/6-311++(2df,2p) level.

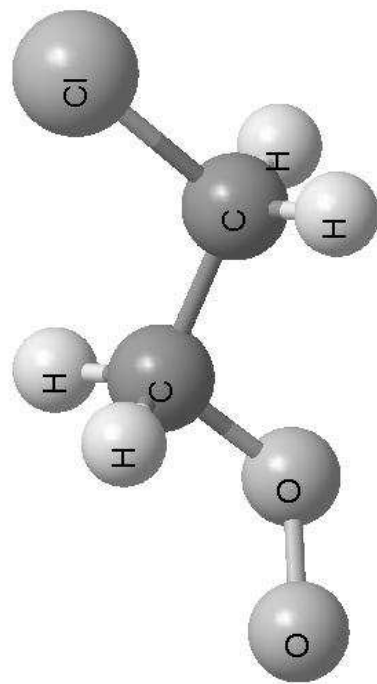


trans-gauche

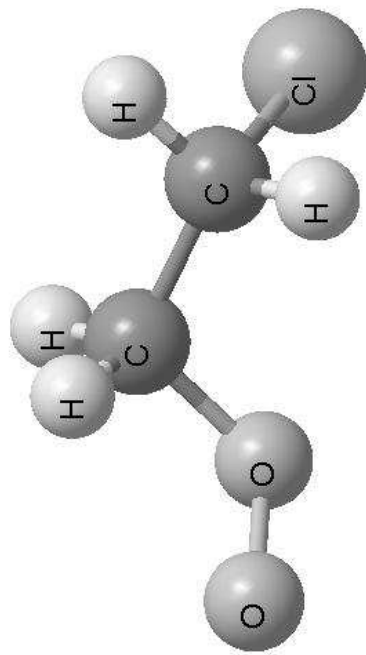


trans-trans

Figure 2.7: Geometries of the trans-trans and trans-gauche conformers of $C_2H_4ClO_2$ optimized at the B3LYP/6-311++(2df,2p) level.



TS-1



TS-2

Figure 2.8: Geometries of the transition states between the trans and the gauche conformers of $C_2H_4ClO_2$ optimized at the B3LYP/6-311++(2df,2p) level.

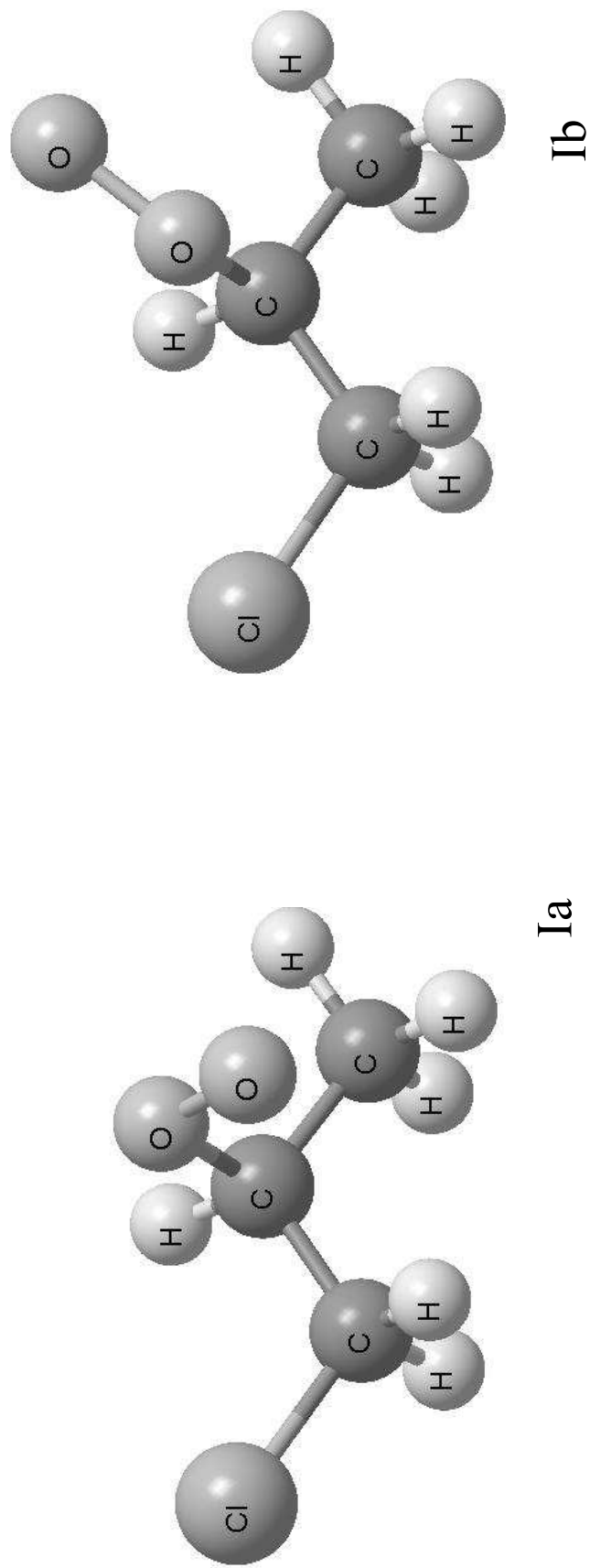


Figure 2.9: Geometries of C₃H₆ClO₂ optimized at the B3LYP/6-311++(2df,2p) level, Ia and Ib conformers.

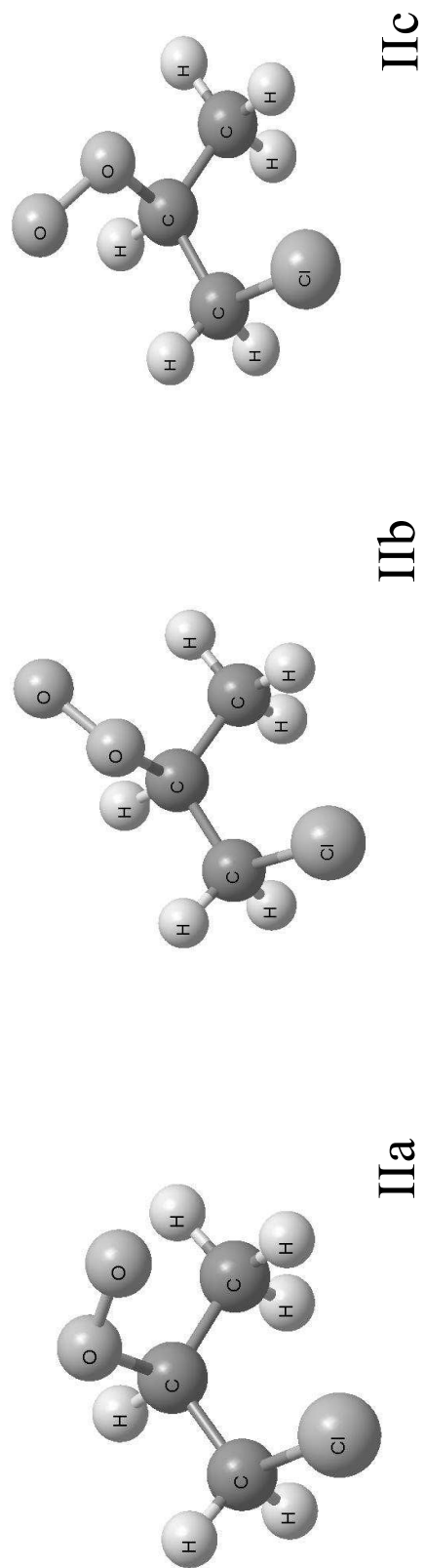


Figure 2.10: Geometries of $C_3H_6ClO_2$ optimized at the B3LYP/6-311++(2df,2p) level, IIa, IIb and IIc conformers.

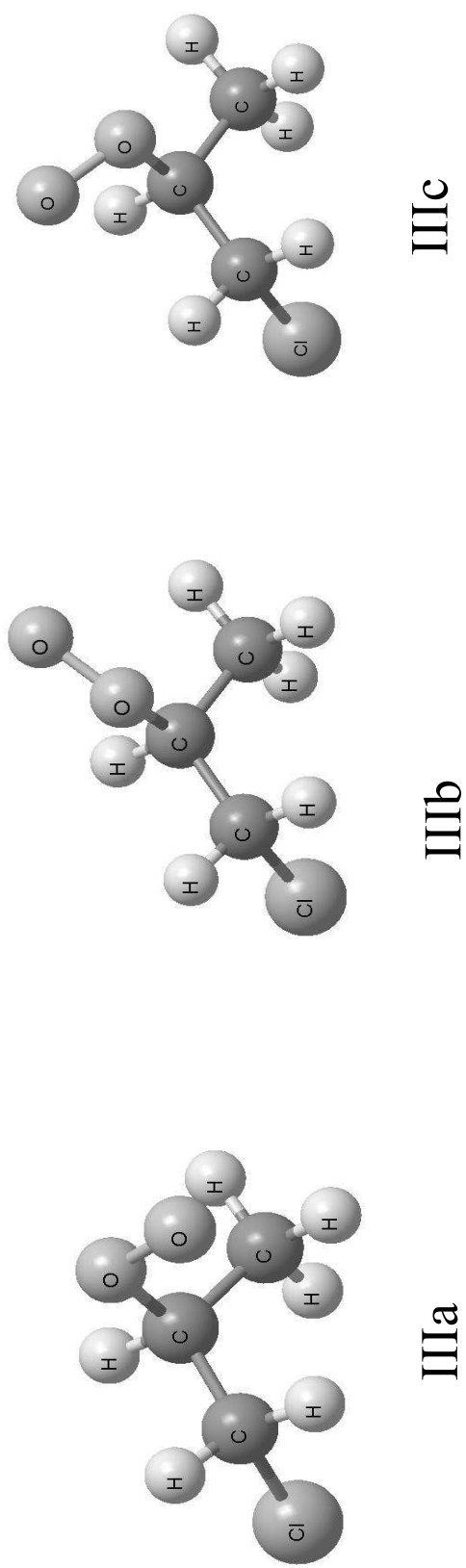


Figure 2.11: Geometries of $C_3H_6ClO_2$ optimized at the B3LYP/6-311++(2df,2p) level, IIIa, IIIb and IIIc conformers.

Table 2.1: Relative energies of chloro-ethyl peroxy radical conformers and transition states between them calculated with 6-311++G(2df,2p) basis set. Zero point energies were calculated at B3LYP level.

conformer	B3LYP	B3LYP incl. ZPE	CCSD	CCSD incl. ZPE
gauche (a)	0.00	0.00	0.00	0.00
trans-trans-TS	1.02		1.32	
trans-trans \tilde{X} A''	0.76	0.59	0.92	0.75
trans-trans \tilde{A} A'	22.12	21.65	20.75	20.28
gauche (b)	0.24	0.19	0.27	0.22
trans-gauche-TS	1.45		1.85	
trans-gauche	0.69	0.52	0.83	0.66

Table 2.2: Frequencies of the gauche conformers of $C_2H_4ClO_2$ at the B3LYP/6-311++G(2df,2p) level.

Mode	gauche (a)	gauche (b)	description
ν_1	94	74	OO wag
ν_2	105	142	CH ₂ Cl twist
ν_3	239	252	CiCCO backbone
ν_4	324	420	CCO bend
ν_5	533	543	COO bend
ν_6	759	667	CCl stretch
ν_7	794	809	CH ₂ rock
ν_8	903	951	CO stretch
ν_9	1049	970	CH ₂ rock&CH ₂ Cl twist
ν_{10}	1060	1081	CC stretch
ν_{11}	1155	1158	CH ₂ twist
ν_{12}	1234	1220	OO stretch
ν_{13}	1278	1270	CH ₂ twist & CH ₂ Cl twist
ν_{14}	1308	1326	CH ₂ twist
ν_{15}	1380	1387	CH ₂ wag

Continued on next page

Table 2.2 - continued from previous page

Mode	gauche	gauche	description
	(a)	(b)	
ν_{16}	1483	1470	CH ₂ Cl H scissors
ν_{17}	1499	1473	CH ₂ scissors
ν_{18}	3084	3062	CH ₂ sym. stretch
ν_{19}	3101	3094	CH ₂ Cl H sym. stretch
ν_{20}	3141	3131	CH ₂ asym. stretch
ν_{21}	3167	3154	CH ₂ Cl H asym. stretch

Table 2.3: Frequencies of the trans- conformers of $C_2H_4ClO_2$ in the \tilde{X} and \tilde{A} states at the B3LYP/6-311++G(2df,2p) level

Mode	trans-	trans-trans		description
	gauche	\tilde{X} A''	\tilde{A} A'	
ν_1	58	55	97	OO wag
ν_2	122	105	108	CH ₂ Cl twist
ν_3	263	176	171	ClCCO backbone
ν_4	350	330	339	CCO bend
ν_5	530	489	391	COO bend
ν_6	668	757	757	C-Cl stretch
ν_7	805	789	813	CH ₂ rock
ν_8	965	943	954	CO stretch
ν_9	1006	1042	1059	CH ₂ rock&CH ₂ Cl twist
ν_{10}	1069	1083	1063	CC stretch
ν_{11}	1190	1180	1201	CH ₂ twist
ν_{12}	1210	1194	1021	OO stretch
ν_{13}	1252	1285	1284	CH ₂ twist & CH ₂ Cl twist
ν_{14}	1324	1290	1288	CH ₂ twist

Continued on next page

Table 2.3 - continued from previous page

Mode	trans-	trans-trans		description
	gauche	$\tilde{X} A''$	$\tilde{A} A'$	
ν_{15}	1390	1387	1391	CH ₂ wag
ν_{16}	1474	1497	1499	CH ₂ Cl H scissors
ν_{17}	1481	1504	1525	CH ₂ scissors
ν_{18}	3053	3075	3044	CH ₂ sym. stretch
ν_{19}	3092	3097	3092	CH ₂ Cl H sym. stretch
ν_{20}	3121	3129	3101	CH ₂ asym. stretch
ν_{21}	3148	3159	3163	CH ₂ Cl H asym. stretch

Table 2.4: Relative energies of chloro-propyl peroxy radical conformers at the B3LYP level with cc-pvtz and 6-311++G(2df,2p) basis sets with and without zero-point energy (ZPE) corrections.

Conformer	cc-pvtz		6-311++g(2df,2p)	
	w/o ZPE	with ZPE	w/o ZPE	with ZPE
Ia	0.74	0.76	0.86	0.86
Ib	0.69	0.62	0.66	0.57
IIa	2.93	2.86	2.91	2.82
IIb	1.24	1.20	1.19	1.14
IIc	0.54	0.51	0.53	0.49
IIIa	0.68	0.71	0.76	0.80
IIIb	0.84	0.82	0.79	0.77
IIIc	0.00	0.00	0.00	0.00

Table 2.5: Frequencies of Ia and Ib conformers of $C_3H_6ClO_2$ at the B3LYP/6-311++(2df,2p) level.

Mode	Ia		Ib	
	cc-pvtz	6-311++G(2df,2p)	cc-pvtz	6-311++G(2df,2p)
ν_1	78	77	78	75
ν_2	144	141	107	106
ν_3	198	196	201	200
ν_4	218	218	226	224
ν_5	298	295	291	290
ν_6	340	339	348	349
ν_7	441	440	448	448
ν_8	593	595	535	534
ν_9	735	737	743	745
ν_{10}	779	779	782	782
ν_{11}	898	897	900	900
ν_{12}	920	919	923	923
ν_{13}	1033	1033	1050	1049
ν_{14}	1112	1112	1101	1100
ν_{15}	1133	1133	1136	1135

Continued on next page

Table 2.5 - continued from previous page

Mode	Ia		Ib	
	cc-pvtz	6-311++G(2df,2p)	cc-pvtz	6-311++G(2df,2p)
ν_{16}	1154	1161	1192	1200
ν_{17}	1231	1231	1237	1238
ν_{18}	1289	1290	1287	1288
ν_{19}	1358	1358	1348	1348
ν_{20}	1383	1384	1367	1367
ν_{21}	1411	1414	1409	1412
ν_{22}	1466	1468	1469	1472
ν_{23}	1488	1490	1488	1491
ν_{24}	1502	1504	1501	1503
ν_{25}	3046	3050	3041	3045
ν_{26}	3089	3091	3084	3086
ν_{27}	3096	3098	3091	3090
ν_{28}	3114	3118	3109	3112
ν_{29}	3124	3128	3125	3128
ν_{30}	3155	3156	3145	3148

Table 2.6: Frequencies of IIa, IIb and IIc conformers of $C_3H_6ClO_2$ at the B3LYP/6-311++(2df,2p) level.

Mode	IIa		IIb		IIc	
	cc-pvtz	6-311++	cc-pvtz	6-311++	cc-pvtz	6-311++
	G(2df,2p)		G(2df,2p)		G(2df,2p)	
ν_1	68	57	79	79	74	73
ν_2	89	90	97	96	128	126
ν_3	198	198	198	198	199	200
ν_4	219	221	228	227	207	207
ν_5	310	309	319	320	298	296
ν_6	357	354	336	336	346	346
ν_7	477	480	468	466	521	520
ν_8	619	619	590	591	557	558
ν_9	718	717	691	693	697	698
ν_{10}	769	769	808	808	804	804
ν_{11}	885	883	875	875	875	874
ν_{12}	909	908	924	924	911	910
ν_{13}	1024	1023	1048	1048	1033	1032
ν_{14}	1090	1089	1078	1078	1084	1084

Continued on next page

Table 2.6 - continued from previous page

Mode	IIa		IIb		IIc	
	cc-pvtz	6-311++	cc-pvtz	6-311++	cc-pvtz	6-311++
	G(2df,2p)		G(2df,2p)		G(2df,2p)	
ν_{15}	1142	1147	1148	1147	1163	1165
ν_{16}	1177	1181	1190	1199	1203	1209
ν_{17}	1229	1229	1238	1239	1224	1224
ν_{18}	1300	1299	1311	1312	1301	1300
ν_{19}	1358	1357	1339	1340	1340	1340
ν_{20}	1372	1372	1365	1363	1364	1363
ν_{21}	1416	1420	1410	1413	1420	1423
ν_{22}	1469	1472	1470	1473	1468	1470
ν_{23}	1485	1487	1489	1492	1488	1490
ν_{24}	1502	1503	1502	1504	1500	1502
ν_{25}	3038	3041	3042	3046	3045	3049
ν_{26}	3052	3056	3049	3053	3052	3056
ν_{27}	3085	3086	3091	3093	3092	3095
ν_{28}	3113	3117	3116	3119	3116	3120
ν_{29}	3140	3143	3136	3139	3133	3137
ν_{30}	3153	3154	3145	3148	3151	3154

Table 2.7: Frequencies of IIIa, IIIb and IIIc conformers of $C_3H_6ClO_2$ at the B3LYP/6-311++(2df,2p) level.

Mode	IIIa		IIIb		IIIc	
	cc-pvtz	6-311++	cc-pvtz	6-311++	cc-pvtz	6-311++
	G(2df,2p)		G(2df,2p)		G(2df,2p)	
ν_1	89	88	72	70	91	90
ν_2	104	104	99	98	112	109
ν_3	204	203	186	186	195	198
ν_4	220	222	224	186	218	219
ν_5	292	291	299	300	272	273
ν_6	358	357	341	341	374	374
ν_7	387	386	443	443	422	421
ν_8	601	602	524	524	533	533
ν_9	768	770	750	753	755	757
ν_{10}	793	794	834	834	820	821
ν_{11}	872	872	868	868	868	867
ν_{12}	919	919	914	915	911	911
ν_{13}	1048	1048	1063	1062	1060	1059
ν_{14}	1087	1088	1085	1086	1090	1090

Continued on next page

Table 2.7 - continued from previous page

Mode	IIa		IIb		IIc	
	cc-pvtz	6-311++	cc-pvtz	6-311++	cc-pvtz	6-311++
	G(2df,2p)		G(2df,2p)		G(2df,2p)	
ν_{15}	1140	1140	1147	1146	1149	1150
ν_{16}	1152	1159	1190	1199	1192	1199
ν_{17}	1241	1241	1238	1239	1234	1234
ν_{18}	1285	1287	1285	1286	1281	1282
ν_{19}	1365	1368	1344	1345	1339	1340
ν_{20}	1378	1377	1382	1380	1381	1379
ν_{21}	1409	1412	1411	1415	1419	1421
ν_{22}	1487	1489	1486	1489	1482	1484
ν_{23}	1491	1494	1493	1495	1492	1494
ν_{24}	1505	1507	1504	1506	1502	1504
ν_{25}	3051	3055	3045	3048	3046	3050
ν_{26}	3083	3086	3083	3085	3083	3086
ν_{27}	3098	3100	3092	3093	3093	3095
ν_{28}	3122	3126	3117	3120	3116	3120
ν_{29}	3128	3131	3129	3131	3128	3131
ν_{30}	3160	3163	3151	3153	3157	3159

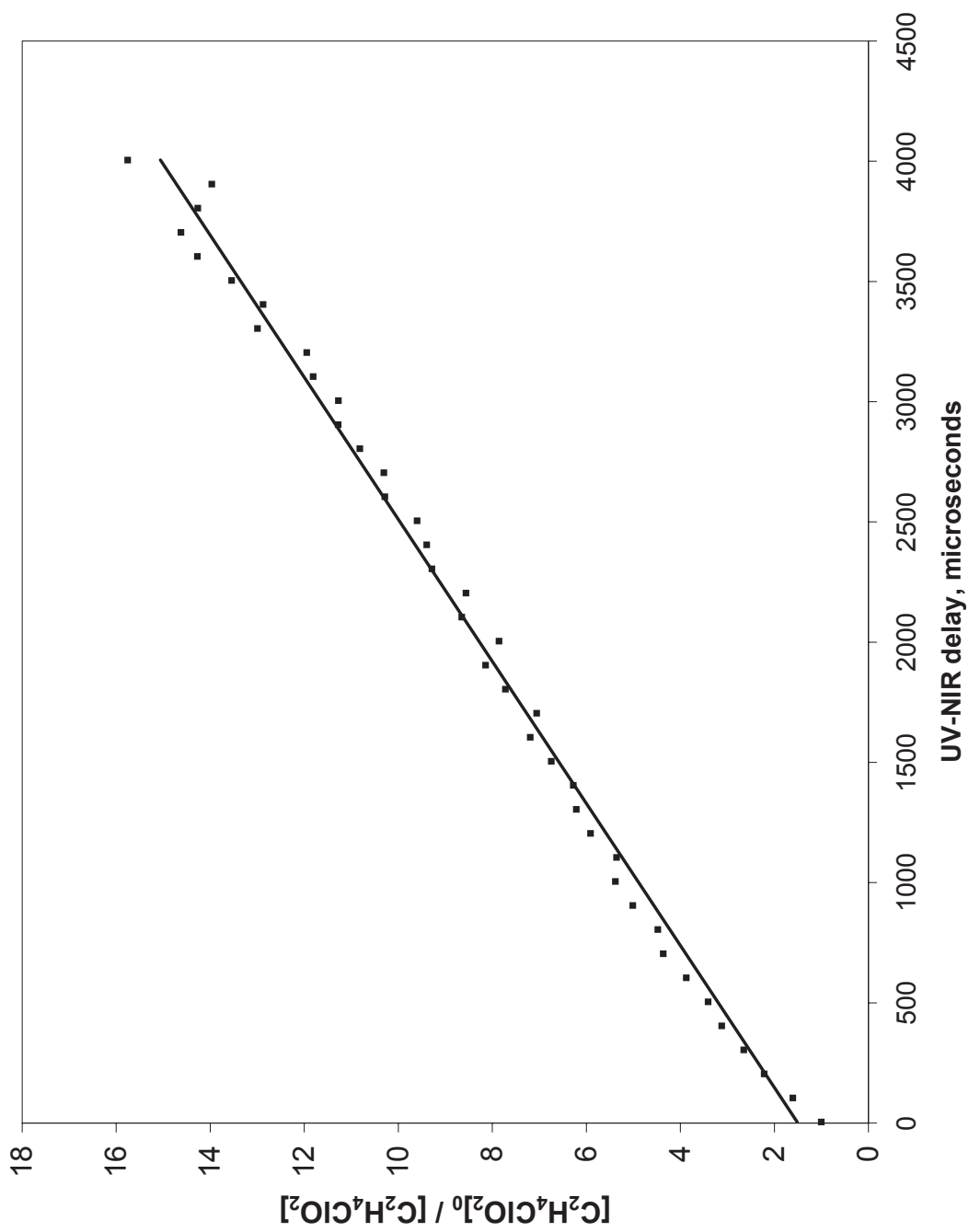


Figure 2.12: Kinetics of $C_2H_4ClO_2$ self-reaction.

Chapter 3

Cavity Ringdown Spectroscopy of the $\tilde{A} \ ^2E'' \leftarrow \tilde{X} \ ^2A'_2$ electronic transition of NO_3

3.1 Introduction

The nitrate radical plays an important role in atmospheric chemistry. Although NO_3 photolyzes rapidly in the visible ($\lambda < 600 \text{ nm}$) and its concentration is quite low during the daytime, it significantly rises at night and the nitrate radical becomes a dominant atmospheric oxidant. Reactivity of NO_3 towards other atmospheric species and its spectroscopy in the visible and mid-infrared have been extensively studied [1]. However, prediction of its electronic structure and the process of photodissociation presents a challenge for the modern electronic structure theory [2]. The main difficulty of treating NO_3 lies in its high symmetry. As an open-shell molecule with a C_3 axis, NO_3 must exhibit Jahn-Teller effect in its degenerate electronic states. Therefore, in addition to its atmospheric significance, NO_3 radical itself is an interesting quantum system. Although our theoretical understanding of Jahn-Teller effect has greatly advanced since its discovery in 1937 [3], it is still treated on a case-by-case basis and

its influence on the potential energy surfaces of NO_3 is poorly understood.

The electronic configurations of the ground state \tilde{X} , $(4e')^4(1e'')^4(1a'_2)^1$ and the excited state \tilde{B} were correctly predicted by Walsh [4] more than fifty years ago. The ground state of NO_3 has a planar D_{3h} geometry. Even this singly-degenerate state was the subject of some controversy a decade ago. Several *ab initio* studies initially predicted shallow C_{2v} minima around the D_{3h} geometry [5, 6] (and ref. therein), while spectroscopic studies of the vibrational bands indicated that NO_3 belonged to the D_{3h} group [7, 8, 9]. This was later resolved by Einfeld and Morokuma [2] who showed that the symmetry breaking of the Hartree-Fock wavefunctions led to artifactual symmetry breaking in the ground state and it was necessary to use MRCI with symmetrically correct wavefunctions to avoid this problem.

In the ground state, the unpaired electron occupies the $1a'_2$ orbital comprised of three in-plane p-orbitals of the oxygen atoms. Thus, the ground state has ${}^2A'_2$ symmetry. NO_3 has six internal degrees of freedom. In the D_{3h} geometry, they correspond to two singly-degenerate modes (symmetric stretch ν_1 (a'_1) and out-of-plane bend ν_2 (a''_2)) and two doubly-degenerate vibrational modes (asymmetric stretch ν_3 (e') and in-plane bend ν_4 (e')) (see Fig. 3.2). The frequencies of the normal modes in the ground state were found to be 1053, 762, 1492 and 368cm^{-1} , respectively [7, 9, 10].

Single excitations of electrons from the $(1e'')$ and $(4e')$ orbitals to the $(1a'_2)$ orbital produce the first two excited states, $\tilde{A} {}^2E''$ and $\tilde{B} {}^2E'$, respectively. Both of these states are doubly-degenerate and therefore, must exhibit Jahn-Teller effect. The

$\tilde{B} \leftarrow \tilde{X}$ transition, first observed in the gas phase by Jones and Wulf [11], gives rise to broad unstructured absorption bands between 680 and 450 nm. The transition is very strong, with the peak cross-section reaching $\sigma(662 \text{ nm}) = 2 \times 10^{-17} \text{ cm}^2$ and for this reason, is routinely used for monitoring of the NO_3 concentration in the atmosphere. Because of its practical importance, the $\tilde{B} \leftarrow \tilde{X}$ transition has been extensively studied. However, optical spectroscopy could not reveal much information about the \tilde{B} state. The broad unassignable features of the $\tilde{B} \leftarrow \tilde{X}$, even under jet-cooled conditions [12] together with the anomalously long fluorescence lifetime of the \tilde{B} state ($2.8 \mu\text{s}$ [13]) suggests that it is strongly coupled to the vibrational levels of the ground state.

The first electronic state $\tilde{A} \ ^2E''$ of NO_3 has also not been well characterized. The transition $\tilde{A} \leftarrow \tilde{X}$ is electronically forbidden, and therefore even the bands that become allowed by vibronic coupling (Herberg-Teller effect) or nonadiabatic effect are weak. The \tilde{A} state was first discovered by Weaver *et al.* [14] in a photoelectron spectrum of NO_3^- anion. The observed band originated $7000 \pm 110 \text{ cm}^{-1}$ above the ground state of neutral NO_3 . The series of resolved peaks were fit to harmonic progressions of two modes, $541 \pm 8 \text{ cm}^{-1}$ and $804 \pm 4 \text{ cm}^{-1}$, which were assigned to ν_4 and ν_1 , respectively. Only two vibronic bands of the $\tilde{A} \leftarrow \tilde{X}$ transition have been observed so far. Kawaguchi *et al.* discovered two near-IR absorption bands at 7600 and 7745 cm^{-1} in a FT-IR spectrum of NO_3 [15] and attributed them to the transitions to $\nu_4 = 1$ and $\nu_2 = 1$ levels of the $\tilde{A} \ ^2E''$ state. Hirota *et al.* then employed diode laser frequency modulation spectroscopy to obtain a rotationally

resolved spectrum of the 7600cm^{-1} band [16]. The band satisfied selection rules of a parallel transition and was assigned to a transition from the ground electronic state to the \tilde{X}^2A_2'' vibronic component of the ν_4 mode of the \tilde{A}^2E'' state. The upper state was adequately described by the symmetric top Hamiltonian with a diagonal spin-rotation term without perturbations. This result suggested that the \tilde{A} was symmetric, i.e., it exhibited dynamic Jahn-Teller effect.

This result seems to be in disagreement with the results of high level *ab initio* study of the excited states of NO_3 by Einfeld and Morokuma [17]. They optimized the structures of NO_3 in the \tilde{A} and \tilde{B} states at the CASSCF and MR-SDCI levels of theory and found that the \tilde{A} underwent significant Jahn-Teller distortion. C_{2v} geometry minima of B_2 symmetry of the \tilde{A} state were found $2000\text{-}3000\text{ cm}^{-1}$ below the conical intersection point (depending on the method). The transition states of A_1 symmetry between the minima were $800\text{-}1000\text{ cm}^{-1}$ higher in energy. Such a large stabilization energy and high barrier to pseudo-rotation indicate strong linear and quadratic Jahn-Teller effects in the \tilde{A} state.

The analysis of the potential energy surface of the \tilde{A} state requires more detailed information on its vibronic bands, but the experimental results available to date are sparse. In this work, we utilize the high sensitivity of the cavity ringdown technique and the wide tuning range of our near-infrared source to obtain a global spectrum of the $\tilde{A}^2E'' \leftarrow \tilde{X}^2A_2'$ transition in the $5900\text{-}10700\text{ cm}^{-1}$ region. Although the resolution of our laser system does not allow us to resolve separate rotational lines and perform a detailed analysis of the rotational structure, we should still be able to

extract some information about the geometry of NO_3 in different vibronic states from the rotational contours of the bands.

3.2 Experiment

The near-IR spectrum of NO_3 was recorded in a flow cell at room temperature. A detailed description of our experimental apparatus has been provided in chapter 1. In this experiment, the Raman cell was used in a 3-pass configuration. LDS698, LDS722, DCM, Oxizine-720 and Rhodamines 575, 590, 610 and 640 laser dyes (Exciton) were used to cover the 5900-10700 cm^{-1} region. In the 9800-10700 cm^{-1} region, the first Stokes component of the radiation generated by Raman scattering was used. Four sets of ringdown mirrors were used in the experiments: Newport 1 m ROC 1" diameter Ultra-Low Loss SuperMirrorsTM (5900-7000 and 7000-8000 cm^{-1} regions) and 6 m ROC 0.8 " diameter and 1 m ROC 1" diameter Los Gatos Research mirrors (7900-8950 and 8950-10700 cm^{-1} regions, respectively). An extended InGaAs photodiode (Hamamatsu) and an amplified Si photodiode (Thorlabs DET400) were used to detect near-IR radiation in the 5900-10000 cm^{-1} and >10000 cm^{-1} regions, respectively. Twenty waveforms were averaged before fitting the ringdown signal to a single-exponential decay.

In the initial experiments, NO_3 was generated by photolysis of N_2O_5 and ClONO_2 at 248 nm in our quartz photolysis cell (see Fig. 1.12). Later on, we switched to ozonolysis of N_2O_5 as a method of generating nitrate radical. NO_3 was produced in a steady state as an intermediate product of that reaction. This method allowed us

to use a much longer cell and thus, increase the sensitivity of the instrument. All the spectra reported here were acquired using our long-path cell described in chapter 1 (see Fig. 1.6). The mirrors were separated from the reaction region by approximately 20 cm long purge volumes. During the scans, a constant flow of nitrogen protected the mirrors from the reagents.

N_2O_5 is solid at the temperatures below 30°C . However, it slowly decomposes into N_2O_4 and O_2 above -10°C . N_2O_5 was always held in a cold trap. It was stored between the experiments in a methanol bath at -80°C . During the scans, the trap was immersed in a $\text{NaCl}/\text{H}_2\text{O}$ slush at -20°C . Ozone was produced by a corona discharge ozone generator (Ozotech, OZ2SS-SS) at the concentration of approximately 2.5% by weight. For convenience, we chose not to trap ozone but to use the ozone/oxygen mixture as a carrier gas for N_2O_5 . UHP oxygen at the pressure of 1.3 atm was flowed through the ozone generator. The O_3/O_2 mixture produced then passed through the N_2O_5 cold trap and entered the ringdown cell. The flow rate of the gas out of the cold trap was controlled by a teflon needle valve. The pressure in the cell was measured by a capacitance manometer (MKS BaratronTM). The partial pressure of nitrogen used to purge the mirrors was 15 Torr. The total pressure in the cell was maintained in the 50-55 Torr range during the scans. The total flow rate of the gas through the cell was 45 sccm, which corresponded to the residence time of 4.5 seconds. To eliminate the absorption bands of N_2O_5 and residual water, a background scan was taken after every run under the same conditions, but with the ozone generator off and subtracted from the spectrum.

The NO_3 concentration was measured between the scans by direct absorption at 661.5 nm using a diode laser (Thorlabs HL6501MG). The diode laser beam followed the same optical path as near-IR radiation. It entered and exited the cell through the cavity ringdown mirrors which were partially transparent to the visible radiation. The same photodiodes were used to measure the diode laser power exiting the cell. Typically, 5-10% of the 661.5 nm radiation was absorbed in a single pass, which corresponded to the NO_3 concentration in the $8 \times 10^{13} - 2 \times 10^{14}$ mol/cm³ range. Scans with different laser dyes were scaled by matching the intensities of the bands present on the overlapping regions of the spectrum. If there were no such bands, the measured NO_3 concentration was used for that purpose.

3.3 Results and Discussion

3.3.1 Experimental Results

We detected a series of absorption bands in the 5900-10700 cm⁻¹ region. Strong absorption of the first and second overtones of the OH stretch of nitric acid present in the cell prevented detection in the 6900-7000 cm⁻¹ and 10130-10180 cm⁻¹ regions. Only two weak bands were found in the 5900-7550 cm⁻¹ region, centered at around 6700 and 7200 cm⁻¹. No absorption was detected at the origin, $\nu_{00} \approx 7060$ cm⁻¹. Above 7550 cm⁻¹, we observed a series of bands which became increasingly congested, especially above 8700 cm⁻¹. The unscaled scans after background subtraction are shown in Fig. 3.4-3.14. All observed bands besides the HNO_3 overtones were at-

tributed to NO_3 . The first two bands in the region above 7550 cm^{-1} were previously reported by Kawaguchi *et al.* [15].

At room temperature, the rotational contours of NO_3 bands have widths of approximately 50 cm^{-1} . All but two bands in the region below 10200 cm^{-1} have sharp bandheads; this allows us to distinguish separate bands in the congested part of the spectrum. In the region above 10200 cm^{-1} , the spectral features become very broad and unstructured, and the bandheads are no longer resolved. The positions of the observed vibronic bands below 9000 cm^{-1} and their relative intensities are summarized in Table 3.1. We estimate the empirical peak absorption cross-section of this transition to be $\sigma(1.29 \mu\text{m}) = 6 \times 10^{-20} \text{ cm}^2$, with the average cross-section being a factor of 5 lower.

Simulation of rotational contours of vibronic bands of NO_3 with the rotational constants obtained by Hirota *et al.* shows that parallel and perpendicular bands have easily distinguishable profiles (see Fig. 3.15). *R*-branches in the bands of both types form sharp bandheads caused by the lengthening of the N-O bond upon excitation to the $\tilde{\text{A}}$ state ($r_{\text{NO}} = 1.27 \text{ \AA}$ versus $r_{\text{NO}} = 1.20 \text{ \AA}$ in the ground state). However, perpendicular bands have a sharper bandhead and do not have a gap between the *P*- and *R*-branches. All but two well resolved bands resemble one of the two profiles and can be identified as parallel or perpendicular bands. The 8290 cm^{-1} and 9620 cm^{-1} bands are the only ones that do not resemble the simulated contours. The majority of the well-resolved bands in the spectrum are perpendicular bands. Only eight bands can be identified as parallel bands. There is only one other obvious progression in

the spectrum formed by the 7600, 8120, 8670 and 9180 cm^{-1} parallel bands.

3.3.2 Assignment

A forbidden electronic transition can become allowed via vibronic coupling. In this case, we have to consider the total vibronic symmetry of the vibrational states, $\Gamma^{ve} = \Gamma^{el} \otimes \Gamma^{vib}$. Only the vibronic transitions for which the product, $\Gamma^{ve'} \otimes \Gamma^{\mu} \otimes \Gamma^{ve''}$ contains a totally symmetric irreducible representation, are allowed. Totally symmetric vibrations still remain forbidden because for them, $\Gamma^{ve} = \Gamma^{el}$; thus the ν_1 mode should not be present in the $\tilde{A} \leftarrow \tilde{X}$ spectrum. This mode can only be active in a combination with other allowed modes.

The "vibrationless" state of the ground electronic state is totally symmetric and therefore has A_2' vibronic symmetry. The (x, y) - and z -components of the dipole moment have E' and A_2'' symmetries. Thus, only vibronic states with symmetries of $\Gamma^{ve} = A_1''$ or E' for parallel and perpendicular bands, respectively, can be accessible from the $\tilde{X}(0000)$ state.

The umbrella mode, ν_2 and its even overtones have $a_2'' \otimes E'' = E'$ vibronic symmetry and will give rise to perpendicular bands. Moreover, the a_2'' modes are the only modes of NO_3 that can mix the \tilde{A} and \tilde{B} states, and "borrow" intensity from the strong $\tilde{B} \leftarrow \tilde{X}$ transition. Therefore, we expect them to be the strongest bands in the spectrum.

The Jahn-Teller active, doubly-degenerate modes, ν_3 and ν_4 in the $\tilde{A} E''$ state split into 3 vibronic states ($e' \otimes E'' = A_1'' + A_2'' + E''$). Only the A_1'' components can

be observed as parallel bands. The overtones and combination bands of these modes will split into a larger number of vibronic states of the same symmetries, A_1'' , A_2'' and E'' .

Combinations of the ν_2 mode with ν_3 and ν_4 will have vibronic components of the A_1' , A_2' and E' symmetries. Only the E' components can be accessed from the ground level. These transitions would correspond to perpendicular bands in the spectrum.

Other vibrational levels of the ground state \tilde{X} may have a completely different set of selection rules. For example, the $\tilde{X}(0001)$ state has $e' \otimes A_2' = E'$ symmetry. From this level, the states of A_1' , A_2' and E' symmetry will be accessible via perpendicular transitions and the states of E'' symmetry via a parallel transition.

The first band, located at 6695.7 cm^{-1} , is the only band we observed below the dark origin $7061 \pm 8 \text{ cm}^{-1}$ (from ref.[16]) of the $\tilde{A} \leftarrow \tilde{X}$ transition. Its spacing from the origin ($\approx 365 \text{ cm}^{-1}$) is very close to the frequency of the ν_4 mode in the ground state, 368 cm^{-1} [10]. At room temperature, this mode has a Boltzmann factor of 0.34, consistent with the observed intensity. The transition from the $\tilde{X}(0001)$ state to the "vibrationless" level of the $\tilde{A} \ ^2E''$ electronic state is allowed by the z -component of the dipole moment operator. This transition should produce a parallel band and indeed, the contour of the 6695.7 cm^{-1} band resembles the contours of the other parallel bands. If this band belonged to a transition to the other Jahn-Teller surface of the \tilde{A} state, one would expect to see other bands of the transition to the blue from 6700 cm^{-1} . However, only one other band was observed in the $6700\text{-}7600 \text{ cm}^{-1}$ region. Therefore, we can unambiguously assign the 6700 cm^{-1} band to the 4_1^0 transition.

The hot band allows us to determine with more confidence the position of the origin. Using the value of $6695.7 \pm 1 \text{ cm}^{-1}$ for the band origin obtained from rotational contour analysis and the value of 368 cm^{-1} for the ground state, ν_4 from an LIF experiment [10], we estimate $\nu_{00}=7064 \text{ cm}^{-1}$. The accuracy is limited by the uncertainty in determining the origin of the LIF band. However, the current value is more accurate than the previously reported value of $7061 \pm 8 \text{ cm}^{-1}$, which was based on the ν_4 frequency of 540 cm^{-1} in the PES spectrum. The $\pm 8 \text{ cm}^{-1}$ uncertainty comes from fitting the PES peaks to harmonic progressions [14]. Given the large shifts in the overtone frequencies of this Jahn-Teller active mode, these error bars are likely to be optimistic.

Ab initio calculations of Einfeld and Morokuma [17] and Stanton [18] predict the stabilization energy of 2000-3000 cm^{-1} in the \tilde{A} state of NO_3 . Numerous works of Miller *et al.* [19, 20, 21, 22, 23, 24, 25, 26] on Jahn-Teller effect in ions and radicals have demonstrated that even a much smaller Jahn-Teller stabilization produces splittings of the vibronic levels of several hundred wavenumbers. In a molecule with strong Jahn-Teller effect, the progressions of the JT active vibrations are highly irregular and their "frequencies" are no longer observable directly. The frequencies of these modes defined by equation (3.11) can be obtained, in most cases, only by adjusting ν and the Jahn-Teller coupling constants to fit the eigenvalues of the Jahn-Teller Hamiltonian to the experimental data. Moreover, for the Jahn-Teller active modes, ν is no longer a good quantum number [26]. In our assignment of the vibronic bands, it will be used only to indicate the state with the largest contribution to the eigenfunction of

the Jahn-Teller Hamiltonian.

The progression of parallel bands at 7602, 8127, 8673 and 9182 cm^{-1} in the NO_3 spectrum could only correspond to an e' mode. Since the frequency of the ν_3 mode is much larger than the average spacing between the bands, the progression can only be attributed to the ν_4 vibration. This confirms the assignment of Hirota *et al.* The spacings between the bands and the origin are 539(1), 519(1), 547(1) and 509(1) cm^{-1} . Such an irregular pattern indicates the presence of the Jahn-Teller coupling. Without modeling the spectrum with the correct Jahn-Teller constants, we can only conclude that in the $\tilde{\text{A}}$ state, the frequency of the ν_4 mode is in the 509-550 cm^{-1} range. This value is 50% larger than the frequency in the ground state.

According to the selection rules, all observed perpendicular bands must involve the umbrella mode, ν_2 . The 7745 cm^{-1} band the first and strongest perpendicular band corresponds to a 678 cm^{-1} vibration. This frequency is too small for a combination band. Thus, this band could only be assigned to the fundamental of the ν_2 in agreement with Kawaguchi *et al.* Therefore, the 9080 cm^{-1} band should correspond to $3\nu_2$.

The combination of ν_1 and ν_2 will also have a_2'' symmetry and should also give a strong perpendicular band. Since ν_1 is expected to be around 800 cm^{-1} , only the 8530 cm^{-1} band fits that description. Assigning it to $\nu_1 + \nu_2$ gives us the value of 782 cm^{-1} for ν_1 and also leads to the possible assignment of the 8370 and 8900 cm^{-1} bands to $\nu_1 + \nu_4$ and $\nu_1 + 2\nu_4$. This assignment is tentative, as it is difficult to identify whether the 8370 and 8900 cm^{-1} bands are parallel or perpendicular bands

due to their overlap with adjacent bands. The values of ν_1 in these combination bands are 758 and 776 cm^{-1} , respectively. The differences in obtained ν_1 frequencies are likely due to anharmonicity and/or bilinear vibronic coupling between the ν_1 and ν_4 modes. The obtained frequency of the ν_1 mode agrees well with the one obtained by photoelectron spectroscopy. The observed ν_1 , ν_2 and ν_4 frequencies are also in agreement with the CASSCF frequencies calculated by Einfeld and Morokuma [17], and Stanton [18].

3.3.3 Theoretical framework

Jahn-Teller effect is a special case of a conical intersection between adiabatic potential energy surfaces. In the vicinity of an intersection point between electronic states of the same symmetry, the Born-Oppenheimer approximation breaks down and non-adiabatic coupling between the electronic and nuclear motion becomes significant. The Jahn-Teller theorem, as formulated in the original paper [3] states: "*All non-linear nuclear configurations are unstable for an orbitally degenerate state.*" It refers to molecules in which electronic degeneracy is not accidental (caused by symmetry). Jahn and Teller showed that molecules of the point groups with degenerate representations (with at least one C_n axis, $n > 2$) must have a degenerate mode, displacement along which will lower the energy of the molecule. The Jahn-Teller distortion usually cannot be observed directly (for reasons that will be discussed below); however, the breakdown of the Born-Oppenheimer approximation in the vicinity of the conical intersection between the split potential energy surfaces usually produces

spectroscopically observable effects. Jahn-Teller systems attract special attention because it is possible to calculate analytically the adiabatic potential energy surfaces near JT conical intersections and predict their properties.

The derivation of analytical expressions for the JT potential energy surfaces can be found in the works of Liehr [27, 28] and Bersuker [29] (and refs. therein). Generally, vibronic coupling is treated by dividing the total Hamiltonian of the molecule into a purely electronic term, H^{el} , a nuclear kinetic energy term, T^{nucl} , and a term, $V(r, Q)$ that includes electron-nuclear and nuclear-nuclear interactions

$$H = H^{el} + T^{nucl} + V(r, Q), \quad (3.1)$$

where r and Q denote the electronic and nuclear coordinates, respectively. Initially, the Schrödinger equation is solved with $V(r, 0)$, evaluated at the undistorted geometry $Q_i = 0$. Here, i labels the normal modes of the system. Afterwards, the omitted $V(r, Q) - V(r, 0)$ term called "vibronic coupling" is included as a perturbation.

The "vibronic coupling" term is normally expanded in Taylor series at $Q_i = 0$ point

$$V(r, Q) - V(r, 0) = \sum_{i=1}^N \left(\frac{\partial V}{\partial Q_i} \right)_0 Q_i + \frac{1}{2} \sum_{i=1}^N \sum_{j=1}^N \left(\frac{\partial^2 V}{\partial Q_i \partial Q_j} \right)_0 Q_i Q_j + \dots \quad (3.2)$$

and only the first two terms are retained, resulting in the so-called linear and quadratic Jahn-Teller effect. Vibronic coupling lifts the degeneracy of the eigenfunctions of the Hamiltonian $H_0 = H^{el} + T^{nucl} + V(r, Q)$. The energies of such states can be found as

solutions of the secular equation.

In the case of a doubly-degenerate state interacting with doubly-degenerate vibrations ($E \otimes e$), when the quadratic Jahn-Teller coupling between the active modes, g_{ij} is neglected, the adiabatic potential energy surfaces will have the form (in notation used by Barckholtz and Miller [30])

$$U_{\pm} = \sum_{i=1}^{N-r} \frac{1}{2} \lambda_i Q_i^2 + \sum_{i=N-r+1}^N \left(\frac{1}{2} \lambda_i Q_i^2 \pm \rho_i k_i \left(1 + \frac{2g_{ii}\rho_i}{k_i} \cos(n\theta_i) + \frac{g_{ii}^2 \rho_i^2}{k_i^2} \right)^{1/2} \right), \quad (3.3)$$

where r is the number of Jahn-Teller active modes, ρ_i and θ_i are the polar coordinates representing doubly-degenerate modes $Q_i^{\pm} = \rho_i e^{i\theta_i}$, and

$$\lambda_i = \langle \phi_1 | \left(\frac{\partial^2 V}{\partial Q_i^+ \partial Q_i^-} \right)_0 | \phi_1 \rangle \quad (3.4)$$

$$k_i = \langle \phi_1 | \left(\frac{\partial V}{\partial Q_i^{\pm}} \right)_0 | \phi_2 \rangle \quad (3.5)$$

$$g_{ij} = \langle \phi_1 | \left(\frac{\partial^2 V}{\partial Q_i^+ \partial Q_j^-} \right)_0 | \phi_2 \rangle. \quad (3.6)$$

The potential energy surface along each JT active coordinate will have the shape of a "mexican hat" (see Fig. 3.1). If both the linear term, k_i and the quadratic term, g_{ii} are non-zero, the surfaces will have a θ -dependence with n -fold symmetry; thus, there will be n maxima and n minima on the moat. If only one of these terms is non-zero, all the points on the moat will have the same energy.

It is convenient to use the dimensionless linear D and quadratic K Jahn-Teller

coupling constants for the following discussion:

$$D = \frac{k^2}{2\hbar} \sqrt{\frac{M}{\lambda^3}} \quad (3.7)$$

$$K = \frac{g}{\lambda}. \quad (3.8)$$

The total Jahn-Teller stabilization energy E_{JT} and the depth of the wells on the moat ΔE can be described in terms of the frequencies of the Jahn-Teller active modes ω_i

$$E_{JT} \approx -D\omega(1 + K), \quad (3.9)$$

$$\Delta E = E_{max} - E_{min} = -2DK\omega, \quad (3.10)$$

where ω is defined as

$$\omega = \frac{1}{2\pi} \sqrt{\frac{\lambda}{M}}. \quad (3.11)$$

Thus, if there are vibrational levels in the moat ($D > 1$), the molecule will be distorted, but generally speaking, the vibrational wavefunction will be delocalized and the observed averaged geometry will be the same as that of an undistorted molecule. This phenomenon is often referred to as "dynamic" Jahn-Teller effect, and the motion around the conical intersection is referred to as "pseudo-rotation". If the quadratic term, K is large enough that the wells on the moat can support vibrational levels, the wavefunction will become localized and a "static" distortion will be observed.

We must note that the Jahn-Teller constants D and K have different values for each JT active mode. Therefore, the total stabilization energy is divided between

all JT active modes. If the quadratic Jahn-Teller coupling between the modes is negligible, then the stabilization energy is the sum over all JT modes [31]

$$E_{JT} \approx \sum_i -D_i \omega_i (1 + K_i). \quad (3.12)$$

Jahn-Teller active molecules must have open shell configurations, i.e., non-zero spin. Thus, the spin-orbit coupling term, $a\mathbf{SL}$ must also be introduced into the Hamiltonian. It also can be treated as a perturbation. The order in which spin-orbit coupling and Jahn-Teller coupling are added to the Hamiltonian depends on the relative magnitude of these effects. Spin-orbit effect decreases the Jahn-Teller stabilization and can completely quench JT effect, and vice versa. In polyatomic molecules without heavy atoms, the spin-orbit coupling constant is usually small (less than 100 cm^{-1}).

3.3.4 Rotational contour analysis

The major discrepancy between the theory and experiment for the \tilde{A} state of NO_3 is the absence of static Jahn-Teller distortion in the $\tilde{A}(0001)$ state analyzed by Hirota *et al.* It could only be explained by the fact that the potential wells on the moat around the conical intersection point in the Q_4^\pm normal coordinate are not deeper than $2\nu_4$. This will lead to only dynamic Jahn-Teller distortion in the state, which, on average, will give a D_{3h} structure. We also have to make the assumption that the wells along the Q_3^\pm normal coordinates do not support any levels ($< \nu_3$); otherwise, the molecule would still be distorted along these coordinates in the $\tilde{A}(0001)$ state.

However, if the theoretical results are correct, one might still expect to observe static Jahn-Teller distortion of NO_3 in the "vibrationless" state and the states with $\nu_4 = 0$.

We simulated the rotational contours of several vibronic bands in search of evidence of static Jahn-Teller distortion of NO_3 . Static distortion leads to asymmetry in the averaged structure; thus, the symmetric Hamiltonian will no longer adequately describe the molecule. We employed SPCAT [32] and Asyrot [33] programs to model the rotational contours using symmetric and asymmetric top Hamiltonians, respectively. Our simulations included the known centrifugal constants for the ground state \tilde{X} and the $\tilde{A}(0001)$ state; however, the spin-rotation and Coriolis coupling were ignored. We started with checking whether the symmetric top model adequately describes the ν_4 bands. We used the rotational constants of Hirota *et al.* [16] for both the upper and lower states. The simulations using the symmetric top Hamiltonian indeed fit the observed profiles well (see Fig. 3.16). For the $2\nu_4$ and $3\nu_4$ bands, the upper state constants B' and C' had to be scaled by 0.987 and 0.975 to achieve better agreement with the experiment.

The symmetric top model, however, failed for the $-\nu_4$ (6700 cm^{-1}) and ν_2 (7745 cm^{-1}) bands. The results of the simulations using both symmetric and asymmetric rotor Hamiltonians are shown in Fig. 3.17 and 3.18. Since the rotational constants of the $\tilde{X}(0001)$ state are not known, we used the ground state $\tilde{X}(0000)$ constants for the lower state of the band. The rotational constants of NO_3 decrease by 5.5% percent upon excitation to the \tilde{A} state. Excitation of vibrational bands leads to an order of magnitude smaller change in the constants [8, 9]. Thus, using the ground state

constants for the "hot" 6700 cm^{-1} band would not lead to significant qualitative changes in the simulated contours. The symmetric top Hamiltonian was not able to predict the width of the bandhead of the 6700 cm^{-1} band, nor the blue shoulder of the 7745 cm^{-1} band. Varying the rotational constant B of the upper state with locked planar symmetric top relationship $A' = B' \approx C'/2$ only slightly shifted the position of the bandheads without affecting the overall shapes of the bands. We found it was necessary to break the $A' = B'$ symmetry to obtain qualitative agreement with the experiment. The contours simulated with the asymmetric rotor model with $A' = 0.461\text{ cm}^{-1}$, $B' = 0.411\text{ cm}^{-1}$, $C' = 0.216\text{ cm}^{-1}$; and $A' = 0.434\text{ cm}^{-1}$, $B' = 0.416\text{ cm}^{-1}$, $C' = 0.216\text{ cm}^{-1}$ for the 6700 and 7745 cm^{-1} bands, respectively, produced the best fit of the experimental data.

The most intriguing fact about the $\tilde{A} \leftarrow \tilde{X}$ spectrum of NO_3 is the absence of an obvious progression of the asymmetric stretch, ν_3 . This JT active mode should be vibronically allowed and have favorable Franck-Condon factors. The frequency of ν_3 in the ground state \tilde{X} is 1492 cm^{-1} . Einfeld and Morokuma predicted that in the C_{2v} geometry, this mode would split into two singly-degenerate modes of frequencies, 1245 cm^{-1} and 1602 cm^{-1} (CASSCF). These values correspond to the $8300\text{-}8700\text{ cm}^{-1}$ region in the $\tilde{A} \leftarrow \tilde{X}$ spectrum. Although the shapes of some weak bands in this part of the spectrum are obscured, there are no obvious strong parallel bands in this region. Our suspicion, then, naturally fell on the 8290 cm^{-1} band the strongest in the spectrum in terms of integrated band strength. The contour of this band similar to the contour of the $-\nu_4$ band does not have a sharp bandhead. This similarity

indicates that NO_3 might also be distorted in this state, and the distortion is even larger than in the $\tilde{\text{A}}(0000)$. Using the asymmetric rigid rotor Hamiltonian, we were able to reproduce the overall shape of this band with the constants, $A' = 0.48 \text{ cm}^{-1}$, $B' = 0.39 \text{ cm}^{-1}$ and $C' = 0.215 \text{ cm}^{-1}$. The band is a C -type (\parallel) transition and therefore, it could be attributed to the ν_3 . Observation of another band of similar shape at 9620 cm^{-1} confirms this assignment. The spacings between the 8290 and 9620 cm^{-1} bands and the origin are 1224 and 1322 cm^{-1} . Two other parallel bands at 8960 and 9280 cm^{-1} can then be attributed to $\nu_3 + \nu_4$ and $\nu_3 + 2\nu_4$, respectively. The shapes of these bands indicate that NO_3 has an averaged D_{3h} structure in the $\tilde{\text{A}}(0011)$ and $\tilde{\text{A}}(0012)$ states. From these observations, we can conclude that the potential well on the moat in the Q_4^\pm coordinates can only support a single level, and the barrier to pseudorotation is between $\approx 540\text{-}1080 \text{ cm}^{-1}$. The higher distortion of the molecule in the $\tilde{\text{A}}(0010)$ state vs. the "vibrationless" state $\tilde{\text{A}}(0000)$ suggests that the potential energy surface cannot be adequately described without vibronic coupling between the modes, i.e., non-diagonal second, and perhaps higher order terms in equation (3.2) need to be included.

Simulation of rotational contours of the $n\nu_4$ bands also helped us notice the small features on the blue side of the contours ($20\text{-}30 \text{ cm}^{-1}$ to the blue from the bands; see Fig. 3.16). These features cannot be reproduced with the Hamiltonian used by Hirota *et al.* to fit their high resolution spectrum of the ν_4 , and we believe they belong to separate bands. Their weak intensities and insufficiently small blue-shifts do not allow us to assign them to sequential bands 4_n^n . Unfortunately, the sensitivity of our

instrument does not allow us to record the full rotational contours of these bands, and we can only hypothesize that they might belong to the "dark" A_2'' and E'' components of the $\tilde{A}(000n)$ states, made slightly allowed by the spin-orbit or high-order vibronic coupling.

3.4 Summary

The $\tilde{A} \leftarrow \tilde{X}$ transition of NO_3 is weak ($\sigma < 6 \times 10^{-20} \text{ cm}^2$) and is therefore, of little atmospheric importance. However, it provides an opportunity to study the Jahn-Teller in this molecule. The results of our study are consistent with earlier studies, but provide additional information. We find clear evidence of vibronic coupling in the vibrational progressions. The rotational structure of the vibronic bands varies widely, with the $\tilde{A}(0000)$, $\tilde{A}(0n00)$ and $\tilde{A}(00n0)$ states having distorted, asymmetric structures. The absence of apparent spin-orbit doublets indicates that the spin-orbit coupling is quenched by the strong linear Jahn-Teller coupling, $a\zeta_e \ll 4D\omega$. Our rotational contour analysis of the $\tilde{A}(0001)$ level supports the conclusion of Hirota *et al.* that this level has a symmetric D_{3h} structure. This observation leads us to conclude that the pseudo-rotation barrier in the Q_4^\pm degenerate coordinates can be overcome by a single-quantum excitation. The further distortion of the molecule upon ν_3 excitation is evidence of vibronic coupling between the ν_3 and ν_4 .

Further analysis of the \tilde{A} state will require computed Jahn-Teller coupling constants for the state, and possibly vibronic coupling constants with the \tilde{B} state. Spectroscopy of jet-cooled NO_3 may be necessary for identification of the vibronic bands

in the congested part of the spectrum above 8300 cm^{-1} .

Table 3.1: Band positions and intensities of the $\tilde{A} \leftarrow \tilde{X}$ transition of NO_3

Peak position, cm^{-1}	Center frequency, cm^{-1}	Relative intensity	Type	Assignment
6704	6696 ¹	0.26	<i>C</i> -type	$-\nu_4$
7610	7602.5 ²	1.00		ν_4
7745	7742 ¹	1.38	\perp	ν_2
7775		0.42		
7925		very weak		
7980		very weak		
8127	8121 ³	1.15		$2\nu_4$
8288 ¹		2.42	<i>C</i> -type	ν_3
8340		0.63	\perp	
8368		0.20		$\nu_1 + \nu_4$
8436(&8448)		0.81		
8527		0.10	\perp	$\nu_1 + \nu_2$
8673	8668 ³	0.67		$3\nu_4$
8764		0.66	\perp	
8815		0.13	\perp	
8835		0.22		
8890		1.06		
8903		0.20		$\nu_1 + 2\nu_4$

[1] Asym. top.

[2] Sym. top, Ref. [16].

[3] Sym. top

References

- [1] R. P. Wayne, I. Barnes, P. Biggs, J. P. Burrows, C. E. Canosamas, J. Hjorth, G. Lebras, G. K. Moortgat, D. Perner, G. Poulet, G. Restelli, and H. Sidebottom. *Atmospheric Environment Part a-General Topics*, 25(1):1–203, 1991.
- [2] W. Eisfeld and K. Morokuma. *Journal of Chemical Physics*, 113(14):5587–5597, 2000.
- [3] H. A. Jahn and E. Teller. *Proceedings of the Royal Society of London. Series A, Mathematical and Physical Sciences*, 161(905):220–235, 1937.
- [4] A. D. Walsh. *Journal of the Chemical Society*, pages 2301–2306, 1953.
- [5] V. R. Morris, S. C. Bhatia, and J. H. Hall. *Journal of Physical Chemistry*, 94(19):7414–7418, 1990.
- [6] V. R. Morris, S. C. Bhatia, and J. H. Hall. *Journal of Physical Chemistry*, 95(23):9203–9208, 1991.
- [7] T. Ishiwata, I. Tanaka, K. Kawaguchi, and E. Hirota. *Journal of Chemical Physics*, 82(5):2196–2205, 1985.

- [8] K. Kawaguchi, E. Hirota, T. Ishiwata, and I. Tanaka. *Journal of Chemical Physics*, 93(2):951–956, 1990.
- [9] R. R. Friedl and S. P. Sander. *Journal of Physical Chemistry*, 91(11):2721–2726, 1987.
- [10] B. S. Kim, P. L. Hunter, and H. S. Johnston. *Journal of Chemical Physics*, 96(6):4057–4067, 1992.
- [11] E. J. Jones and O. R. Wulf. *Journal of Chemical Physics*, 5:873–875, 1937.
- [12] R. T. Carter, K. F. Schmidt, H. Bitto, and J. R. Huber. *Chemical Physics Letters*, 257(3-4):297–302, 1996.
- [13] T. Ishiwata, I. Fujiwara, Y. Naruge, K. Obi, and I. Tanaka. *Journal of Physical Chemistry*, 87(8):1349–1352, 1983.
- [14] A. Weaver, D. W. Arnold, S. E. Bradforth, and D. M. Neumark. *Journal of Chemical Physics*, 94(3):1740–1751, 1991.
- [15] K. Kawaguchi, T. Ishiwata, E. Hirota, and I. Tanaka. *Chemical Physics*, 231(2-3):193–198, 1998.
- [16] E. Hirota, T. Ishiwata, K. Kawaguchi, M. Fujitake, N. Ohashi, and I. Tanaka. *Journal of Chemical Physics*, 107(8):2829–2838, 1997.
- [17] W. Eisfeld and K. Morokuma. *Journal of Chemical Physics*, 114(21):9430–9440, 2001.

- [18] J. F. Stanton. private communication.
- [19] T. A. Barckholtz and T. A. Miller. *Journal of Physical Chemistry A*, 103(14):2321–2336, 1999.
- [20] T. A. Barckholtz, M. C. Yang, and T. A. Miller. *Molecular Physics*, 97(1-2):239–254, 1999.
- [21] B. E. Applegate, T. A. Miller, and T. A. Barckholtz. *Journal of Chemical Physics*, 114(11):4855–4868, 2001.
- [22] B. E. Applegate, A. J. Bezant, and T. A. Miller. *Journal of Chemical Physics*, 114(11):4869–4882, 2001.
- [23] K. Raghavachari, R. C. Haddon, T. A. Miller, and V. E. Bondybey. *Journal of Chemical Physics*, 79(3):1387–1395, 1983.
- [24] T. J. Sears, T. A. Miller, and V. E. Bondybey. *Faraday Discussions*, (71):175–180, 1981.
- [25] B. E. Applegate and T. A. Miller. *Journal of Chemical Physics*, 117(23):10654–10674, 2002.
- [26] T. A. Barckholtz and T. A. Miller. *International Reviews in Physical Chemistry*, 17(4):435–524, 1998.
- [27] A. D. Liehr. *Journal of Physical Chemistry*, 67(2):389–471, 1963.
- [28] A. D. Liehr. *Journal of Physical Chemistry*, 67(2):471–494, 1963.

- [29] I. B. Bersuker. *Chemical Reviews*, 101(4):1067–1114, 2001.
- [30] T. A. Barckholtz and T. A. Miller. *International Reviews in Physical Chemistry*, 17(4):435–524, 1998.
- [31] T. A. Barckholtz and T. A. Miller. *Journal of Physical Chemistry A*, 103(14):2321–2336, 1999.
- [32] H. M. Pickett. *Journal of Molecular Spectroscopy*, 148(2):371–377, 1991.
- [33] R. H. Judge and D. J. Clouthier. *Computer Physics Communications*, 135(3):293–311, 2001.

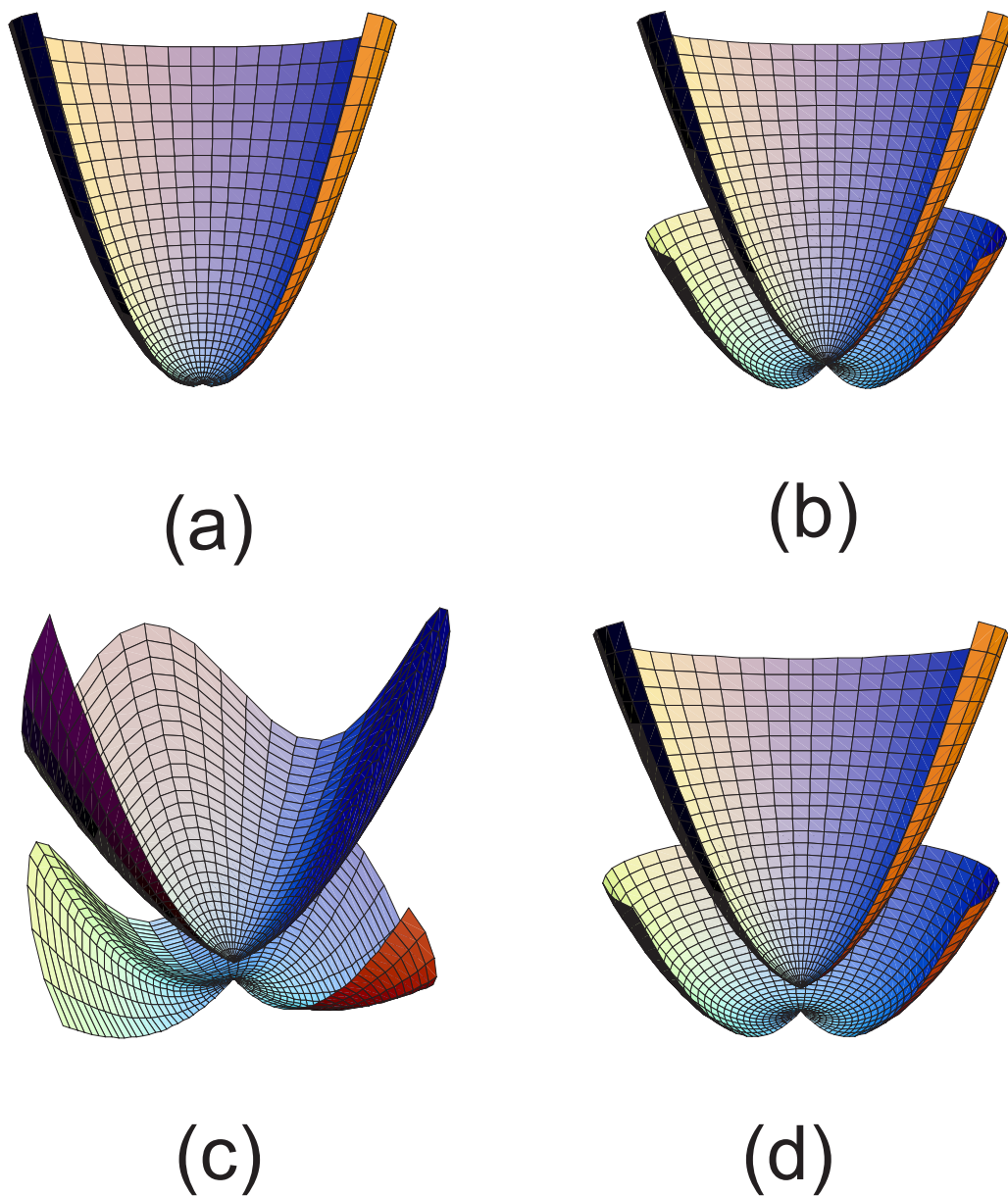


Figure 3.1: Potential energy surface of a doubly-degenerate electronic state along a Jahn-Teller active doubly-degenerate mode: (a) zero Jahn-Teller and zero spin-orbit coupling; (b) linear only Jahn-Teller coupling; (c) linear and quadratic Jahn-Teller coupling; (d) linear Jahn-Teller and spin-orbit coupling.

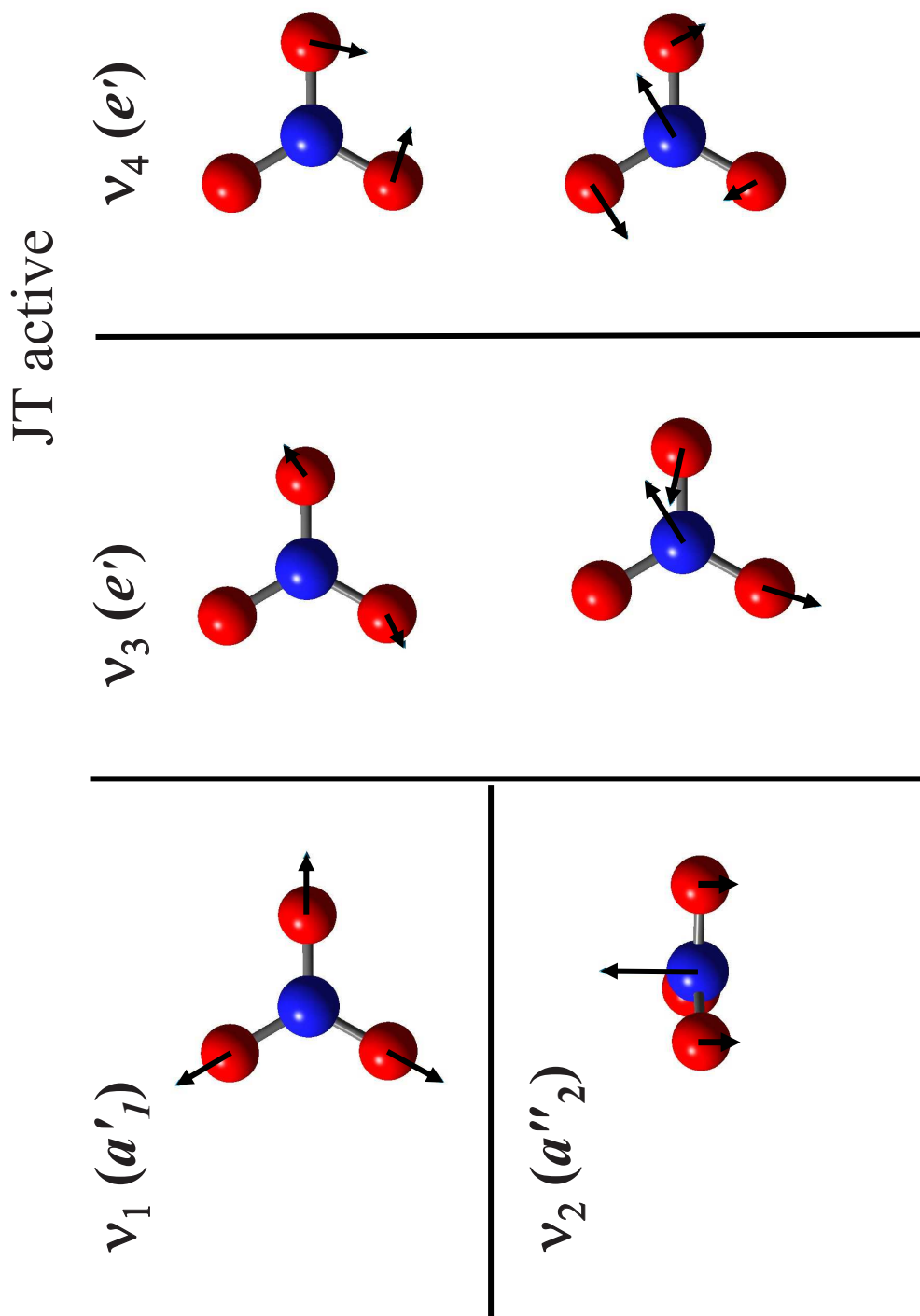


Figure 3.2: Normal modes of NO_3

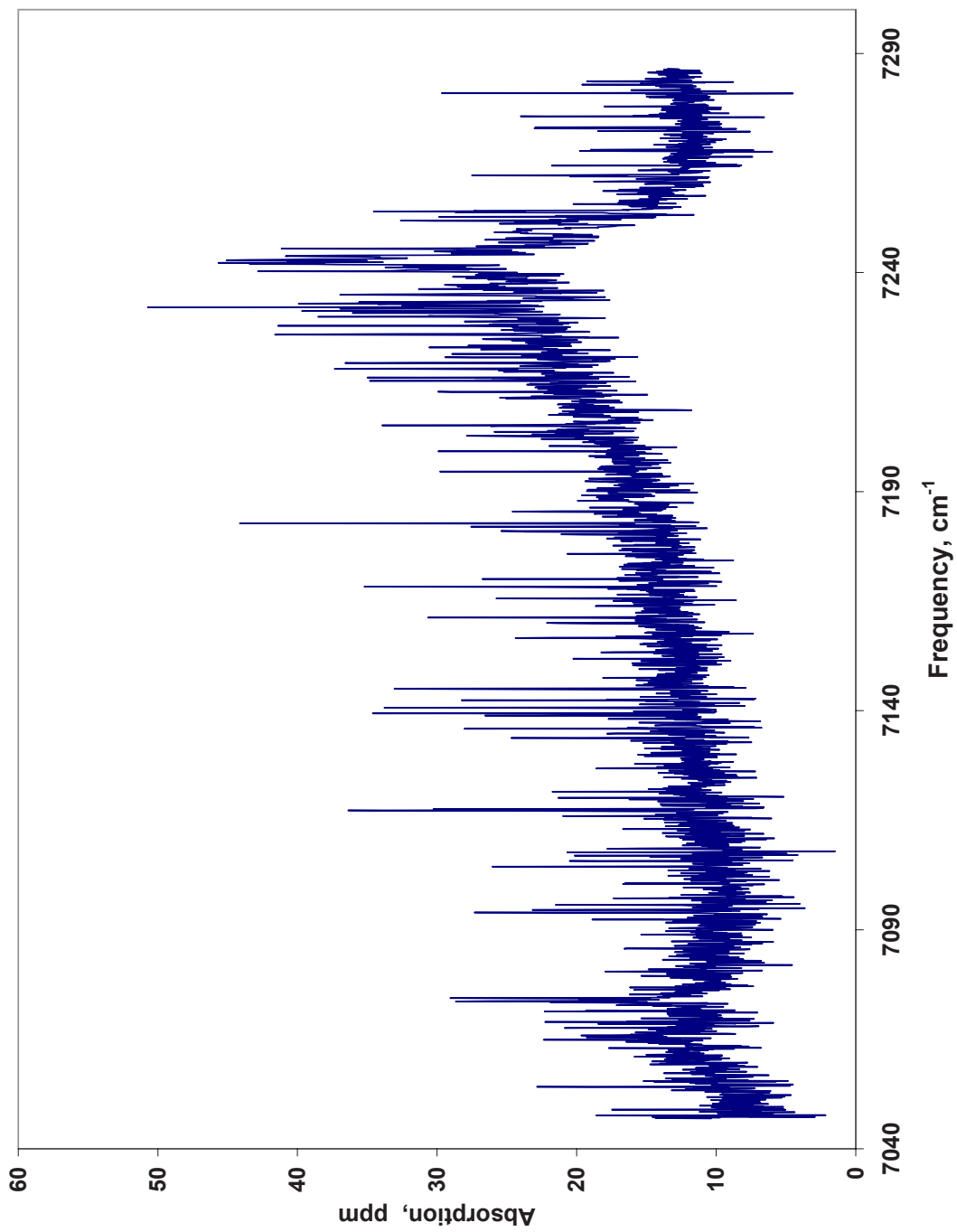


Figure 3.3: Cavity ringdown spectrum of the $\tilde{A} \leftarrow \tilde{X}$ transition of NO_3 in the 7050-7280 cm^{-1} region.

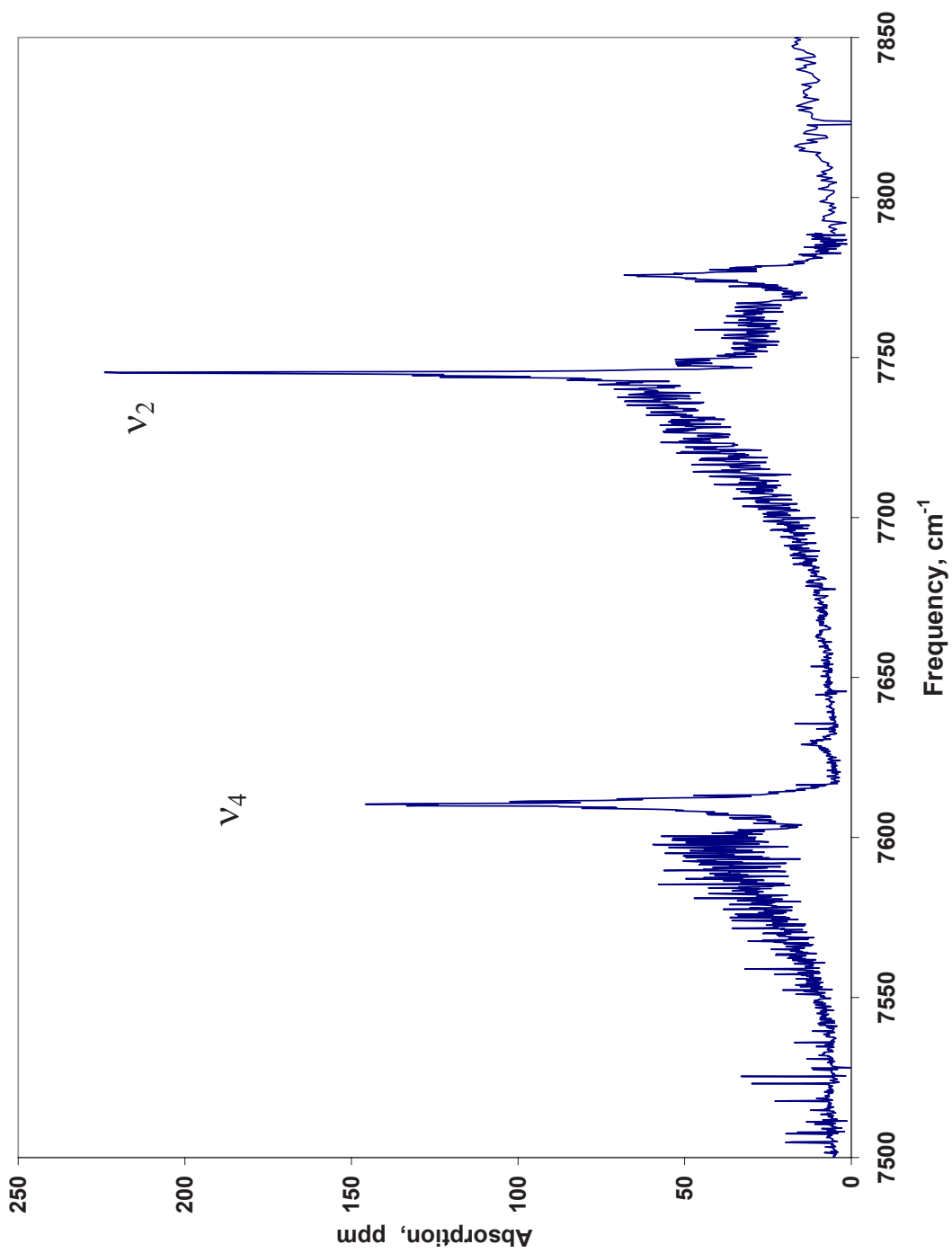


Figure 3.4: Cavity ringdown spectrum of the $\tilde{A} \leftarrow \tilde{X}$ transition of NO₃ in the 7500-7850 cm⁻¹ region.

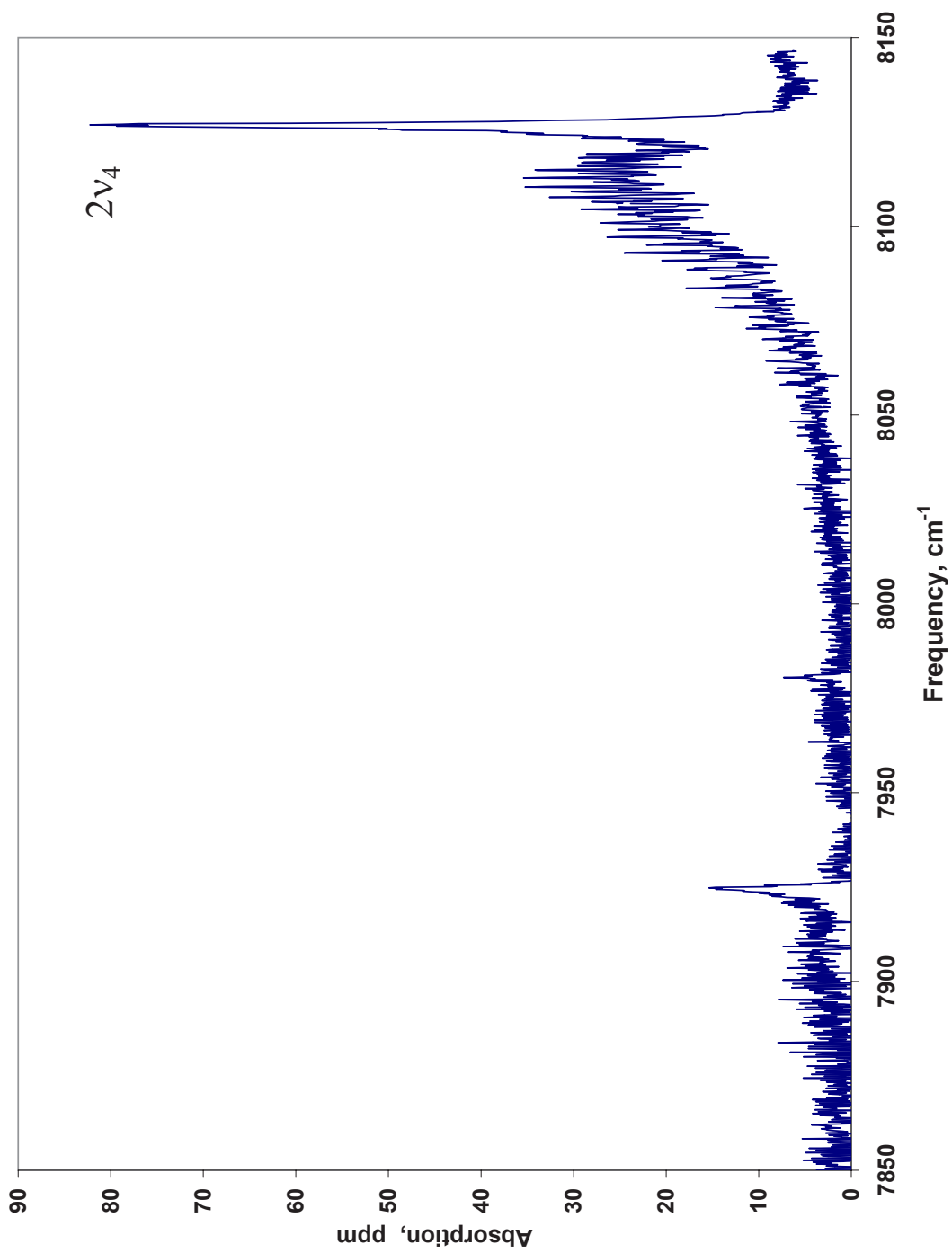


Figure 3.5: Cavity ringdown spectrum of the $\tilde{A} \leftarrow \tilde{X}$ transition of NO₃ in the 7850-8150 cm⁻¹ region.

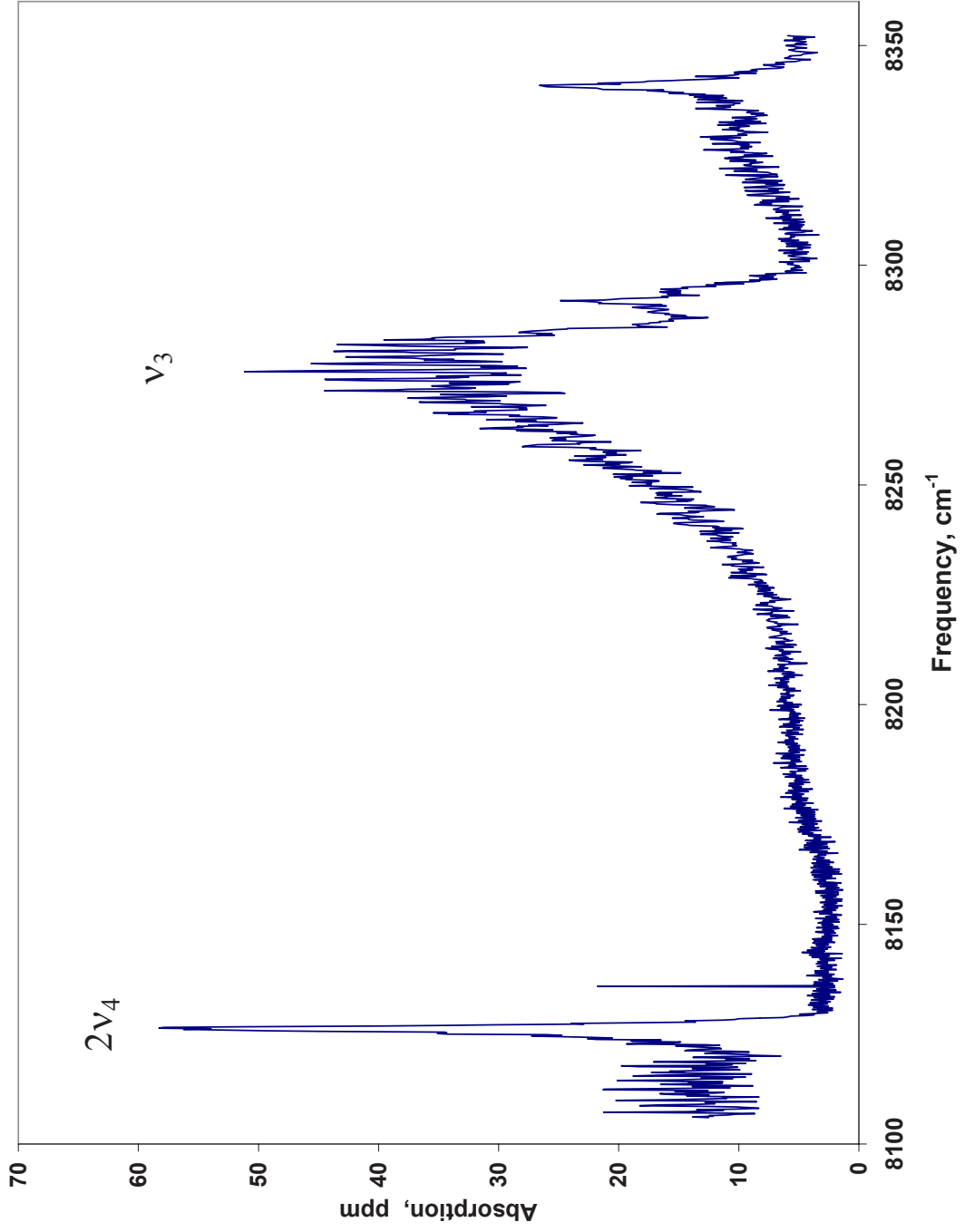


Figure 3.6: Cavity ringdown spectrum of the $\tilde{A} \leftarrow \tilde{X}$ transition of NO₃ in the 8100-8350 cm⁻¹ region.

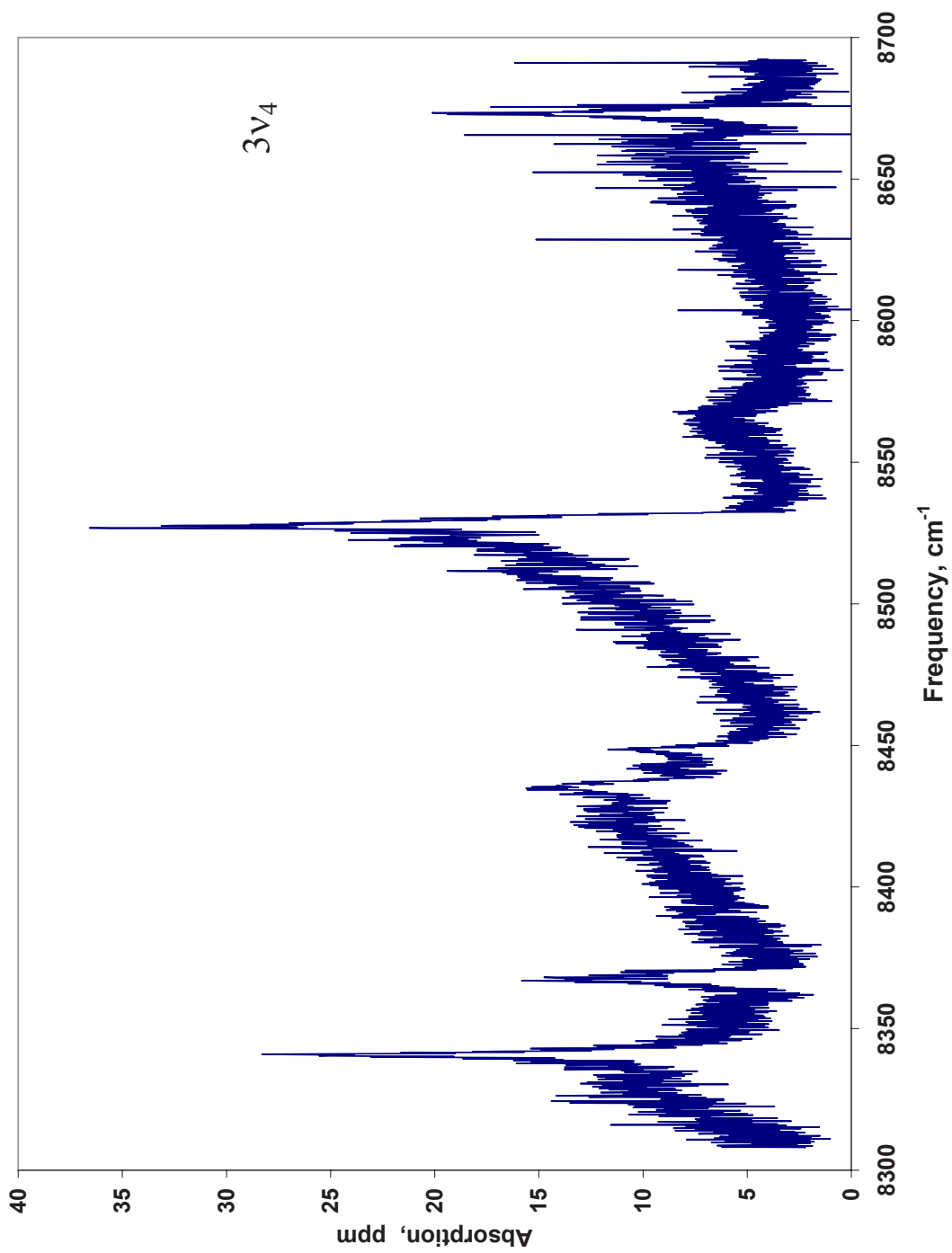


Figure 3.7: Cavity ringdown spectrum of the $\tilde{A} \leftarrow \tilde{X}$ transition of NO₃ in the 8300-8700 cm⁻¹ region.

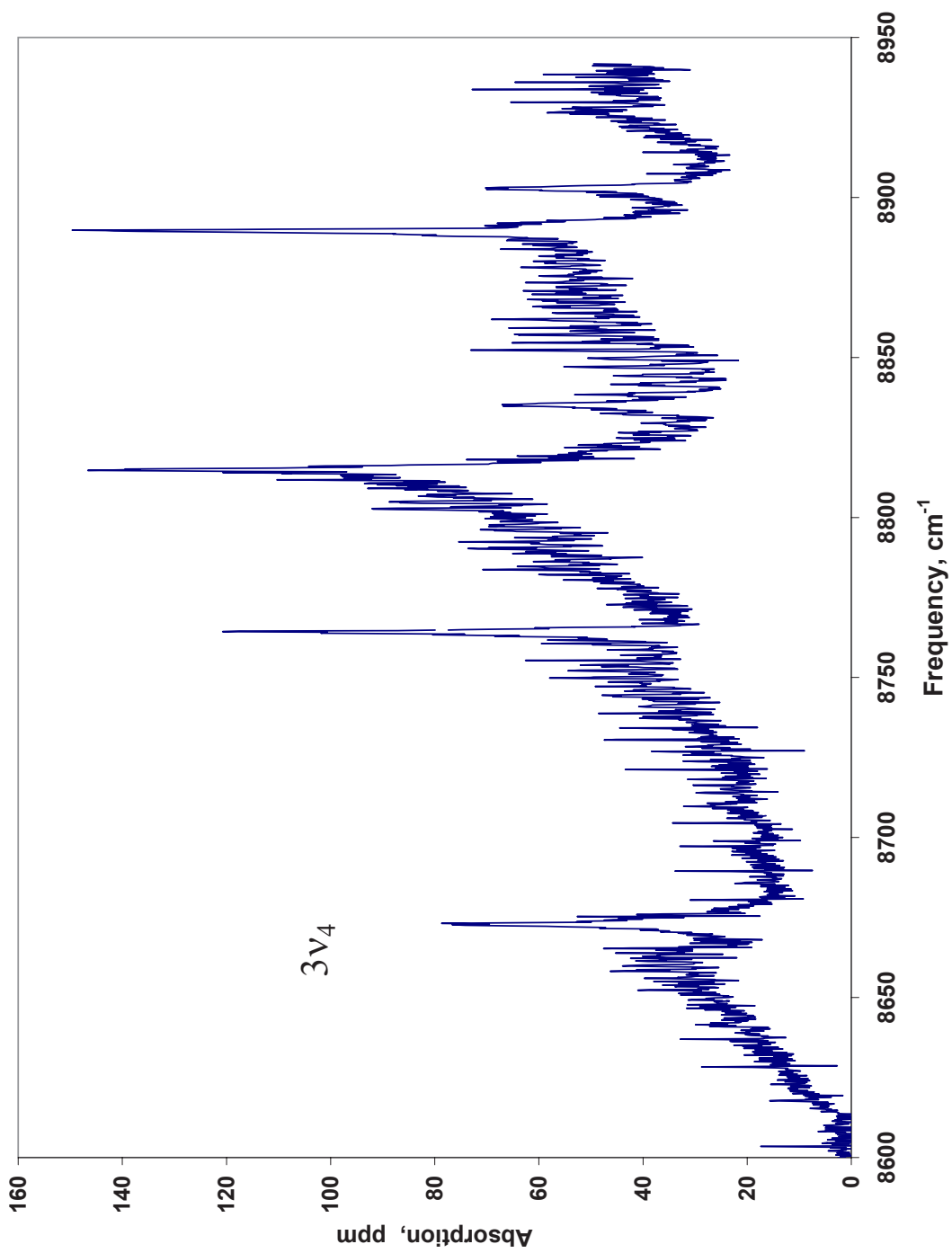


Figure 3.8: Cavity ringdown spectrum of the $\tilde{A} \leftarrow \tilde{X}$ transition of NO₃ in the 8600-8950 cm⁻¹ region.

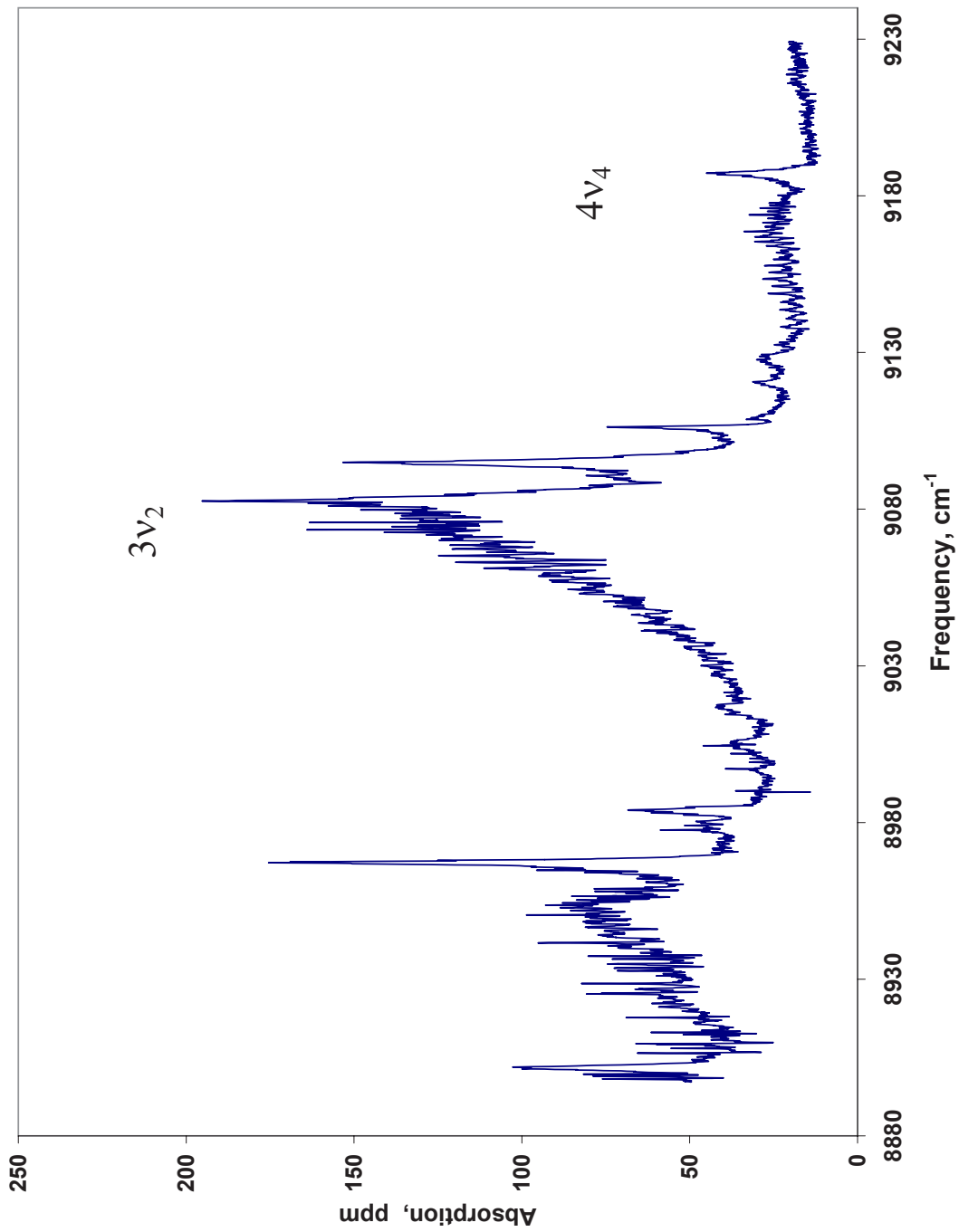


Figure 3.9: Cavity ringdown spectrum of the $\tilde{A} \leftarrow \tilde{X}$ transition of NO₃ in the 8900-9230 cm⁻¹ region.

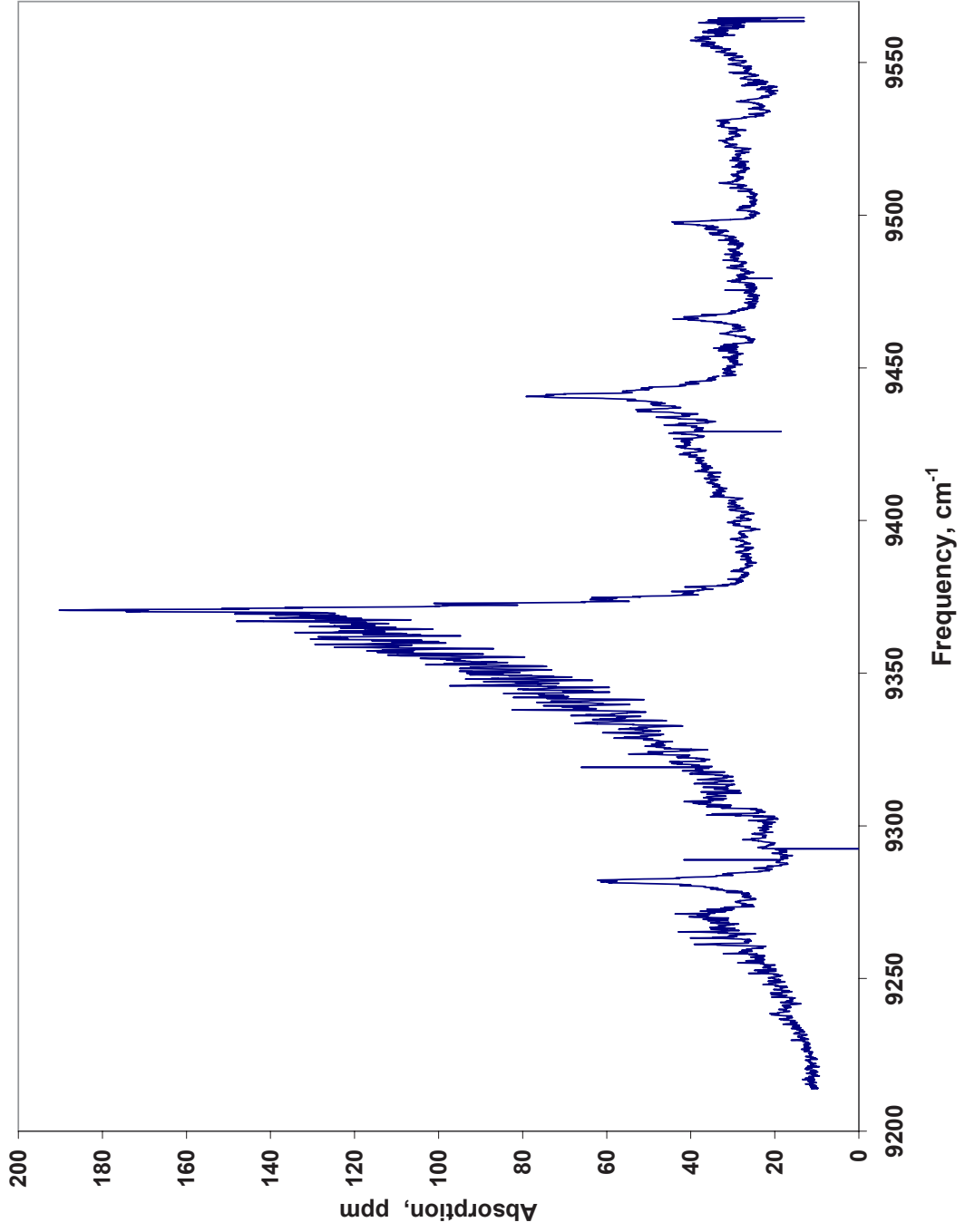


Figure 3.10: Cavity ringdown spectrum of the $\tilde{A} \leftarrow \tilde{X}$ transition of NO_3 in the $9210\text{-}9550\text{ cm}^{-1}$ region.

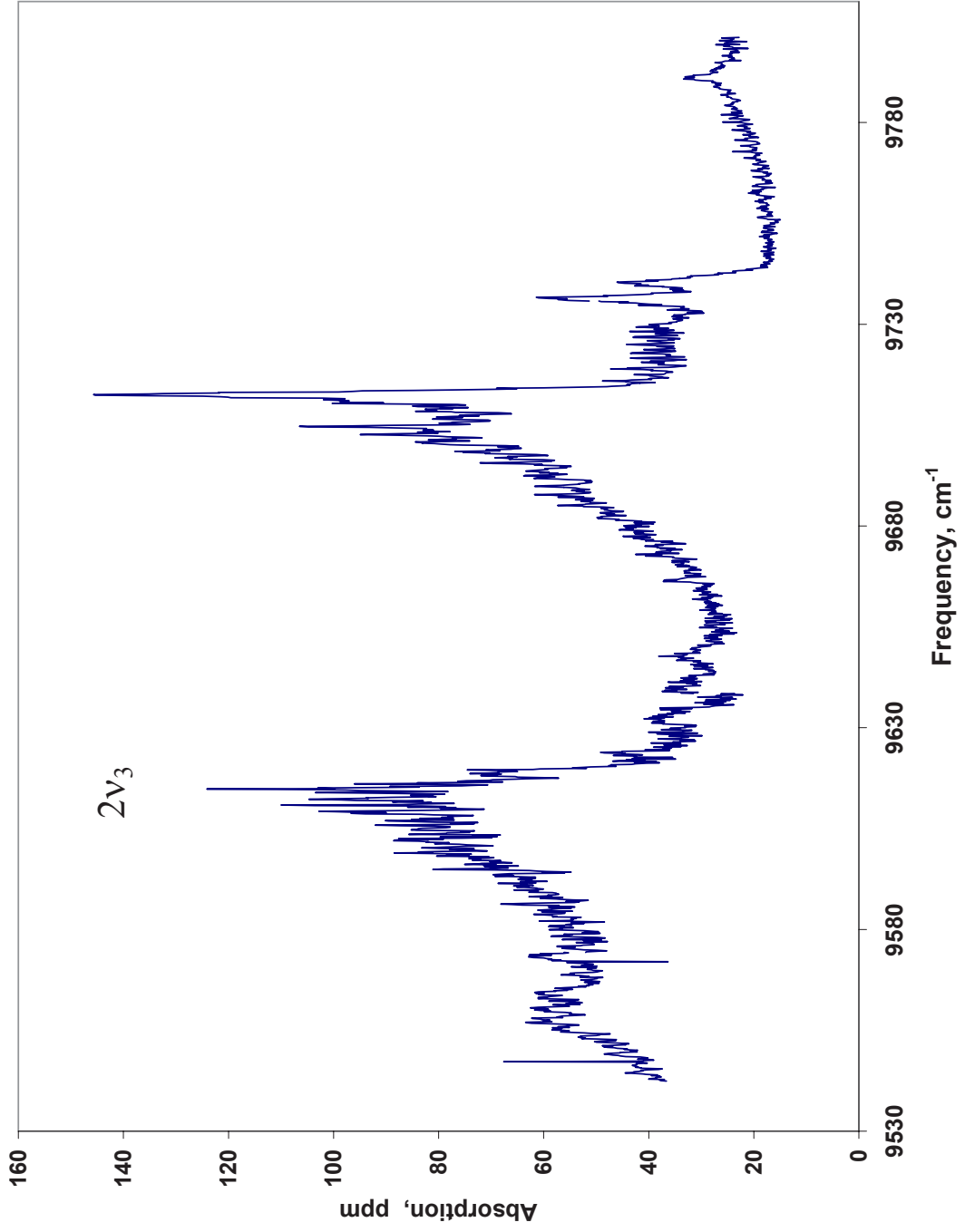


Figure 3.11: Cavity ringdown spectrum of the $\tilde{A} \leftarrow \tilde{X}$ transition of NO₃ in the 9550-9800 cm⁻¹ region.

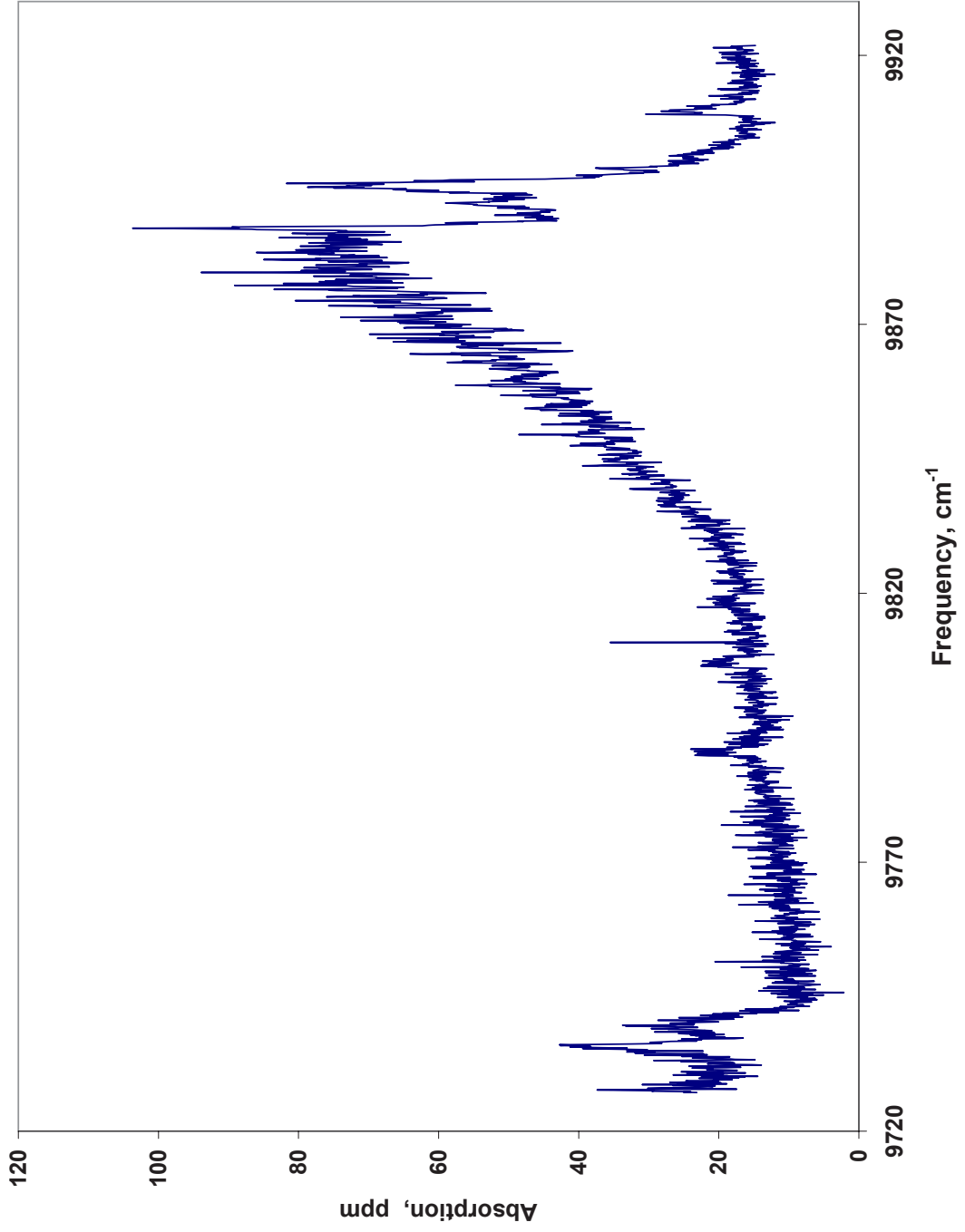


Figure 3.12: Cavity ringdown spectrum of the $\tilde{A} \leftarrow \tilde{X}$ transition of NO₃ in the 9720-9920 cm⁻¹ region.

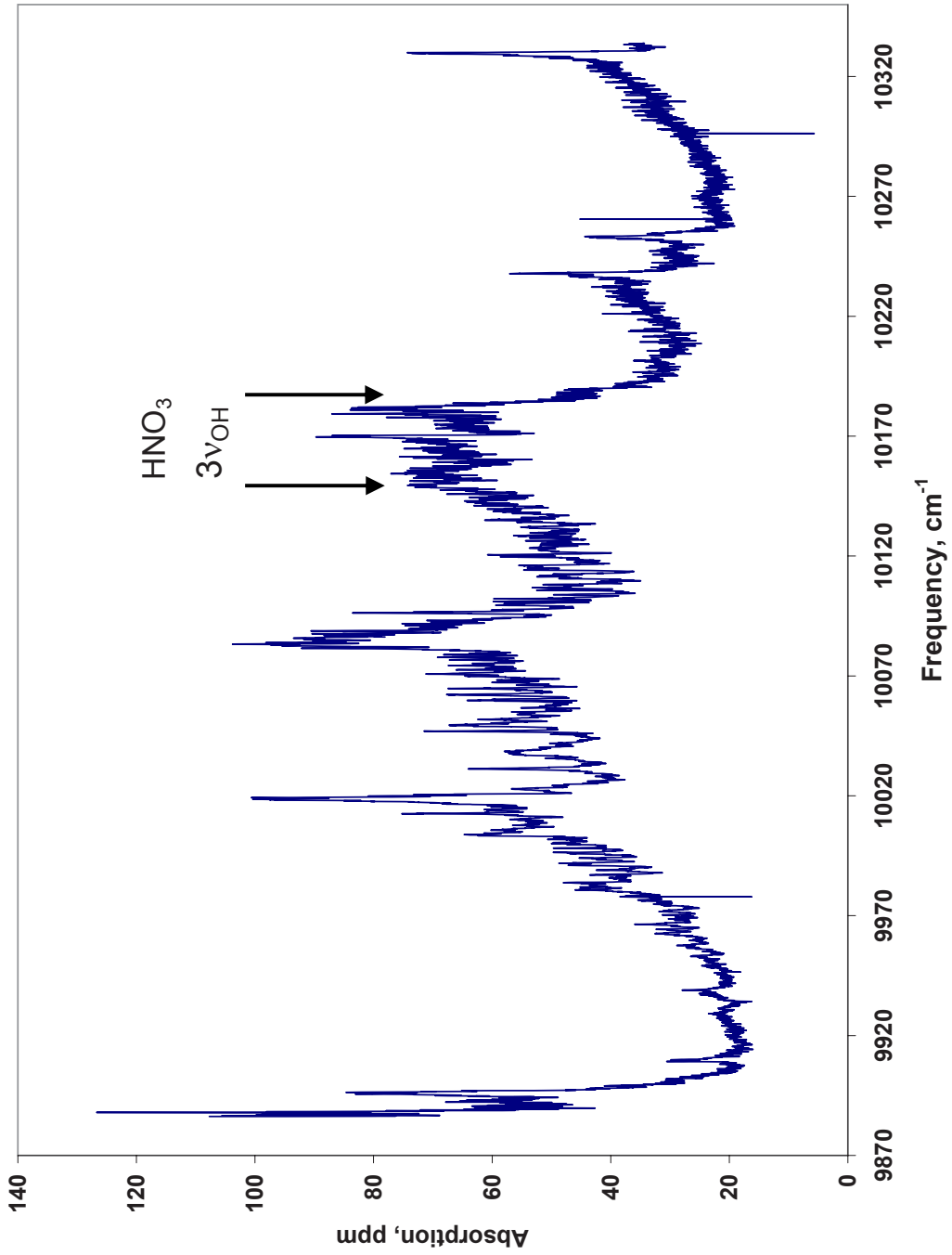


Figure 3.13: Cavity ringdown spectrum of the $\tilde{A} \leftarrow \tilde{X}$ transition of NO₃ in the 9870-10300 cm⁻¹ region.

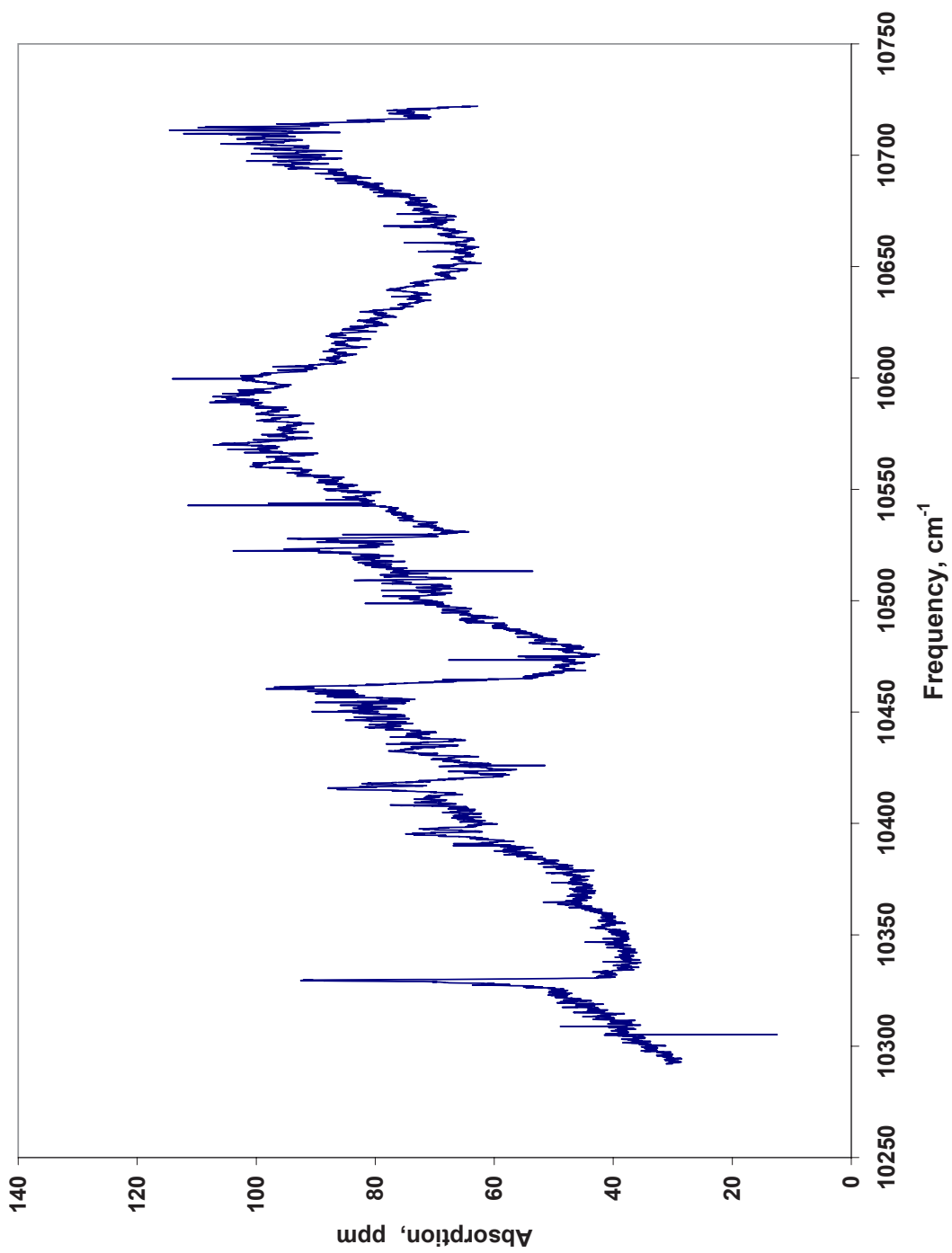


Figure 3.14: Cavity ringdown spectrum of the $\tilde{A} \leftarrow \tilde{X}$ transition of NO₃ in the 10300-10700 cm⁻¹ region.

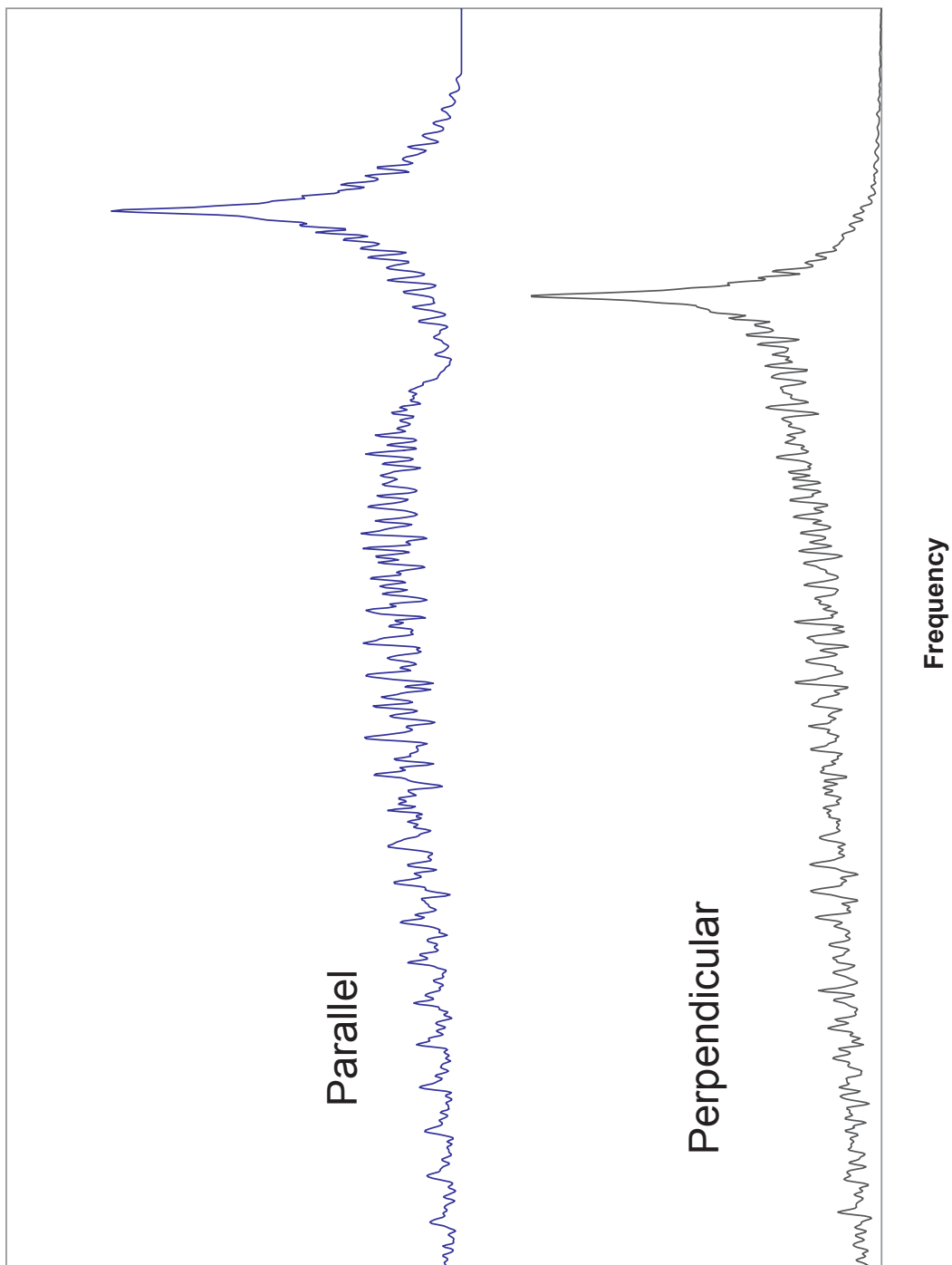


Figure 3.15: Simulation of rotational contours of a parallel and perpendicular $\tilde{A} \leftarrow \tilde{X}$ vibronic bands of NO_3 .

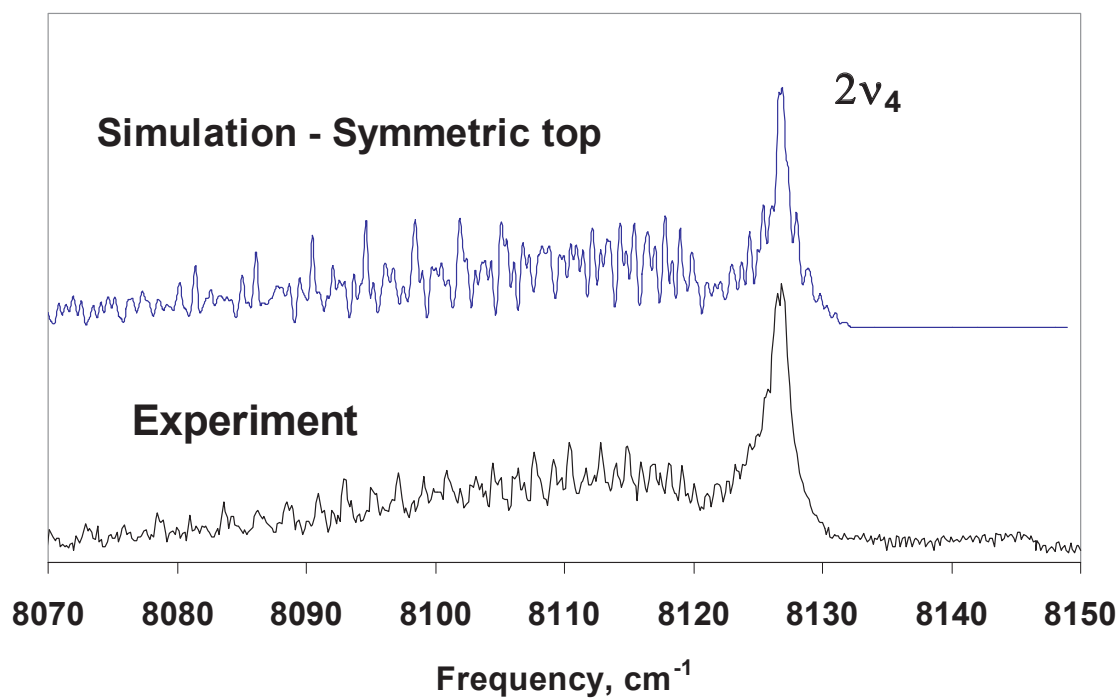
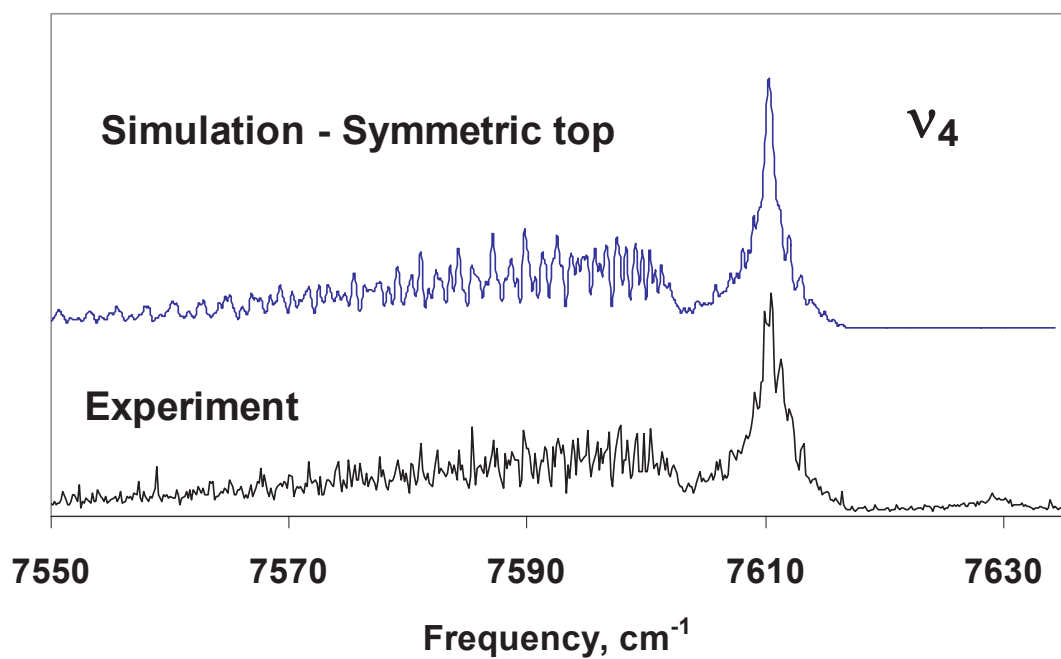


Figure 3.16: Simulation of rotational contours of the ν_4 and $2\nu_4$ bands.

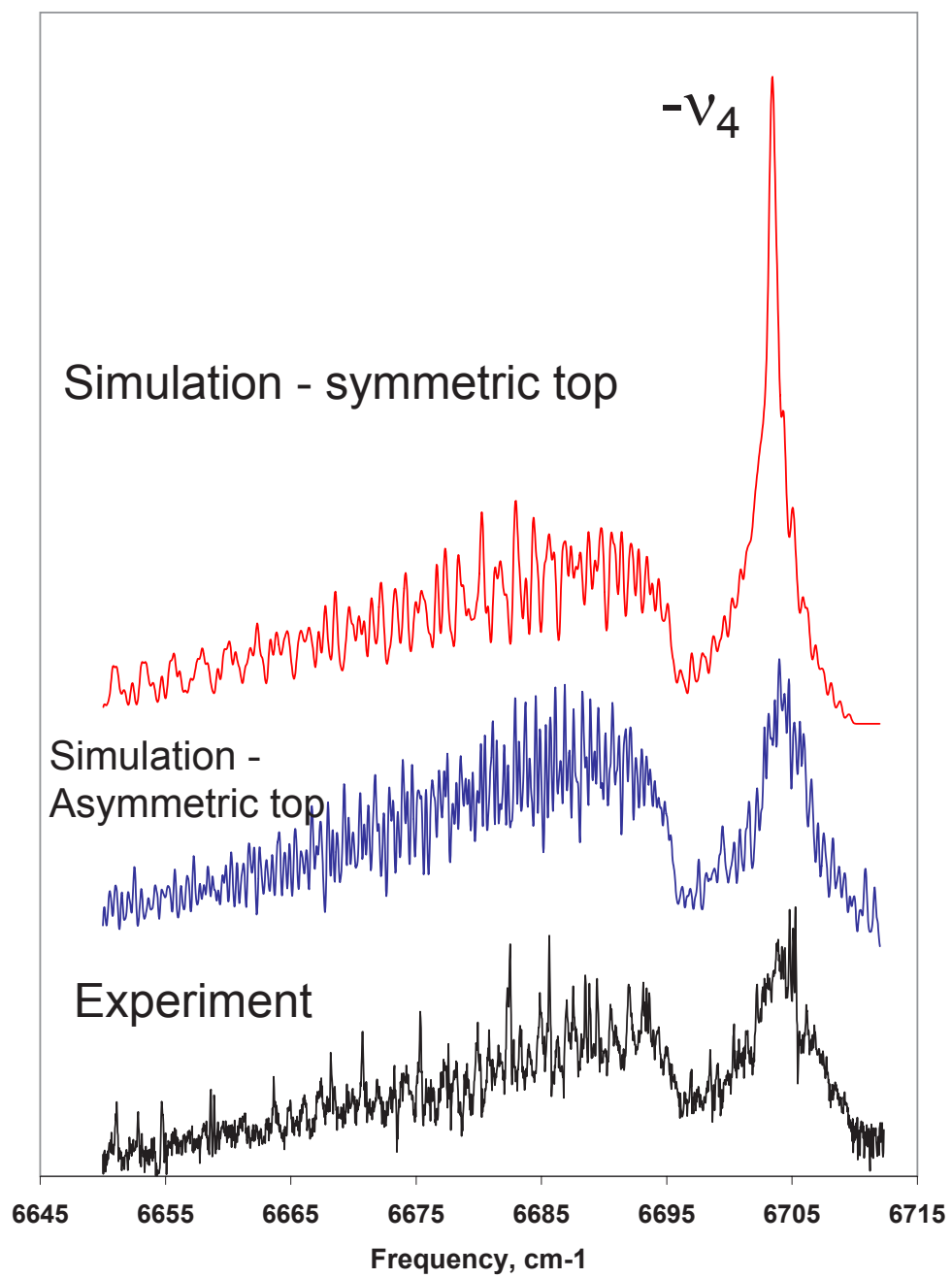


Figure 3.17: Simulation of rotational contour of the $-\nu_4$ band.

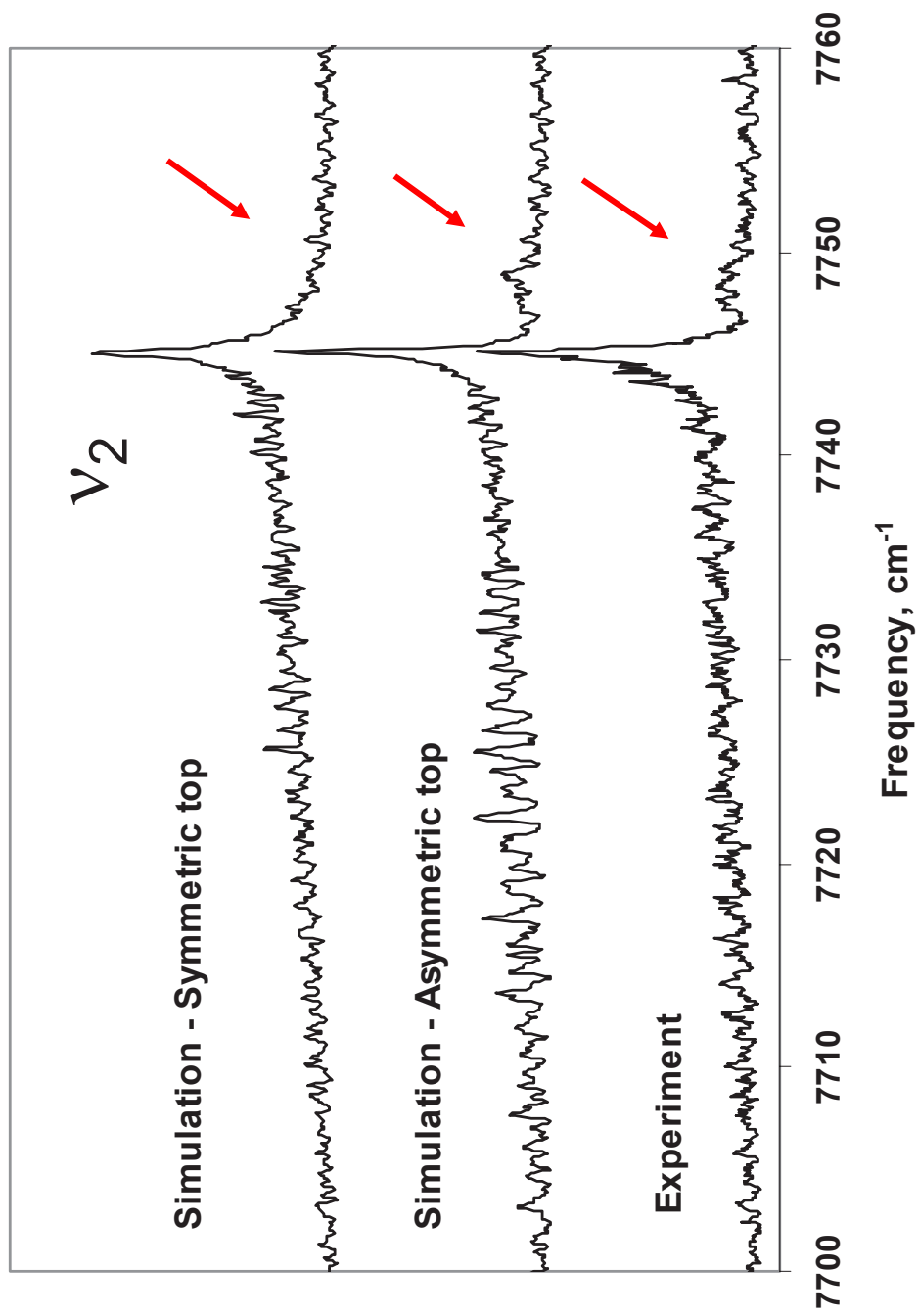


Figure 3.18: Simulation of rotational contour of the ν_2 bands. The arrow points at the feature that can only be reproduced by the asymmetric top Hamiltonian.

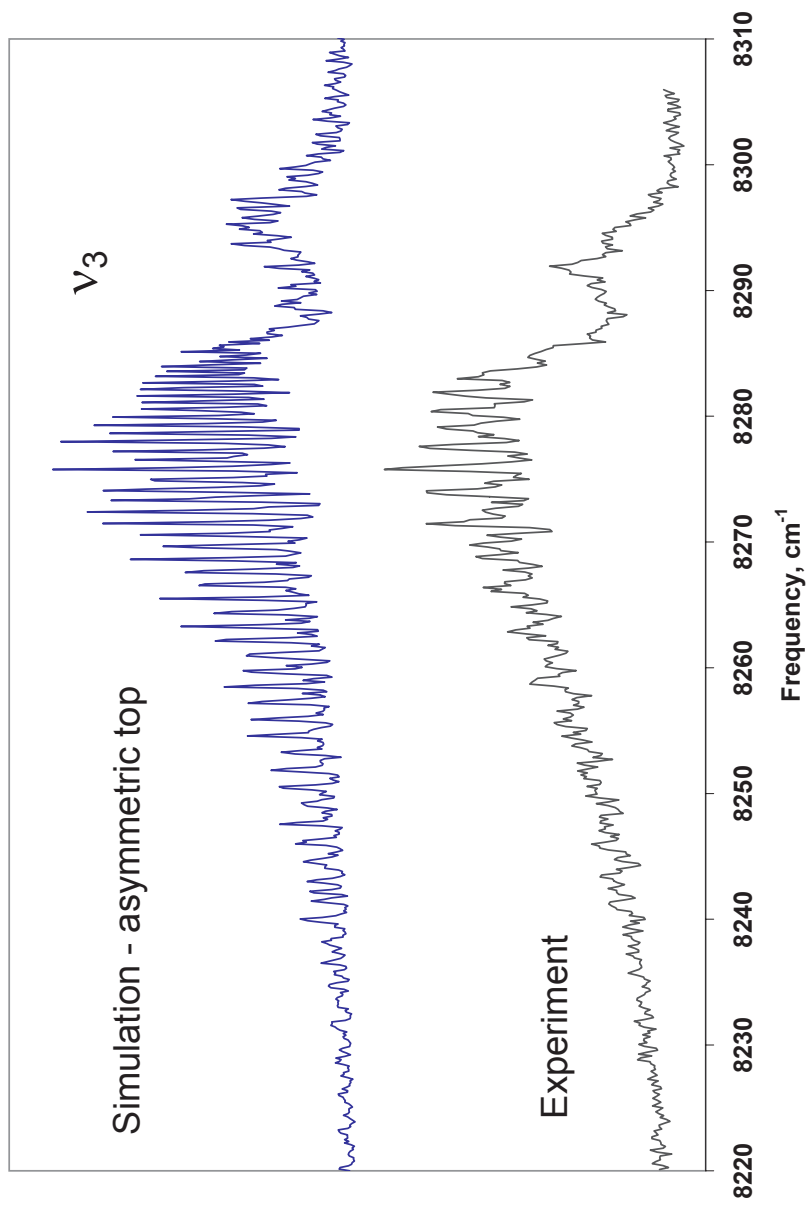


Figure 3.19: Simulation of rotational contour of the 8290 cm⁻¹ band.